UNIVERSITÀ
DEGLI STUDI
FIRENZE

DOTTORATO DI RICERCA IN
SCIENZE CHIMICHE

CICLO XXXI

COORDINATORE Prof. Piero Baglioni

Metallic nanoparticles for surface-enhanced Raman scattering (SERS) studies on proteins and pollutants

Settore Scientifico Disciplinare CHIM/02

Dottorando
Dott. Lorenzo Tognaccini

____
(firma)

Tutore
Prof. Giulietta Smulevich

____
(firma)

Coordinatore
Prof. Piero Baglioni

____
(firma)

Anni 2015/2018

Index

Abbreviations

2D	Two-dimensional
4-OP	4-octylphenol
5-c	Five-coordinated
6-c	Six-coordinated
AgNPs	Silver nanoparticles
AgNWs	Silver nanowires
AMPA	Aminomethylphosphonic acid
AuNPs	Gold nanoparticles
AuNRs	Gold nanorods
AuNRs@PAA	Polyacrylic acid-wrapped gold nanorods
AuHHCc	Cytochrome c bioconjugated on polyacrylic acid-wrapped gold nanorods
Cc	Cytochrome c
CCD	Charge coupled device
CL	Cardiolipin
CT	Porphyrin-to-iron charge transfer band
CTAB	Cetyl trimethylammonium bromide
DEHP	bis(2-ethylhexyl)phthalate
DIDP	Diisodecyl phthalate
DFT	Density functional theory
DLS	Dynamic light scattering
DMT	Dimethoate
EF	Enhancement factor
FAO	Food and agriculture organization
FCMs	Food contact materials
FEM	Finite element method
GLP	Glyphosate
Hb	Hemoglobin
HEPES	2-[4-(2-hydroxyethyl)piperazin-1-yl]ethanesulfonic acid
HHCc	Horse heart Cytochrome c

HS	High spin
HuCc	Human Cytochrome c
LIOAS	Laser-induced optoacoustic spectroscopy
LS	Low spin
LSPR	Localized surface plasmon resonance
MA	Met80Ala mutant of human Cytochrome c
Mb	Myoglobin
MCLG	Maximum contaminant level goal
NIR	Near-infrared
Nd:YAG	Neodymium-doped yttrium aluminium garnet; Nd:$Y_3Al_5O_{12}$
NMR	Nuclear magnetic resonance
NP	Nanoparticle
NR	Nanorod
OMT	Omethoate
PAA	Polyacrylic acid
PDI	Polydispersity index
PVP	Polyvinylpyrrolidone
RR	Resonance Raman
PDB	Protein data bank
SDS	Sodium dodecyl sulphate
SEM	Scanning electron microscopy
SERS	Surface enhanced Raman scattering
SERRS	Surface enhanced resonance Raman scattering
TEM	Transmission electron microscopy
UV-Vis	Ultraviolet-visible
WHO	World health organization
WT	Wild type
YHMA	Tyr67His/Met80Ala double mutant of human Cytochrome c

Summary

Surface enhanced Raman scattering (SERS) is a spectroscopic technique that can achieve extremely high sensitivity thanks to the enhancement of the Raman signal of molecules adsorbed on rough metal surfaces or on metallic nanoparticles. The high performances of this technique and the great variety of available nanosubstrates make SERS a very versatile tool to be employed in a large number of applications ranging from chemistry to life sciences, from physics to the environmental field.

In my PhD research activity I tested the properties of different metal nanoparticles in order to assess the possibility of their use for practical applications. My work was divided in three main topics.

1) Cytochrome c bioconjugation on gold nanorods

Gold nanorods (AuNRs) have interesting optical properties, being characterized by two surface plasmon bands, a transverse mode located in the visible region and a longitudinal one at longer wavelengths, which can be tuned by varying the length-to-width ratio. Bioconjugates of AuNRs can be of great interest for biomedical applications, like optical biosensing and imaging of tissues. However, their use is limited since NRs solutions are stabilized by the presence of concentrated cetyltrimethylammonium bromide (CTAB) surfactant which is cytotoxic and denatures proteins.

Therefore, I investigated the ability of weak negatively charged polyelectrolyte such as polyacrylic acid (PAA) to allow electrostatic interaction between AuNRs and a protein probe, horse heart Cytochrome c (HHCc), bearing surface positive charges (Lys residues).

Concomitantly to the work on the bioconjugation, I undertook detailed studies on misligated model compounds of HHCc to identified the possible Raman markers that allow to distinguish the native structure (His-Fe-Met heme coordination) from various non-native forms. In fact, it is well known that that the protein under denaturing conditions, can adopt His-Fe-His, His-Fe-Lys, His-Fe-OH^- and His-Fe-H_2O misligated

coordination states. Moreover, I also conducted a study of the human Cc (HuCc) wild type (WT) protein and its key variants Met80Ala (MA) and Tyr67H/Met80Ala (YHMA), to have a better understanding of the possible rearrangements of Cc distal cavity. The acquired knowledge on the misligated species, allowed me to identify the misligated coordination state upon mutation: the MA variant is a mixture of 6-coordinated high spin (6cHS) His-Fe-H_2O species and 6c low spin (6cLS) His-Fe-OH^- species, the latter decreasing at acidic pH; the YHMA double mutant shows, instead, a main His-Fe-His 6cLS coordination, with contributions from 6cHS and 5cHS species that increase by lowering the pH.

In parallel, I studied HHCc bioconjugation on the PAA-covered AuNRs. Adsorption of the protein and native state retention has been demonstrated for the first time on Au nanoparticles, by means of UV-Vis and Raman spectroscopy, thus validating the proposed protocol. The successful creation of such bioconjugates with the retention of the protein structure and function along with the preservation of the NPs properties (no aggregation) represents a fundamental accomplishment, as it provides the only way to access functional hybrid systems with potential applications in biotechnology, medicine, and catalysis.

2) Silver nanowires for SERS in the NIR region

SERS is commonly performed in the visible range, whereas infrared excitation is less usual in spite of its great potential in biological applications, since it can penetrate deeper in biological tissues, especially in the near-infrared (NIR) region. For this purpose, silver nanowires (AgNWs) are an interesting nanosubstrate because they have an extremely broad localized surface plasmon resonance (LSPR) extinction band, covering the UV, visible, and infrared regions.

Therefore, using benzenethiol, a typical SERS probe, and isopropanol an internal standard, I compared the SERS enhancement factor (EF) of commercially available and water dispersible AgNWs at three different excitation wavelengths. While the SERS enhancement factor (EF) is very low in the maximum extinction zone (406.7 nm), AgNWs displayed high EF in the visible region (514.5 nm) and fairly good EF in the NIR region (1064 nm). Moreover, laser-induced optoacoustic spectroscopy measurements (LIOAS) showed that contributions to extinction are mostly due to scattering, especially in the NIR. Hence, AgNWs demonstrated to be a very useful SERS substrate for NIR excitation, because not only in this region they are still fairly SERS-active, but also absorption does not significantly contribute to extinction, thus preventing the AgNWs from heating during irradiation. The effect is outstanding at 1064 nm, nevertheless, low heating and high SERS efficiency are also maintained at shorter wavelengths (514.5 nm), adding further versatility to AgNWs as SERS substrates.

3) In-field detection of pesticide and pollutants

In modern agriculture, chemical pesticides are widely used and play an essential role in food production, nevertheless there is increasing evidence showing an association between pesticide exposures and human diseases, such as cancer and nervous system disorders. Analytical methods with very high sensitivity and general applicability exist but are generally expensive and time-consuming. Hence I used citrate-capped (Lee-Meisel) spherical Ag nanoparticles (AgNPs) to develop a simple and quick method based on SERS for pesticides in-field detection. In particular I addressed dimethoate (DMT), an organophosphorous insecticide forbidden for organic cultures, and glyphosate (GLP), a massively used non-selective herbicide. Then I tried to apply the same method to the detection of food pollutants, the so-called FCMs (food contact materials) that also cause concern for human health due to their endocrine disruptor properties.

Lee-Meisel AgNPs proved to be a valid nanosubstrate for quick detection of DMT directly on the olive leaves. DMT presence can be detected by simply depositing a drop of AgNPs colloidal solution on a leaf and acquiring a few seconds spectrum with commercially available portable Raman instruments. This kind of test could be easily adopted for certification of organic oil production as a quick and low-cost screening technique before proceeding to more expensive and time-consuming quantitative analysis.

The same NPs also provided reproducible SERS spectra of GLP, which allowed for the first time a tentative assignment. Nevertheless, The AgNPs demonstrated insufficient sensitivity to detect GLP below 10^{-4} M concentration, higher than the recommended limit in drinking water. Hence, in order to develop an efficient detection method, SERS sensitivity needs to be further improved by using alternative nanosubstrates, possibly with sharp edges or tips allowing higher EF, or else functionalized for a better GLP adsorption.

For the FCM compounds I have obtained only very preliminary results. Among the tested compounds, diisodecyl phthalate (DIDP) and 4-octylphenol (4-OP) have insufficient affinity for citrate-capped AgNPs surface, whereas the SERS spectra of bisphenol A I obtained are quite different from those reported in literature, obtained on imprinted core-shell gold nanoparticles. Therefore specific surface engineereed AgNPs are required to obtain an appropriate adsorption and thus sensitivity for FCM compounds.

Chapter 1

Surface Enhanced Raman Scattering (SERS)

1.1 Introduction

Surface-enhanced Raman scattering (SERS) was observed for the first time in 1973 on a silver roughened electrode [Fleischmann 1974], but its interpretation dates to 1977 [Jeanmarie 1977]. Anyway, the great interest for this technique arose from the first observation of a single-molecule spectrum [Nie 1997, Kneipp 1997], that definitely demonstrated the high sensitivity that SERS can achieve. Thanks to the derived enthusiasm, in the last two decades quick and constant improvements in nanoscience and nanofabrication opened the doors to a broad range of SERS applications in many disciplines, from chemistry to life sciences, from physics to the environmental field, making of SERS a central research topic.

1.2 Electromagnetic enhancement

To obtain SERS, the analyte needs to be adsorbed on a rough metal surface or on the surface of metal nanoparticles (NPs, 10-100 nm), because the intensity of the signal strongly depends on the interaction between the light and the metal. Metals possess specific optical properties, that are the study subject of plasmonics, a term indicating the coupling between the electric field of the incident light (E_{inc}) and the wave oscillations of the metals conduction electrons (plasma oscillations, i.e. plasmons). In fact, when an electromagnetic wave (ω_{inc}) excites a metal nanostructure like a nanosphere in resonance with the plasmons, it induces an oscillation of the electrons cloud on the surface, thus producing a charge separation. This kind of resonance is called localized surface plasmon resonance (LSPR) and the associated dipole is proportional to the polarizability of the metal nanosphere and to the intensity of the E_{inc}. Moreover, the generated dipole acts as a nanoantenna and emits radiation at the same wavelength of the incident light (elastic light scattering), giving rise to an increase in the local electric field (E_{loc}) on the metal surface. The frequency at which the resonance takes place depends on the specific properties of the metal (the dielectric function) and on the medium.

When a molecule is adsorbed on a NP surface, the E_{loc} induces in it a dipole moment $\mu_{ind} = \alpha E_{loc}$ and, if the polarizability tensor α is different than zero, Raman inelastic scattering takes place with frequency ω_{Ram}. In addition, the Raman scattered radiation, that differs in frequency from the incident light by a vibrational transition energy, can be in resonance with the LSPR and induce E_{loc} increase, leading to elastic light scattering off the metal surface.

The resulting SERS enhancement factor (EF) depends on the product of the squares of the incident and the scattered light fields:

$I_{SERS} \propto | E_{inc}(\omega_{inc}) |^2 | E_{Ram}(\omega_{Ram}) |^2$

and it is maximum if both the radiation are close to resonance with the LSPR. If the frequency shift of the Raman scattered light is considered negligible, the SERS intensity becomes $I_{SERS} = (E_{inc})^4$, that is an approximation usually consistent for blue to green light excitation, but not for lower energy radiations. Standard SERS EFs may fall in the broad range of 10^3-10^{10} [Etchegoin 2011]. Anyway, even if the SERS signal is observed in the far field, it has to be specified that SERS enhancement is tightly confined to the surface, because, since the electric field intensity decrease with the cube of the distance, the EF decreases with the twelfth power of the distance. Another factor to be considered is the orientation of the analytes on the metal surface: different molecular disposition give rise to different SERS spectra: in fact SERS enhancement takes place only for those vibrational modes whose polarizability tensor α has a component perpendicular to the metal surface.

1.2.1 Hot spots and nanoparticles aggregation

The achievement of single-molecule spectra stimulated theoretical studies on the origin of very high EFs. Consequently, it has been observed that isolated NPs do not show high EFs (about 10^3), that are conversely localized in very confined regions (hot spots), i.e. in the gap space between two particles, but also (for non-spherical nanosubstrates) at sharp edges and on tips. The distance between the particle is crucial for the magnitude of the EF, such as an increase from 1 nm to 5.5 nm gap results in a decrease of the EF from 10^{10}-10^{11} to 10^{7}-10^{8} [Xu 2000]. Therefore, to reach high EFs even with spherical NPs, colloidal solution are often aggregated by adding inorganic salts like KCl, NaCl, NaBr, KNO_3, $NaNO_3$, $MgSO_4$, surfactants, organic amines or mineral acids to the colloids [Sun 2008, Kneipp 2006, Bell 2006]. Nevertheless, even the simple addition of the analyte to the colloidal solution can induce aggregation and increase the EF.

1.2.2 Metals

As mentioned above, the LSPR frequency depends on the specific properties of the metal, in particular on its dielectric function, and consequently, not every metal can achieve good EFs. Silver (Ag) and gold (Au) are the most useful metals for SERS purposes because their dielectric function provides LSPR peaks in the visible region, allowing excitation with lasers emitting in the visible range. Ag is plasmonically more active than Au and can achieve high sensitivity for excitation in all the visible spectrum. Conversely, Au performance is quite poor for $\lambda <$ 600 nm, but for $\lambda \geq$ 600 nm it can achieve very good EFs, similarly to Ag. Anyway, Au is more chemically stable and is usually preferred to Ag for application where the stability of the NPs dispersion in the long run is more crucial than high EF.

1.3 Chemical enhancement

The electromagnetic enhancement described above is the main effect giving rise to SERS, thanks to the high EFs that can be reached. Anyway, to completely describe this phenomena, chemical interactions between molecules and the metal surface have also to be considered, together with the unique electronic properties of the adsorbate molecules. The ensemble of this effects are named chemical enhancement and can contribute to the total enhancement for a 10-10^{3} factor. It consists in an increase of the adsorbed molecules polarizability α, inducing increase of the adsorbate dipole. For example, charge transfer (CT) between the molecule and the metal can modify α, changing the Raman cross-section, or new electronic excitation routes could result through a photoinduced CT from the metal to the adsorbed molecule. Moreover, the adsorbate molecules usually differ from the free ones in the energy levels distribution; if the incident light is in resonance with an electronic transition of the adsorbate and not with the free molecules, resonance Raman (RR) would be obtained for the adsorbate.

In most cases, more than one of this effects occur contemporarily, making identification of the exact mechanism and separation of the different possible contributions a hard task, mostly treated by electronic structure calculations [Zhao 2006, Jensen 2008]

1.4 Nanoparticle SERS substrate

The ideal nanoparticle substrate is easy to prepare, well-reproducible, stable and capable to perform high EFs. During the years many synthetic methods have been proposed and various shape and dimension of NPs have been achieved. In fact, the key step for successful SERS application is the fabrication of a nanosubstrate that guarantees performance and reproducibility.

The most used SERS substrates are metallic NPs synthesized by wet chemistry, because they have great advantages such as low cost, easy preparation and characterization. Moreover, the use of a colloidal solution allows to minimize sample degradation even when high laser power is needed.

The most common synthesis method is by chemical reduction of metal salts in solution by using various reducing agents like sodium citrate [Lee 1982, Frens 1973], sodium borohydride [Weaver 1998], hydrazine [Nickel 2004] or hydroxylamine hydrochloride [Canamares 2005, Leopold 2003]. The size distribution of the NPs can be controlled by simply tuning temperature, pH and the concentration and kind of metal salt, reductant and surfactant.

Moreover, many differently shaped NPs have been fabricated and experimental data also indicate that anisotropic shapes allow to obtain higher EFs than spherical NPs. For example, Au nanorods (AuNRs) are produced by the seed-mediated growth method [Guo 2009, Gole 2004], in which variation of the synthesis condition results in AuNRs with different aspect ratios (length-to-width ratio); this allows a fine tuning of their SERS activity, because the NRs longitudinal surface plasmon resonance mode red shifts with increasing aspect ratio [Orendorff 2005, Orendorff 2006].

Another example is the polyol synthesis of Ag nanoparticles (AgNPs) with various shapes [Wiley 2006, Sun 2003, Tao 2008]. Ethylene glycol is used both as a solvent and a reducing agent; by varying the concentration of glycoaldehyde and the temperature, differently shaped AgNPs can be obtained, also allowing to synthesize NPs with sharp edges or tips [McLellan 2006]. With this method it is even possible to synthesize long Ag nanowires (AgNWs) with a broad LSPR band covering also the near infrared (NIR) region, thus suitable for long-wavelength excitation applications.

In my thesis I tested different metal nanoparticles properties in order to assess the possibility of their use for practical applications.

i) I addressed biocompatibility of AuNRs, to be used in biomedical applications, by means of conjugation with proteins. So far, not many biological applications with gold nanorods have been reported, in part because nanorod solutions are stabilized by the presence of concentrated CTAB surfactant which are cytotoxic. I have, therefore, explored the use of a different approach for the bioconjugation and my experiments were aimed to spectroscopically verify both the effectiveness and the biocompatibility of the bioconjugation process.

ii) I evaluated the suitability of commercially available AgNWs as a SERS nanosubstrate for applications with excitation in the near-infrared (NIR) region. In fact, significant biomedical applications become possible when nanoparticle resonances are tuned to NIR, where most biological tissues are relatively transparent.

iii) I exploited citrate-capped spherical AgNPs to set up a quick and sensitive method based on SERS to detect pesticides or different pollutants both in solution or directly in-field. In fact, the environmental concern on the use of pesticide (as well of any pollutant) comes from their effects on non-target species, and to their possibility to directly contaminate food. Hence it is essential to be able to monitor pollutants in the environment and food with rapid on-site measurement.

References

- Bell S.E., Sirimuthu N.M., J. Am. Chem. Soc. 2006, 128, 15580-15581.
- Canamares M.V., Garcia-Ramos J.V., Gómez-Varga J.D., Domingo C., Sanchez-Cortes S., Langmuir 2005, 21, 8546-8553.
- Etchegoin P.G., Le Ru E.C., Surface Enhanced Raman Spectroscopy (Schlücker S. Ed.), Wiley-VCH, Weinheim, 2011, pp. 1 – 37.
- Fleischmann M., Hendra P.J., McQuillan A.J., Chem. Phys. Lett. 1974, 26, 163.
- Frens G., Nat. Phys. Sci. 1973, 241, 20-22.
- Gole A., Murphy C.J., Chem. Mater. 2004, 16, 3633-3640.
- Guo S.-J., Dong S.-J., Wang, E.-K., Cryst. Growth Des. 2009, 9, 372-377.
- Jeanmaire D.L., Van Duyne R.P., J. Electroanal. Chem. 1977, 1, 84.
- Jensen L., Aikens C.M., Schatz G.C., Chem. Soc. Rev. 2008, 37, 1061.
- Kneipp K., Wang Y., Kneipp H., Phys. Rev. Lett. 1997, 78, 1667-1670.
- Kneipp K., Kneipp H., Isr. J. Chem. 2006, 46, 299-305.
- Lee P.C., Meisel D., J. Phys. Chem. 1982, 86, 3391-3395.
- Leopold N., Lendl B., J. Phys. Chem. B 2003, 107, 5723-5727.
- McLellan J., Siekkinen A., Chen J., Xia Y., Chem. Phys. Lett. 2006, 427, 122-126.
- Nickel U., Mansyreff K., Schneider S., J. Raman Spectrosc. 2004, 35, 101-110.
- Nie S., Emory S.R., Science 1997, 275, 1102-1106.
- Orendorff C.J., Gole A., Sau T.K., Murphy C.J., Anal. Chem. 2005, 77, 3261-3266.
- Orendorff C.J., Gearheart L.A., Jana N.R., Murphy C.J., Phys. Chem. Chem. Phys. 2006, 8, 165-170.
- Sun Y., Xia Y., Analyst 2003, 128, 686-691.

- Sun L.-L., Song Y.-H., Wang L., Guo C.-L., Sun Y.-J., Liu Z.-L. Li Z. J. Phys. Chem.C 2008, 112, 1415‑1422.
- Tao A.R., Habas S., Yang, P., Small 2008, 4, 310‑325.
- Weaver G.C., Norrod K., J. Chem. Educ. 1998, 75, 621‑624.
- Wiley B.J., Im S.H., Li Z.Y., McLellan J., Siekkinen A., Xia Y., J. Phys. Chem. B 2006, 110, 15666‑15675.
- Xu H., Aizpurua J., Käll M., Apell P., Phys. Rev. E 2000, 62, 4318.
- Zhao L., Jensen L., Schatz G.C., J. Am. Chem. Soc. 2006, 128, 2911.

Chapter 2

Methods

2.1 UV-Visible electronic absorption spectroscopy

Electronic absorption measurements were recorded using a 1 cm or a 1 mm quartz cuvette at 600 nm/min scan rate, or with a 5 mm nuclear magnetic resonance (NMR) tube at 300 nm/min scan rate at 25 °C by means of a Cary 60 spectrophotometer (Agilent Technologies, Santa Clara, CA) with a resolution of 1.5 nm. All spectra were baseline-subtracted and corrected for the dilution factor. For the differentiation process, the Savitzky–Golay method was applied using 15 data points (LabCalc, Galactic Industries, Salem, NH). No changes in the wavelength or in the bandwidth were observed when the number of points was increased or decreased. Absorption spectra were measured both prior to and after RR measurements to ensure that no degradation occurred under the used experimental conditions.

2.2 Raman, resonance Raman and SERS spectroscopy

The Raman, resonance Raman (RR) and SERS spectra were obtained with different kinds of instruments.

- A dispersive Raman spectrometer equipped with a Kr^+ laser (Innova 300 C, Coherent Inc., Santa Clara, CA, USA) for 406.7 and 413.1 nm, a He-Cd laser (Kimmon IK4121R-G, Kimmon Koha Co. LTD, Tokyo, Japan) for 441.6 nm and an Ar^+ laser (Innova 90-5, Coherent Inc., Santa Clara, CA, USA) for 514.5 nm excitation wavelength. The incident light was focused with a 25 cm focal length spherical lens onto the samples. The samples were analysed at 25 °C in a 1 cm quartz cuvette for SERS measurements or in a 5 mm slowly-rotating NMR tube for RR spectra. The back-scattered light was dispersed with a triple monochromator, consisting of two Acton Research SpectraPro 2300i working in the subtractive mode, and a SpectraPro 2500i (Princeton Instruments, Trenton, NJ, USA) in the final stage with 3600 or 1800 grooves/mm grating, and detected with a liquid-nitrogen cooled CCD detector. The spectral resolution was < 4 cm^{-1} and the spectral dispersion > 1.2 cm^{-1} per pixel. The samples of the mutated proteins were cooled by a gentle flow of N_2 gas (sample temperature about 12 °C) during the RR measurement. This setup has been used for experiments in Chapters 3 and 4.

- A portable Raman spectrometer for SERS "in-field measurements" was assembled using a 785 nm narrow-band diode laser coupled to a Raman fiber probe (InPhotonics, Norwood, MA, USA) delivering 20 mW laser power at sample; the Raman scattered light was feed to a BWTek Exemplar Pro spectrometer (B&W Tek, Newark, DE, USA) with deep-cooled CCD detector. The spectra were recorded at 25 °C in a 1 cm quartz cuvette. Used for experiments in Chapter 5.
- A Renishaw RM2000 micro-Raman (Renishaw, Wotton-under-Edge, UK), used to obtain the spectra of dried solutions on olive leaves. The measurements were carried out at 25 °C using a 785 nm laser excitation source focused by a 20x microscope objective (2mW at the sample). Raman mapping was performed by moving the sample on a motorized micrometric table, acquiring the spectrum in different points and plotting the intensity of a representative band as a function of the sampling point position. Used for experiments in Chapter 5.
- A BWTek spectrometer with the BAC151B microsampling system (B&W Tek, Newark, DE, USA) and a 785 nm laser source, focusing 5 mW on the sample was used for final tests in order to assess feasibility of in-field measurements. Spectra were measured at 25 °C directly on olive leaves. Used for experiments in Chapter 5.
- A MultiRAM FT-Raman system (Bruker, Billerica, MA, USA), equipped with a Nd:YAG laser emitting at 1064 nm. The spectral resolution was 4 cm^{-1}. Room temperature spectra of liquid samples were obtained using a 1 cm quartz cuvette, whereas spectra of solid samples were recorded at 25 °C by putting some powder in an aluminium holder. Used for experiments in Chapters 4 and 5.

2.3 Spectroscopic data analysis

Spectroscopic data were analysed using LabCalc (Galactic Industries Corporation, Salem, NH, USA) and OriginPro (OriginLab Corporation, Northampton, MA, USA). The spectra obtained with the 1064 nm excitation wavelength were calibrated automatically on the basis of the frequency of a He-Ne laser. All the other spectra were calibrated with indene, n-pentane and carbon tetrachloride as standards to an accuracy of 1 cm^{-1} for intense isolated bands.

All measurements were repeated several times under the same conditions to ensure reproducibility. To improve the signal-to noise ratio, a number of spectra were accumulated and summed only if no spectral differences were noted. All spectra were baseline-corrected and vertically shifted to allow better visualization in the presented figures.

A spectral simulation program (LabCalc) using a Lorentzian line shape was used to determine the peak positions, bandwidth, and intensity. The frequencies of the bands were optimized to an accuracy of 1 cm^{-1} and the bandwidths to an accuracy of 0.5 cm^{-1}. Bandwidths (full width at half-maximum) varied as follows: 12-15 cm^{-1} in the high-frequency region and 9-14 cm^{-1} in the low-frequency region.

2.4 Transmission electron microscopy (TEM)

TEM analyses were performed with a JEM-1011 microscope (JEOL Ltd., Akishima, Tokyo, Japan) operating at 100 kV. The samples were prepared by deposition of a few drops of aqueous NPs dispersions onto a carbon-coated copper grid and evaporation of the solvent. Each sample was stained with a 2% (v/v) phosphotungstic acid solution for 30 s. A statistical analysis of NRs size distribution was performed on the basis of low-magnification TEM images with the help of ImageJ software (NIH, Bethesda, MD, USA). At least 150 NPs were counted for each sample.

2.5 Particle size, size distribution and ζ-potential measurements

The average hydrodynamic diameters (z-average), size distribution (polydispersity index, PDI), and ζ-potential were determined using Zetasizer Nano ZS (Malvern Instruments Ltd., Malvern, UK) by dynamic light scattering (DLS) after suspension in demineralized water at a suitable concentration (≈0.1%, w/v NRs concentration). The ζ-potential was determined by laser Doppler velocimetry after dilution of the samples with KCl 1 mM (≈0.01%, w/v NRs concentration).

2.6 Scanning electron microscopy (SEM)

SEM analysis was performed with a EVO MA15 scanning electron microscope (Carl Zeiss, Oberkochen, Germany) coupled with an Oxford INCA250 energy-dispersive spectrometer (Oxford Instruments, Abingdon-on-Thames UK), operating at 25 kV accelerating voltage and 7.5 mm working distance. Water-dispersed AgNWs were dried in a convection oven at 80 °C for some hours. Immediately prior to SEM measurement, a gold thin film of about 10 nm was sputtered over the sample.

2.7 Laser-induced optoacoustic spectroscopy (LIOAS)

LIOAS signals are generated by thermal relaxation that follows light absorption, producing a temperature increase in the surrounding environment of the absorbing molecules [Tam 1986] or particles [Pang 2016, Shi 2017]. The subsequent expansion induces emission of a mechanical (acoustic) wave that is detected by means of a piezoelectric transducer. Light scattering does not contribute to the generated acoustic wave, at least in diluted solutions [Small 2000].

In the case of a dispersion of scattering nanoparticles, extinction (E_λ) is the sum of the absorption (A_λ) and scattering (S_λ) contributions [Jain 2006, Van Dijk 2006]:

$E_\lambda = A_\lambda + S_\lambda$

where λ is the excitation wavelength. Absorption can be isolated by calibrated LIOAS measurements, in which the signal of the sample and that of a calorimetric reference are recorded under strictly identical experimental conditions. A calorimetric reference is a substance which (i) attenuates the incident light without scattering losses, (ii) instantaneously releases all the absorbed energy as heat and (iii) does not give rise to intrinsic volume changes upon photoexcitation [Braslavsky 1972]. It can be reasonably assumed that conditions (ii) and

(iii) are also true for my silver nanowires (AgNWs) samples, therefore, signal decreases must be due to scattering losses. The signals were detected with a 1 MHz resonant frequency piezoelectric transducer (V103-RM, Panametrics, Cumming, GA, USA) clamped to a spectrophotometry quartz cuvette with a 1 cm optical path. We averaged its output, once processed using a Panametrics 5660 B amplifier, with a TDS-3054B digitizing oscilloscope (Tektronix, Beaverton, OR, USA). The minimum number of signals was 512 for each averaging cycle. The laser source was the output of a Nd:YAG laser at 1064, 532 and 355 nm (Quanta System, Samarate, Italy). The pulse duration was ~10 ns and the repetition rate 10 Hz. The incident laser energy (< 100 μJ) was measured behind the empty sample cuvette using a pyroelectric head energy meter, before and after each LIOAS measurement. The incident laser beam was shaped by a rectangular slit with 1 × 10 mm size without focusing on the sample. Noticeably, the irradiance (< 1 mW μm^{-2}) was below the threshold for the formation of bubbles according to the recent calculations [Shi 2017]. The laser energy at the sample was adjusted by means of neutral density filters. The LIOAS signal amplitude was considered as the peak-to-valley value of the waveform observed on the oscilloscope. The calorimetric references for the calibration were $KMnO_4$ or $CuSO_4$ solutions. Extinction spectra were recorded before and after each measurement to check the integrity of the sample and reference solutions. In particular, extinction changes, which could imply AgNWs reshaping modifications, were not detected.

References

- Braslavsky S.E., Heibel G.E., Chem. Rev. 1992, 92, 1381.
- Jain P.K., Lee K.S., El-Sayed I.H., El-Sayed M.A., J. Phys. Chem. B 2006, 110, 7238.
- Pang G.A., Laufer J., Niessner R., Haisch C., J. Phys. Chem. C 2016, 120, 27646.
- Shi Y., Yang S., Xing D., J. Phys. Chem. C 2017, 121, 5805.
- Small J.R., Foster N.S., Amonette J.E., Autrey T., Appl. Spectrosc. 2000, 54, 1142.
- Tam A.C., Rev. Mod. Phys. 1986, 58, 381.
- Van Dijk M.A., Tchebotareva A.L., Orrit M., Lippitz M., Berciaud S., Lasne D., Cognet L., Lounis B., Phys. Chem. Chem. Phys. 2006, 8, 3486.

Chapter 3

Surface engineering of gold nanorods for Cytochrome c bioconjugation: an effective strategy to preserve protein structure

- Ciaccio C.*, Tognaccini L.*, Battista T., Cervelli M., Howes B.D., Santucci R., Coletta M., Mariottini P., Smulevich G., Fiorucci L., The Met80Ala and Tyr67His/Met80Ala mutants of human Cytochrome c shed light on the reciprocal role of Met80 and Tyr67 in regulating ligand access into the heme pocket, J. Inorg. Biochem. 169, 2017, 86-96.

* these authors contributed equally to this work

- Milazzo L., Tognaccini L., Howes B.D., Sinibaldi F., Piro M.C., Fittipaldi M., Baratto M.C., Pogni R., Santucci R., Smulevich G., Unravelling the Non-Native Low-Spin State of the Cytochrome c–Cardiolipin Complex: Evidence of the Formation of a His-Ligated Species Only, Biochemistry 2017, 56, 1887-1898.

- Milazzo L., Tognaccini L., Howes B.D., Smulevich G., Probing the non-native states of Cytochrome c with resonance Raman spectroscopy: a tool for investigating the structure-function relationship, J. Raman Spectrosc. 2018, 49, 1041-1055.

- Placido T.*, Tognaccini L.*, Howes B.D., Montrone A., Laquintana V., Comparelli R., Curri M.L., Smulevich G., Agostiano A., Surface engineering of gold nanorods for Cytochrome c bioconjugation: an effective strategy to preserve the protein structure, ACS Omega 2018, 3, 4959-4967.

* these authors contributed equally to this work

3.1 Introduction

Anisotropic gold nanoparticles (AuNPs) such as nanorods (NRs) have recently attracted a lot of attention due to their interesting optical properties which have been exploited especially in biomedical diagnostics, in photothermal therapy, as dark field imaging contrast agents and surface enhanced Raman scattering (SERS) substrates [Alkilany 2012, Jain 2008, Kuo 2010, Ros 2014, Daniel 2004, Burda 2005, Lee 2006, Njoki 2007]. AuNRs are characterized by two surface plasmon bands, a transverse mode located in the visible region around 520 nm and a longitudinal one at longer wavelengths, which can be tuned from the visible to the near-infrared (NIR) region by varying the length-to-width ratio of the AuNRs [Pérez-Juste 2005, Sau 2010, Link 1999]. Bioconjugates of AuNRs can be of great interest for biomedical applications, especially when the resonances of the NRs are tuned to the NIR, where biological tissues are relatively transparent. In particular, NP-protein hybrid systems have already demonstrated their potential for many applications in research and diagnostics, namely optical biosensing [Katz 2004], imaging of tissues, cells, or macromolecules [Daniel 2004, Hainfeld 2000, Mason 2005] and physicochemical manipulation of biological systems [Hamad-Schifferli 2002]. To accomplish this bioconjugation task, the nature of the NP interface and the adsorption are crucial, as they can determine conformational changes, denaturation, or undesirable protein orientations with respect to the substrate [Yang 1993]. To solve these problems, NPs have been modified with small molecules [Hobara 1994] or polymeric matrixes [Lofas 1995, Yu 2013, Malikova 2002]. The goal of my work has been to bioconjugate water-dispersible AuNRs, prepared by professor Agostiano's research group (Bari University) and coated with the positively charged surfactant stabilizer cetyltrimethylammonium bromide (CTAB), to horse heart cytochrome c (HHCc), while preserving the protein structure. Up to now, three different approaches to link proteins to Au are reported in the literature [Austin 2014]:

- direct anchoring on the CTAB coating of AuNRs by exploiting electrostatic adsorption, provided that the protein is negatively charged;

- interposing a negatively charged layer as a "glue" between CTAB and the protein [Huang 2009];
- using as intermediate linkers bifunctional molecules containing a functional group with good affinity for the metal surface (i.e., cyano, mercapto, carboxylic acid or amino groups) to displace the native bilayer and, on the other side, a functional group that interacts with the protein by means of covalent or noncovalent bonds [Austin 2014].

HHCc, that is almost identical to the human variant, has been selected as a protein probe to test the NPs biocompatibility being a small, single chain heme protein that has been extensively studied by resonance Raman (RR) spectroscopy [Scott 1996]. It is also an interesting pharmacological target because not only it plays an important role in electron transfer, but also acts as an apoptosis (programmed cell death) initiator after interacting with cardiolipin, a phospholipid of the inner mitochondrial membrane [Orrenius 2007, Caroppi 2009, Kagan 2009].

Since HHCc do not have any functional groups able to covalently bind the Au surface, a direct covalent interaction of HHCc with the bare AuNR cannot be envisaged. On the other hand, HHCc exhibits three positively charged residues (Lys72, 73, 79) on its surface [Daniel 2004, Weidinger 2006] that prevent any direct electrostatic interaction with the CTAB-capped AuNRs. Moreover, a surface functionalization step to replace the pristine CTAB coating with bifunctional molecules more suited for subsequent binding of HHCc could cause irreversible aggregation of AuNRs or a continuous release of the residual CTAB, thus altering the protein stability [Murphy 2010]. Hence, a reliable strategy, typically used to modify the surface chemistry and simultaneously protect the native NR coating from possible detachment of CTAB molecules, is based on polyelectrolyte wrapping [Murphy 2010]. Therefore, we investigated the ability of a weak polyelectrolyte such as polyacrylic acid (PAA) to allow electrostatic interaction between HHCc and AuNRs upon controlling ionic strength and pH. Recent studies have shown that the conformation of HHCc adsorbed on AuNPs depends on surface coverage and NP size [Aubin-Tam 2008]. To date, preservation of the native structure of HHCc has been achieved on electrodes by using appropriate self-assembled monolayers [Weidinger 2006, Królikowska 2007], but bioconjugation of colloidal AuNPs has mostly resulted in protein denaturation [Keating 1998, Aubin-Tam 2005, Aubin-Tam 2009, Brown 1996, Park 2009, Jiang 2005]. In particular, the conjugation of HHCc to AuNPs has been found to preserve the HHCc structure only when the structure has been decorated with aggregated Ag nanospheres [Keating 1998].

Since Cc can assume various misligated forms depending on pH, temperature and ionic force [Oellerich 2002, Santoni 2004, Döpner 1998, Jordan 1995, Indiani 2000], before studying the bioconiugated Cc, I undertook studies on misligated model compounds of HHCc to identify the Raman markers which allow one to distinguish the protein native structure from the misligated ones. In addition, I conducted parallel studies on human Cc (HuCc) wild type (WT) protein and some site-selected variants where the key residues have been mutated.

3.2 Materials

Sodium dithionite was obtained from Fluka Biochemika. Sodium borohydride ($NaBH_4$, ~99%), L-ascorbic acid (99%), potassium ferricyanide ($K_3[Fe(CN)_6]$, analytical grade), sodium lauryl sulfate (SDS, reagent grade), sodium dihydrogen phosphate (NaH_2PO_4, analytical grade), sodium hydrogen phosphate (Na_2HPO_4, reagent grade), hydrogen tetrachloroaurate(III) trihydrate ($HAuCl_4 \cdot 3H_2O$, 99.9%), silver nitrate ($AgNO_3$, 99.9999%), PAA (Mn ≈ 130 kDa), potassium phosphate monobasic (≥98%), potassium phosphate dibasic (≥98%), potassium chloride (≥99%), imidazole (analytical grade), HHCc ≥95% based on mol. wt. 12384) and cardiolipin, as a sodium salt from bovine heart (~98%, lyophilized powder) were purchased from Sigma-Aldrich. Stock solutions were prepared using deionized water (Millipore Milli-Q gradient A-10 system).

Expression and site-directed mutagenesis of recombinant HHCc were obtained by prof. Santucci's research group (Tor Vergata University, Rome).

Expression and site-directed mutagenesis of recombinant HuCc were obtained by prof. Fiorucci's research group (Tor Vergata University, Rome).

CTAB-capped AuNRs with a longitudinal plasmon band at 800 nm were synthesized by prof. Agostiano's research group (Bari University Aldo Moro) using a suitably modified literature procedure commonly known as the "seed mediated" growth method [Placido 2014, Khanal 2007].

The AuNRs were functionalized with PAA by exploiting electrostatic interactions in a layer-by-layer fashion (see the sketch in **Fig. 3.1**). The "as prepared" AuNRs were coated with PAA by incubation of 1 mL of AuNRs (2×10^{-9} M) and 1 mL of PAA (1.6 mg/mL, pH 7.0) for 20 min under gentle stirring. Then, this mixture was centrifuged two times at 10000 rpm for 10 min to wash the AuNRs and eliminate free PAA. Then AuNRs@PAA that precipitated upon centrifugation were dispersed in a phosphate buffer (5 mM, pH 7.0) to ensure deprotonation of the PAA carboxylate groups and confer negative charges to the NRs surface.

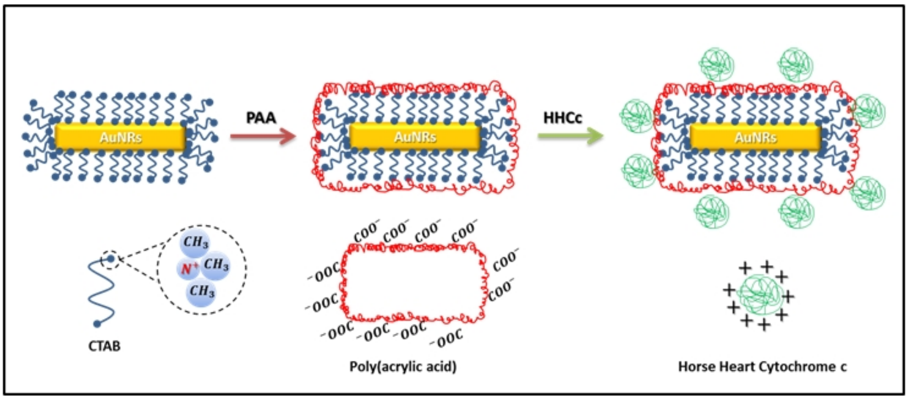

Figure 3.1: Multiple functionalization process of AuNRs with HHCc.

3.2.1 Samples preparation

HHCc bis-His model compound was prepared according to [Oellerich 2002]; briefly, 75 mM SDS (sodium dodecyl sulfate) solution was added to a HHCc solution in 50 mM phosphate buffer (pH 7.0) followed by addition of a 0.1 M imidazole solution (pH 7.0); the SDS concentration in the resulting mixture was 13-14 mM and the protein: imidazole molar ratio was 1:2500.

His-Fe-Lys ligation was obtained at pH 12.1 and 100 μM concentration.

His-Fe-OH^- misligated model compound was prepared with the HHCc K727379N (Lys72Asn/Lys73Asn/Lys79Asn) triple mutant, where no Lys residues can bind iron, at pH 12.0.

Finally, the six-coordinated high spin (6cHS) species model, i.e. the His-Fe-H_2O misligated compound, was obtained at pH 2.0 at high ionic strength (NaCl 2 M) [Jordan 1995].

Model compounds concentration in the range 25-100 μM were used for spectroscopic measurements.

The purified HuCc and its variants (Met80Ala, MA and Tyr67His/Met80Ala, YHMA) were diluted with 0.1 M phosphate buffer at pH 7.0 and/or 0.125 M citrate buffer at pH 4.3 to obtain concentrations in the 15-50 μM range at pH 7.0 or 5.5. The protein concentration was determined on the basis of the molar absorptivity (ε) of 106 mM^{-1} cm^{-1} at 409 nm for the WT protein [Margoliash 1959] and of 121.7 mM^{-1} cm^{-1} at 405 nm for the MA, and YHMA mutants [Bren 1993].

To ensure complete oxidation, 1-3 μL of a 3 mM freshly prepared $K_4[Fe(CN)_6]$ solution were added to 40 μL protein samples.

The pure ferric form of the Met80Ala (MA) mutant was obtained by a reduction and re-oxidation process. The sample solution was reduced by adding dithionite powder, excess dithionite being removed by 2 h dialysis in fresh buffer; the sample was then oxidized by adding a few grains of $K_4[Fe(CN)_6]$, excess $K_4[Fe(CN)_6]$ being removed by dialyzing overnight.

Ferrous samples were prepared by addition of 2-3 μL of a freshly prepared sodium dithionite (10 mg/mL) solution to the ferric forms (40 μL) previously degassed with nitrogen. It is noted that the double Tyr67His/Met80Ala (YHMA) variant easily oxidized at pH lower than 7.0.

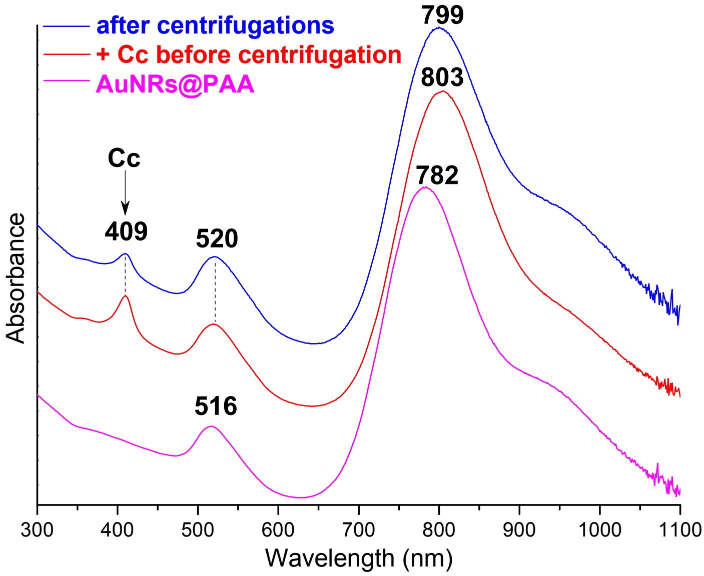

Figure 3.2: UV-Vis absorption spectra of AuNRs@PAA (pink), AuNRs@PAA mixed with the HHCc solution prior to centrifugation (red) and after the centrifugation cycles (blue).

Bioconjugation of HHCc on AuNRs has been obtained by adding 200 μL of a HHCc solution (0.5 mg/mL) in 5 mM phosphate buffer (pH 7.0) to the as prepared AuNRs@PAA solution (5×10^{-10} M). This mixture was kept under gentle stirring for 1 h. Thus, the obtained HHCc-conjugated AuNRs (AuHHCc) solution was centrifuged at 7000 rpm for 10 min, and washed with phosphate buffer (5 mM, pH 7) to remove free HHCc until no further decrease of the Soret band absorbance was observed (**Fig. 3.2**). To ensure complete oxidization of the HHCc adsorbed on the NRs, 2 μL of a $K_3[Fe(CN)_6]$ solution (1 grain in 1 mL) was added. The resulting solution was characterized by UV-Vis and RR spectroscopy, and, by others, by FT-IR spectroscopy, transmission electron microscopy (TEM) and ζ-potential measurements.

3.3 Resonance Raman studies of Cytochrome c

Cc is a single-chain heme protein lying in the inter-membrane space of the eukaryotic mitochondria, where it plays a role as an electron carrier and as a ROS scavenger [Orrenius 2007, Caroppi 2009]. It is composed of 104 amino acids and contains a heme c prosthetic group covalently attached to the polypeptide chain by two thioether bridges formed with the Cys14 and Cys17 residues [Bushnell 1990, Louie 1990, Berghuis 1992]. His18 and Met80 are the fifth and sixth axial ligands, respectively, of the heme iron in the native protein (**Fig. 3.3**).

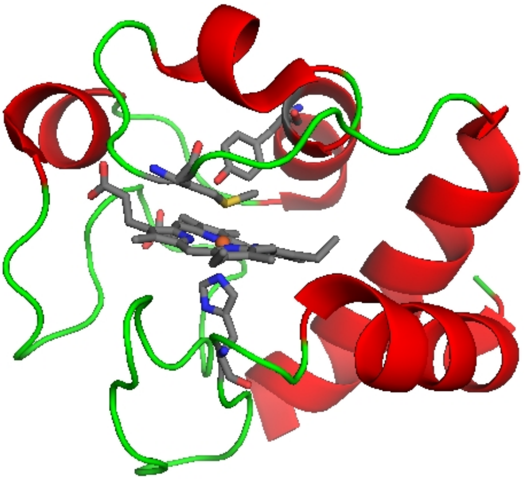

Figure 3.3: HHCc structure (PDB file: 1HRC). His18, Met80 and Tyr67 are reported in dark grey.

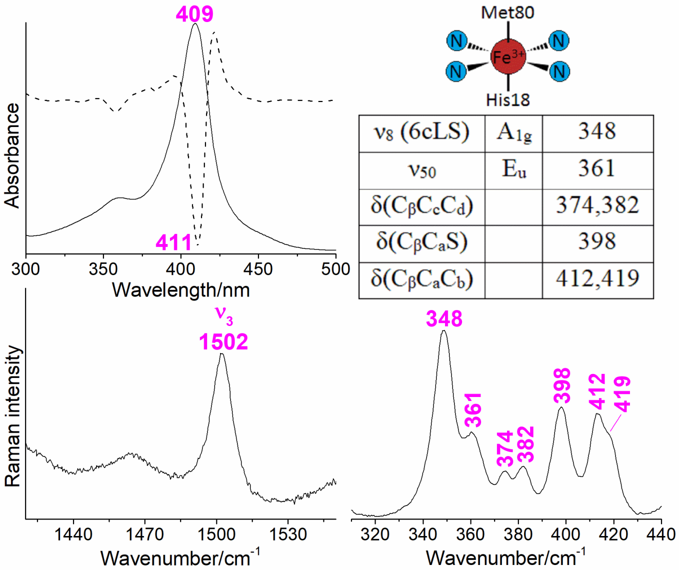

ν_8 (6cLS)	A_{1g}	348
ν_{50}	E_u	361
$\delta(C_\beta C_c C_d)$		374,382
$\delta(C_\beta C_a S)$		398
$\delta(C_\beta C_a C_b)$		412,419

Figure 3.4. Absorption spectrum in the Soret region with its second derivative (top, left) and RR (λ_{exc} = 406.7 nm) spectra in the ν_3 (bottom, left) and fingerprint (300-440 cm^{-1}) (bottom, right) regions of native HHCc. Experimental conditions: 5 mW laser power on the sample, average of 4 spectra with 20 minutes integration time.

The main features of the UV-Vis absorption and RR spectra of the WT HHCc are shown in **Fig. 3.4** and are identical to those reported for yeast Cc and HHCc [Hu 1993], typical of a 6-coordinated low spin (6cLS) species with a His-Fe-Met coordination state.

3.3.1 Misligated model compounds

Cc is found in its native form at pH 7.0 and low ionic strength, but extensive studies demonstrated that Cc can adopt various misligated states depending on the environmental conditions:

- at pH 2.0 and high ionic force, the Met80 residue is substituted by a water molecule, resulting in a 6cHS aquo form, His-Fe-H_2O [Jordan 1995, Indiani 2000];
- between pH 9 and 11 a His-Fe-Lys form is observed, where Met80 is substituted by Lys72, 73 or 79 [Döpner 1998];
- at pH > 11, the His-Fe-Lys species is in equilibrium with a His-Fe-OH^- form [Döpner 1998];
- in presence of SDS micelles, a bis-His coordination state is observed, where His26 or 33 substitute Met80 [Oellerich 2002, Santoni 2004].

The substitution of the native Met80 ligand is associated with an increase of heme planarity due to the relaxation of the tertiary structure, causing many changes in the absorption and RR spectra that are observed for all the misligated forms mentioned above, i.e.:

(a) blue-shift of the Soret band,
(b) loss of the CT band at 695 nm
(c) upshift of the core-size marker bands (such as ν_3, see **Fig. 3.4**),
(d) weakening or disappearing of the out-of-plane bending modes.

Nevertheless, each misligated species shows a unique spectral pattern in the fingerprint region of the RR spectrum (300-440 cm^{-1}), hence I prepared four HHCc misligated model compounds to identify the Raman markers for each non-native forms.

His-Fe-His [Othman 1994, Oellerich 2002, Santoni 2004] (**Fig. 3.5**): the ν_8 band downshifts from 348 cm^{-1} of the native form to 344 cm^{-1} and the $\delta(C_\beta C_a C_b)$ band at 418 cm^{-1} intensity increases. Moreover, a new band appears at 400 cm^{-1} which is assigned to the ν_{asym}(Fe-Im$_2$) mode, that is the specific marker of the bis-His coordination, as previously observed for the N-fragment of Cc and Cc″ [Santoni 2004].

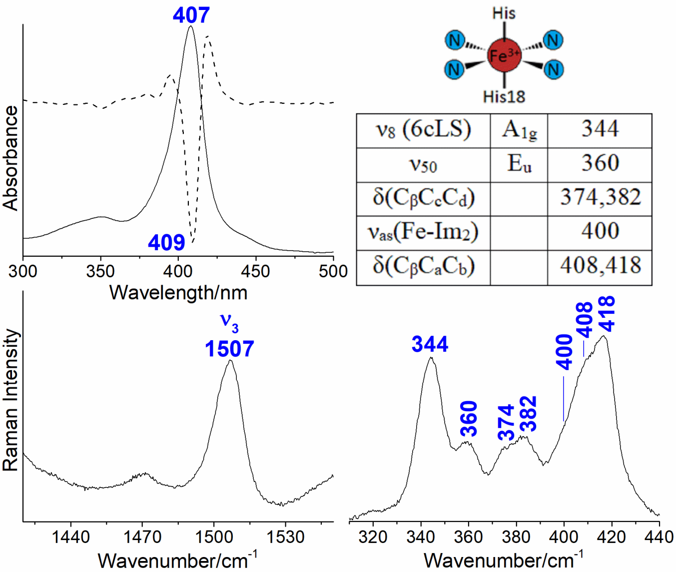

ν_8 (6cLS)	A_{1g}	344
ν_{50}	E_u	360
$\delta(C_\beta C_c C_d)$		374,382
ν_{as}(Fe-Im$_2$)		400
$\delta(C_\beta C_a C_b)$		408,418

Figure 3.5: Absorption spectrum in the Soret region with its second derivative (top, left) and RR (λ_{exc} = 406.7 nm) spectra in the ν_3 (bottom, left) and fingerprint (300-440 cm^{-1}) (bottom, right) regions of the His-Fe-His model compound. Experimental conditions: 10 mW laser power on the sample, average of 12 spectra with 60 minutes integration time.

His-Fe-Lys [Döpner 1998] (**Fig. 3.6**): the ν_8 band downshifts of from 348 cm^{-1} of the native form to 343 cm^{-1}, a new band at 384 cm^{-1} appears and is assigned to the ν(Fe-N$_{Lys}$) stretching vibration. Moreover, the $\delta(C_\beta C_a S)$ thioether vibration mode splits, giving bands at 394 and 401 cm^{-1}, and the $\delta(C_\beta C_a C_b)$ band at 412 cm^{-1} increases.

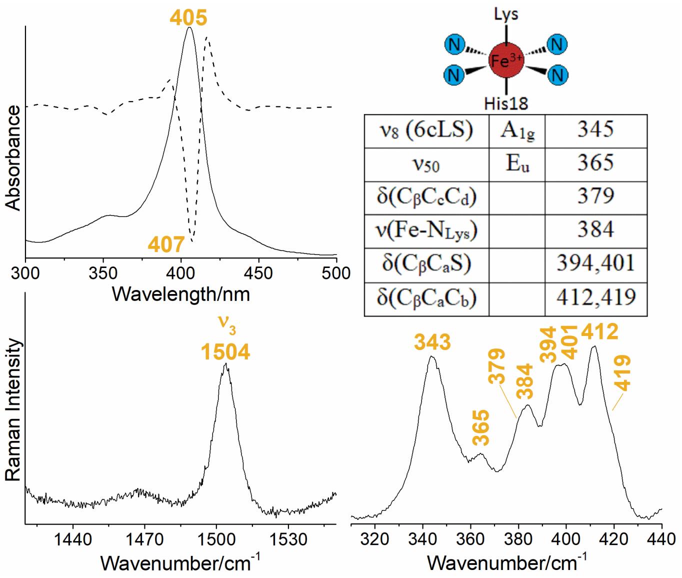

ν_8 (6cLS)	A_{1g}	345
ν_{50}	E_u	365
$\delta(C_\beta C_c C_d)$		379
$\nu(Fe\text{-}N_{Lys})$		384
$\delta(C_\beta C_a S)$		394,401
$\delta(C_\beta C_a C_b)$		412,419

Figure 3.6: Absorption spectrum in the Soret region with its second derivative (top, left) and RR (λ_{exc} = 406.7 nm) spectra in the ν_3 (bottom, left) and fingerprint (300-440 cm^{-1}) (bottom, right) regions of the His-Fe-Lys model compound. Experimental conditions: 5 mW laser power on the sample, average of 11 spectra with 55 minutes integration time (left) and average of 20 spectra with 10 minutes integration time.

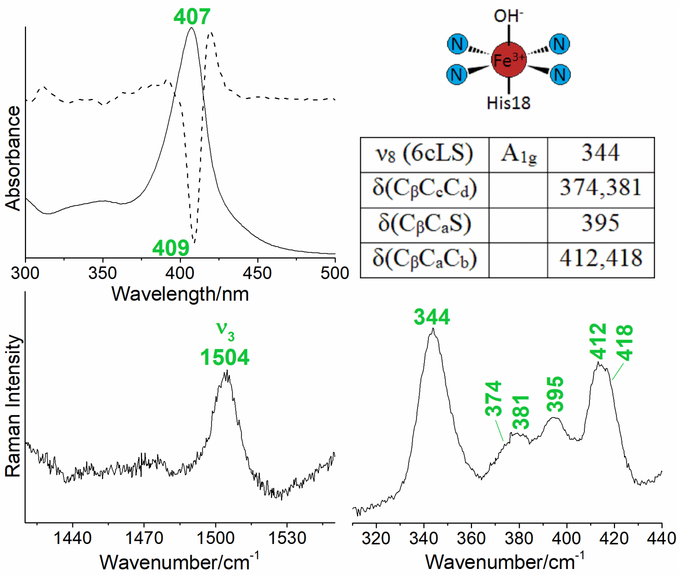

ν_8 (6cLS)	A_{1g}	344
$\delta(C_\beta C_c C_d)$		374,381
$\delta(C_\beta C_a S)$		395
$\delta(C_\beta C_a C_b)$		412,418

Figure 3.7: Absorption spectrum in the Soret region with its second derivative (top, left) and RR (λ_{exc} = 406.7 nm) spectra in the ν_3 (bottom, left) and fingerprint (300-440 cm^{-1}) (bottom, right) regions of the His-Fe-OH$^-$ Cyt c model compound. Experimental conditions as reported in Figure 3.15.

His18-Fe-OH$^-$ [Döpner 1998, Battistuzzi 2012] (**Fig. 3.7**): downshift of the ν_8 band from 348 cm^{-1} of the native form to 344 cm^{-1} and a significant intensity loss of the thioether bending mode $\delta(C_\beta C_a S)$ at 395 cm^{-1} are observed.

His-Fe-H$_2$O [Jordan 1995] (**Fig. 3.8**): a mixture of 6cHS aquo (second derivative Soret band at 401 nm, ν_3 at 1481 cm^{-1}) and 6cLS (second derivative Soret band at 410 nm and ν_3 at 1504, cm^{-1}) species is observed. In the fingerprint region the ν_8 mode is at very low wavenumber (342 cm^{-1}), and the $\delta(C_\beta C_c C_d)$ propionate bending modes give rise to very intense bands at 378 and 385 cm^{-1}.

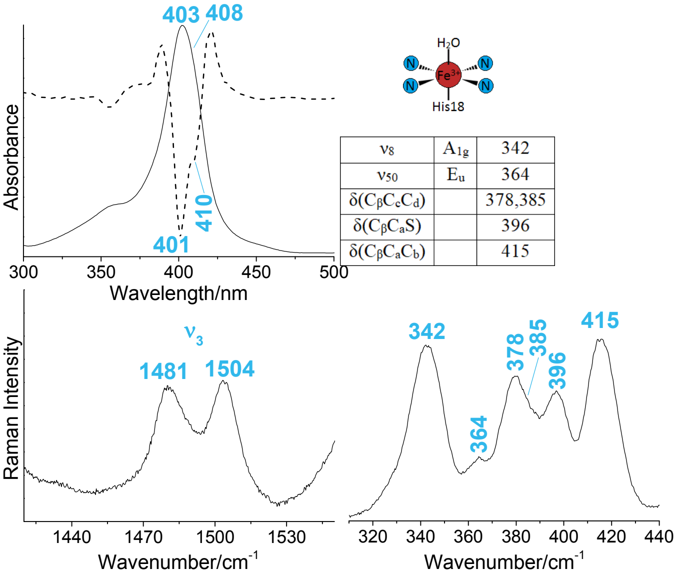

ν_8	A_{1g}	342
ν_{50}	E_u	364
$\delta(C_\beta C_c C_d)$		378,385
$\delta(C_\beta C_a S)$		396
$\delta(C_\beta C_a C_b)$		415

Figure 3.8: Absorption spectrum in the Soret region with its second derivative (top, left) and RR (λ_{exc} = 406.7 nm) spectra in the ν_3 (bottom, left) and fingerprint (300-440 cm^{-1}) (bottom, right) regions of the His-Fe-H$_2$O model compound. Experimental conditions: laser power at the sample 10 mW; average of 8 spectra with 40 min integration time (left) and average of 12 spectra with 60 min integration time (right).

3.3.2 Human Cytochrome c

In parallel, I conducted a study on HuCc WT protein and its variants MA and YHMA. Cc is in fact a very interesting protein, because of the multiple functions that it carries out in response to different cell stimuli. In particular, these different functions seem to be regulated also by protein conformational changes. Direct interaction with cardiolipin (CL), a phospholipid of the mitochondrial membrane, gives rise to a more flexible tertiary structure, disruption of the Fe-Met80 ligation, gain of peroxidase activity and release into the cytosol [Ow 2008, Santucci 2010] with consequent apoptosis triggering. In this process, the position of Met80 is thought to be crucial in conferring different functionality to Cc.

Met80 is located in the surface heme crevice loop (residues 71-85), the most highly conserved segment of the primary structure of Cc. The dynamics of the heme crevice loop are regulated by its link with the 40-57 loop through Tyr67. In fact, Tyr67, a highly conserved residue, forms a hydrogen bond network with Met80 and other conserved residues (such as Asn52 and Thr78). This hydrogen bond network helps to maintain the sulfur atom of Met80 in the right position as the heme iron ligand, thus also controlling the redox potential of the protein. Moreover, mutations at the Tyr67 position have been previously shown to lead to a rearrangement of the distal portion of the heme cavity, depending on the type of substituting residue [Ying 2009, Casalini 2010]. In HuCc, substitution of Tyr67 by Arg leads to the cleavage of the Fe-Met80 bond, while substitution by His affects the heme pocket to a much lower extent [Patriarca 2012, Tognaccini 2016]. To have a better understanding of the possible rearrangements of the distal cavity when mutation of key residues occur, I used the acquired knowledge on the misligated species to study HuCc WT protein and its variants MA and YHMA by UV-Vis and RR spectroscopies.

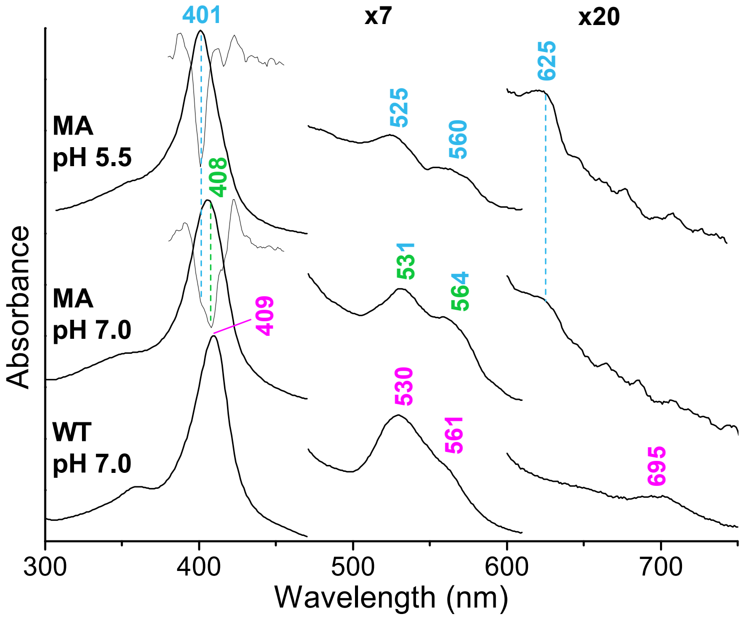

Figure 3.9: UV-Vis absorption and second derivative spectra of ferric WT HuCc at pH 7.0 together with its MA mutant at pH 7.0 and pH 5.5. The 470-610 and 600-750 nm regions are expanded 7-fold and 20-fold, respectively.

3.3.2.1 Met80Ala mutant

At neutral pH, the MA mutant UV-Vis electronic absorption spectrum is characterized by the absence of the CT band at 695 nm (indicative of the Fe-Met80 bond, [Stellwagen 1974]) and the Soret maximum at 408 nm (**Fig. 3.9**). In addition, the RR core size marker band wavenumbers are slightly upshifted compared to the WT (**Fig. 3.10**, A).

These spectral variations indicate that the main species is a 6cLS and that Met80 has been replaced by another internal ligand, which induces the formation of a more planar heme [Indiani 2000, Döpner 1998, Sinibaldi 2003, Oellerich 2002, Battistuzzi 2012]. The presence of a 6c high spin (HS) H_2O-Fe-His aquo species is also noted, as indicated by the shoulder of the Soret band at 401 nm, the band at 625 nm, assigned to the CT1 band, and the core size marker bands at 1480 and 1570 cm^{-1}, assigned to ν_3 and ν_2, respectively.

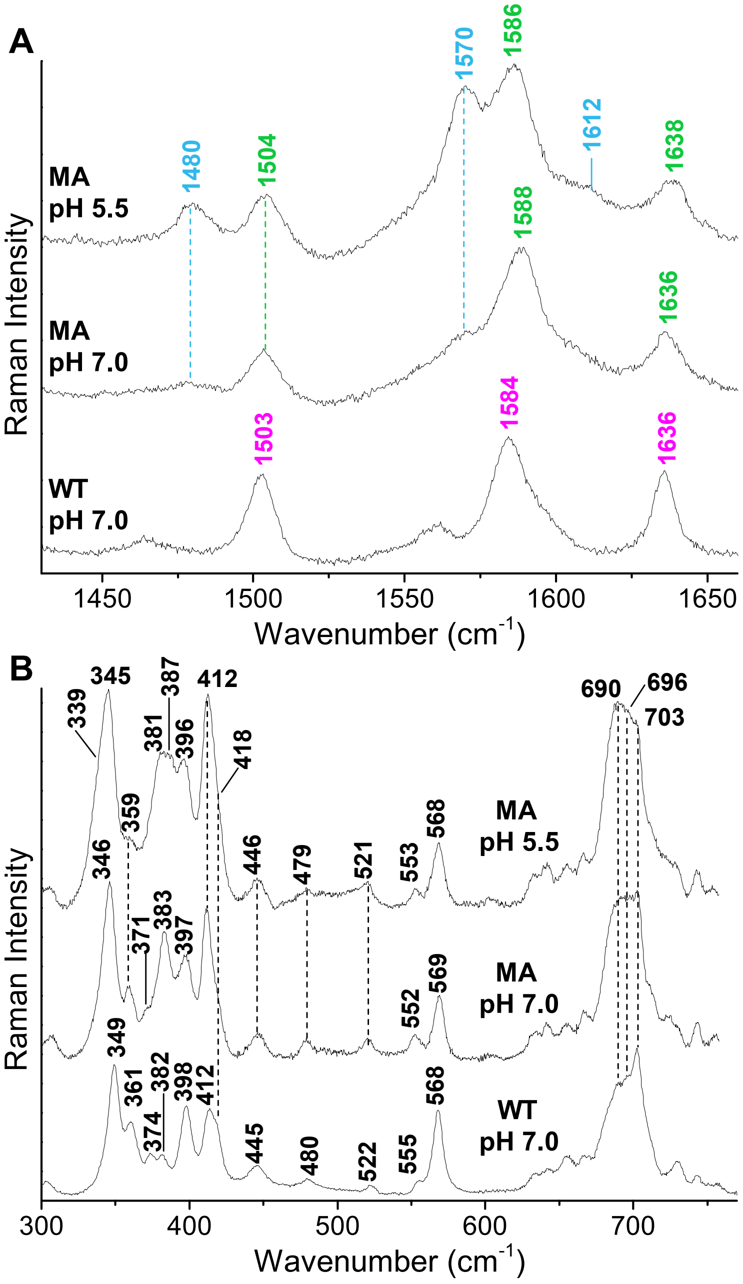

Figure 3.10: RR spectra in the high (panel A) and low (panel B) frequency regions of ferric WT HuCc at pH 7.0 together with its MA mutant at pH 7.0 and pH 5.5. Experimental conditions: 406.7 nm excitation wavelength, 5 mW laser power at the sample, average of 6 spectra with 30 minutes integration time.

In the RR fingerprint region (**Fig. 3.10**, B), the downshift of the ν_8 band from 348 (WT) to 346 cm^{-1} and the intensity loss of the thioether bending mode $\delta(C_\beta C_a S)$ at 397 cm^{-1}, are reminiscent of the markers of the His-Fe-OH^- 6cLS species [Döpner 1998], that is the main one at pH 7.0 (**Fig. 3.10**, B).

This species decreases upon lowering the pH, as observed at pH 5.5, where the 6cHS aquo species becomes predominant, as indicated by the Soret maximum that completely shifts to 401 nm, the RR core size marker bands that gain intensity, and the appearance of the weak ν_{10} band at 1612 cm^{-1} (**Fig. 3.9** and **3.10**, A). In fact, at pH 5.5, protonation of the OH^- axial ligand results in a mixture of a His-Fe-OH^- 6cLS and a 6cHS aquo species, the latter increasing at the expense of the hydroxo form.

Upon reduction, the UV-Vis spectrum of the MA mutant (**Fig. 3.11**) is characteristic of a mixture of two species, a 6cLS heme (bands at 412, 521, and 550 nm) and a 5cHS form (434 and 565 nm), indicating that the sixth coordination position of the heme iron is partially occupied by an internal ligand.

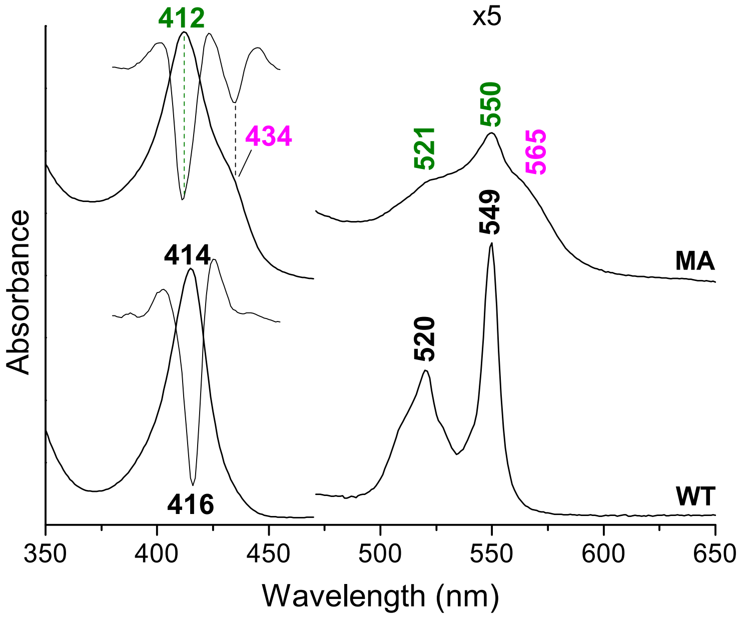

Figure 3.11: Electronic absorption spectra of ferrous WT HuCc at pH 7.0 and of its MA mutant at pH 5.9. The 470-650 region has been expanded 5-fold.

Accordingly, the presence of a small amount of 6cLS species is observed in the high frequency RR spectrum, obtained in resonance (413.1 nm) with the LS form (**Fig. 3.12**, B, spectrum b’). Conversely, the 5cHS species, becomes predominant with excitation at 441.6 nm, i.e. in resonance with the Soret band of the 5cHS heme at 434 nm, (**Fig. 3.12**, B, spectrum c’).

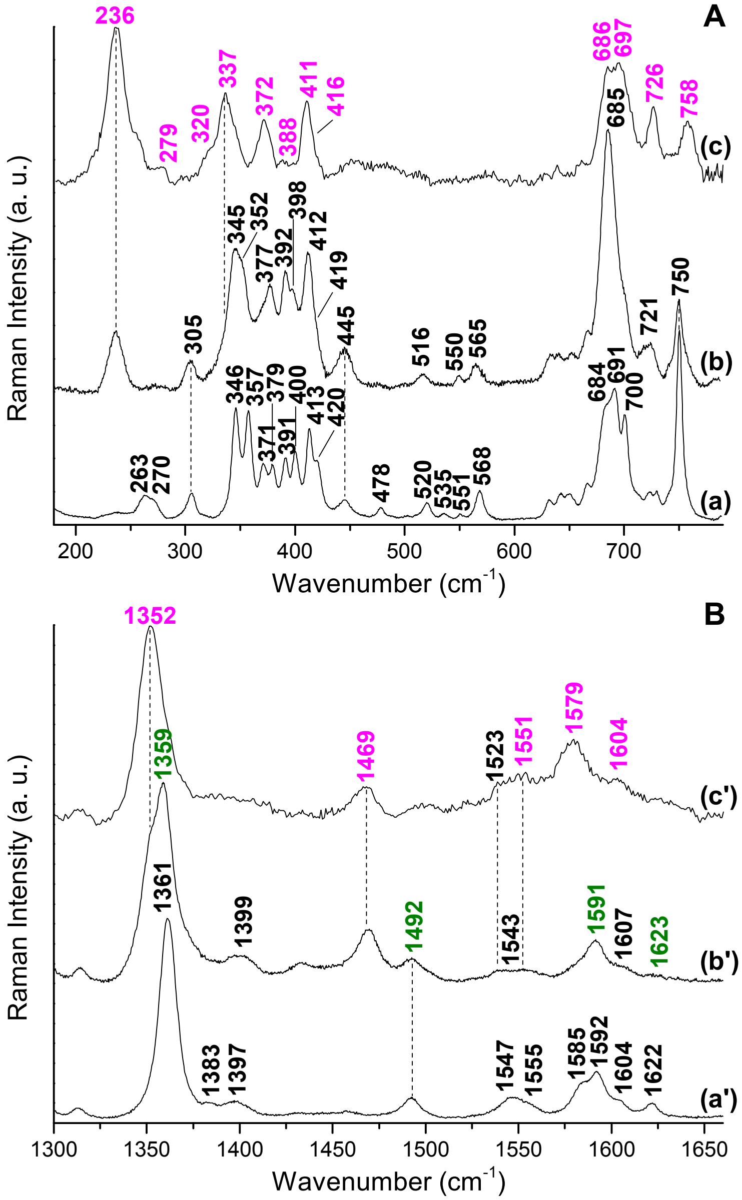

Figure 3.12: RR spectra in the low (panel A) and in the high (panel B frequency regions of ferrous WT HuCc at pH 7.0 (a and a') and of its MA mutant at pH 5.9 (b, b', c and c'). Experimental conditions: 413.1 nm excitation wavelength. (a, a') laser power at the sample 5 mW, average of 4 spectra with 20 min integration time. (b, b'), laser power at the sample 2 mW, (b'), average of 12 spectra with 60 min integration time. 441.6 nm excitation wavelength: (c, c'), laser power at the sample 10 mW, average of 4 spectra with 20 min integration time.

This effect is markedly evident in the low frequency region as the spectra obtained with the two excitation wavelengths are very different (**Fig. 3.12**, A, spectra b and c). In the 441.6 nm spectrum the strongest band at 236 cm^{-1}, which becomes very weak for 413.1 nm excitation, is tentatively assigned to the ν(Fe-Im) stretching mode, since it is expected to give rise to a strong band in 5cHS ferrous heme proteins upon excitation in the Soret band [Kitagawa 1988]. The nature of the internal ligand responsible for the minor 6cLS species is unclear.

The complete vibrational assignment of the RR spectra of the MA mutant in its ferric and ferrous forms is reported in **Table 3.1**.

Table 3.1. Vibrational mode assignment of ferric and ferrous WT HuCc and its MA mutant at pH 7.0 and pH 5.5-6.0 [Choi 1982, Hu 1993, Othman 1994, Othman 1998].

Mode	***Symmetry***	**Fe^{3+}**			**Fe^{2+}**	
		WT	**M80A**		**WT**	**M80A**
		pH 7.0	*pH 7.0*	*pH 5.5*	*pH 7.0*	*pH 6.0*
ν(Fe-Im)						236
γ_{24}	E_g	230				
ν_9	A_{1g}	273			263, 270	
ν_{51}	E_u	303			306	305
ν_8 (5cHS)	A_{1g}		339			337
ν_8 (6cLS)	A_{1g}	349	346		346	345
ν_{50}	E_u	361	359		357	352
$\delta(C_\beta C_c C_d)$ (5cHS)						372,388
$\delta(C_\beta C_c C_d)$		374,	371,	381,	371,	377

		382	383	387	379	
$\delta(C_\beta C_a S)$		398	397	396	391, 400	392, 398
$\delta(C_\beta C_a C_b)$ (5cHS)						411,416
$\delta(C_\beta C_a C_b)$		413, 418	412, 418		413, 420	412, 419
γ_{22}	E_g	445	446		445	445
ν_{33}		480	479		478	
γ_{12}	B_{1u}	522	521		520	516
ν_{49}	E_u				535	
γ_{21}	E_g	555, 568	552, 569	553, 568	551, 568	550, 565
ν(C-S)		690,696	690,696		684,691	685
ν(C-S) (5cHS)						686
ν_7 (5cHS)	A_{1g}					697
ν_7	A_{1g}	703	703		700	700
ν_{15}	B_{1g}				750	750
ν_{15} (5cHS)	B_{1g}					758
ν_{21}	A_{2g}	1317	1318		1313	1314
ν_4 (5cHS)	A_{1g}					1352
ν_4 (6cHS)	A_{1g}		1373			
ν_4 (6cLS)	A_{1g}	1373	1377		1361	1359
ν_{20}	A_{2g}				1383	
ν_{29}	B_{2g}	1406	1404		1397	1399
ν_{28}	B_{2g}	1465				
ν_3 (5cHS)	A_{1g}					1469
ν_3 (6cHS)	A_{1g}		1480			
ν_3 (6cLS)	A_{1g}	1503	1504		1492	1492
ν_{38} (5cHS)	E_u					1523
ν_{38} (6cLS)	E_u	1547			1555	
ν_{11} (5cHS)	B_{1g}					1551
ν_{11} (6cLS)	B_{1g}	1560			1547	1553

ν_2 (6cHS)	A_{1g}		1570			
ν_2 (5cHS)	A_{1g}					1579
ν_{19} (6cLS)	A_{2g}				1585	
ν_2 (6cLS)	A_{1g}	1584	1588	1586	1592	1591
ν_{37}	E_u	1596	1603		1604	1607
ν_{10} (5cHS)	B_{1g}					1604
ν_{10} (6cHS)	B_{1g}		1612			
ν_{10} (6cLS)	B_{1g}	1636	1636	1638	1622	1623

3.3.2.2 Tyr67His/Met80Ala double mutant

The double YHMA mutation gives rise to the appearance of two new species, a misligated 6cLS heme, characterized by a Soret band at 409 nm, and a 6cHS aquo form, with the Soret band at 397 nm and CT1 band at 630 nm, which increases at lower pH (**Fig. 3.13**, panel A). In the high frequency RR spectra (**Fig. 3.13**, panel B, spectrum b), the core size marker bands of the 6cLS species have frequencies higher than those of the WT (**Fig. 3.13**, panel B spectrum a) but they differ from those of the MA mutant (**Fig. 3.10**, panel A) and are reminiscent of those observed for His-Fe-His ligation [Oellerich 2002]. Moreover, a curve fitting analysis (**Fig. 3.14**) confirms the presence of a 5cHS form. In the RR low frequency region (**Fig. 3.15**, spectrum b), the YHMA spectrum shows marked changes compared to the WT and is very similar to those of imidazole-microperoxidase [Othman 1994] and of N-fragment of Cc and Cc″ [Santoni 2004], that have been assigned to a bis-His coordination. In fact, i) the shape of the 330-430 cm^{-1} region, called “fingerprint region” due to its sensitivity to the heme ligation; ii) the decrease in intensity of the out-of-plane bending modes [γ_{22} (445 cm^{-1}), γ_{12} (522 cm^{-1}), γ_{21} (568 cm^{-1}) and γ_5 (730 cm^{-1})] and of the propionyl bending mode [$\delta(C_\beta C_c C_d)$, at 374 cm^{-1}]; iii) the downshift of the ν_8 band to 344 cm^{-1} with the concomitant broadening and intensity decrease; iv) the presence of the very intense $\delta(C_\beta C_a C_b)$ band at 417 cm^{-1}; v) the shift of the ν_7 band, which overlaps with the ν(C-S) stretching mode at 696 cm^{-1}, are all consistent with this assignment.

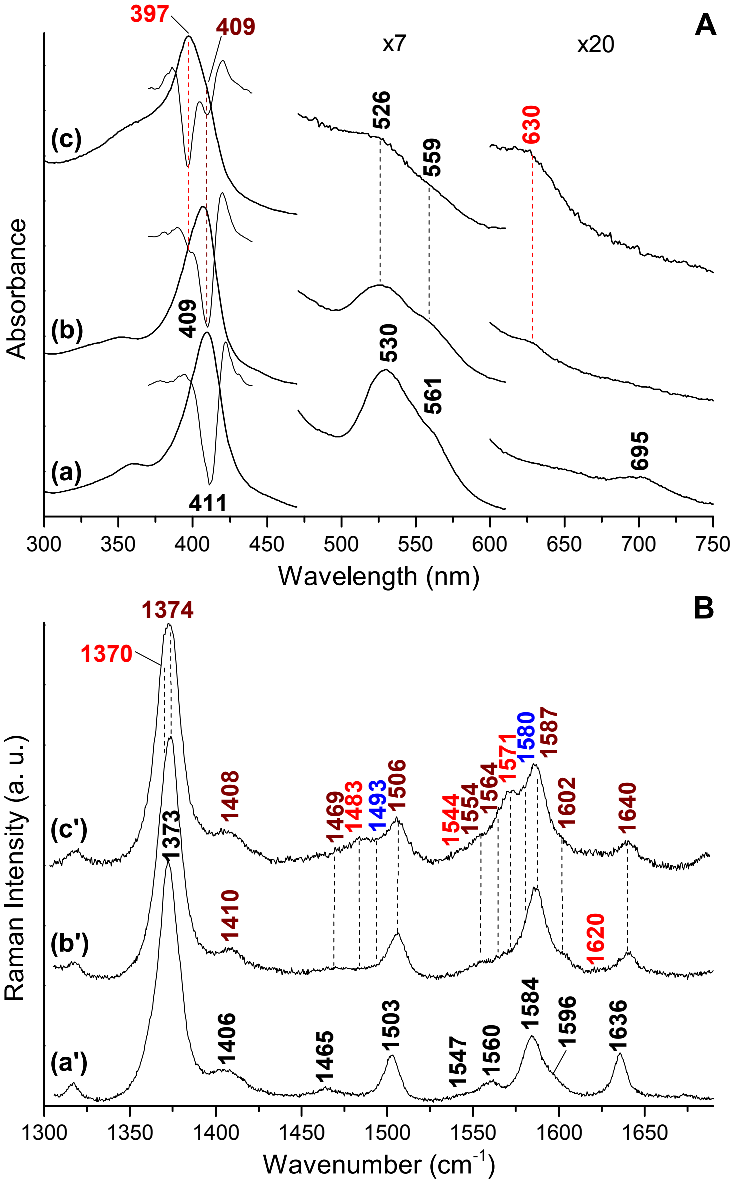

Figure 3.13: Comparison of the electronic absorption (Panel A) and RR spectra (Panel B) in the high frequency region of ferric WT HuCc at pH 7.0 (a, a') together with its YHMA mutant at pH 7.0 (b, b') and pH 5.5 (c, c'). The 470-610 and 600-750 nm regions are expanded 7- and 20-fold, respectively. RR experimental conditions: 406.7 nm excitation wavelength, laser power at the sample 5 mW (a') and 2 mW (b', c'), average of 6 spectra with 30 min integration time.

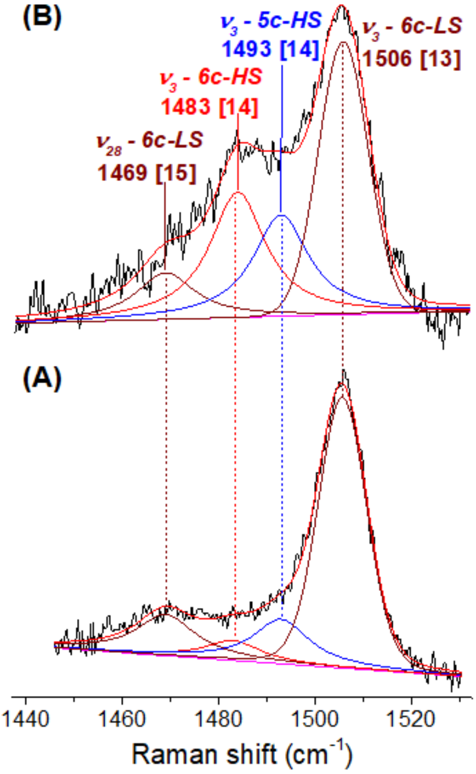

Figure 3.14: Curvefitting analysis of the 1440-1530 cm^{-1} zone of the YHMA mutant at pH 7.0 (A) and 5.0 (B). The bandwidths are indicated in brackets.

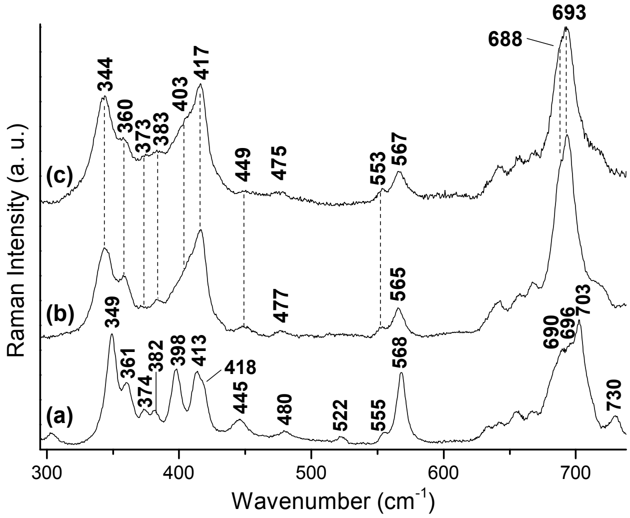

Figure 3.15: Comparison of the RR spectra in the low frequency region of ferric WT HuCc at pH 7.0 (a) together with its YHMA mutant at pH 7.0 (b) and pH 5.5 (c) and Cc bis-His model (d). Experimental conditions: 406.7 nm

excitation wavelength, laser power at the sample 5 mW (a, d) and 2 mW (b, c), average of 6 spectra with 30 min integration time.

Accordingly, the curve fitting analysis of the pH 7.0 double mutant spectrum (**Fig. 3.16**) shows the presence of a new band at 403 cm^{-1}, assigned to the bis-His asymmetric ν_{as}(Fe-Im$_2$) stretching mode, the specific marker of the bis-His coordination [Santoni 2004]. Since coordination of His26 or His33 would require a change in the tertiary structure, it is very likely that His67, which replaces Tyr67 in the distal cavity, binds the iron atom.

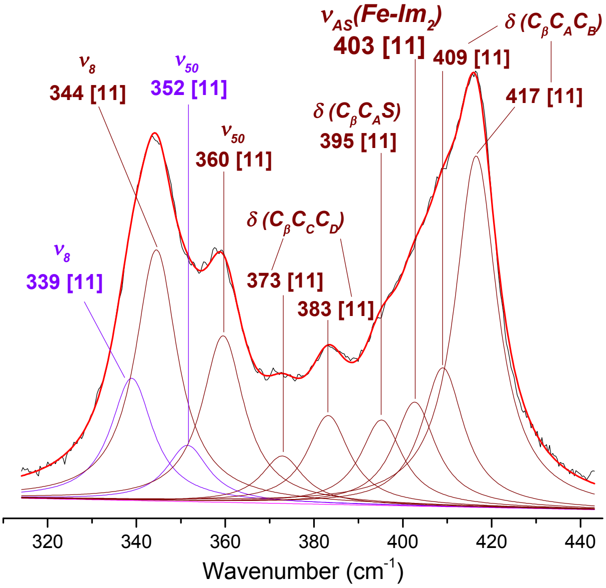

Figure 3.16: Curve fitting of the RR spectrum reported in Fig. 3.9 (spectrum b) in the 300-440 cm^{-1} region of YHMA at pH 7.0. Bandwidths are reported in brackets.

Upon reduction, the electronic absorption spectrum of the YHMA mutant is very similar to that of the WT (**Fig. 3.17**, left panel). However, the 6cLS RR spectrum in the high frequency region (**Fig. 3.18**, right panel) is characterized by core size marker bands that are up-shifted by 2-4 cm^{-1}. In addition, the bands at 1585 (ν_{19}) and 1547 (ν_{11}) cm^{-1}, which are anomalously intense in the WT spectrum due to the ruffling distortion of the heme [Shelnutt 1998], almost disappear in the mutant spectrum. Therefore, as for the ferric state, these changes suggest the formation of a misligated 6cLS ferrous form [Othman 1998].

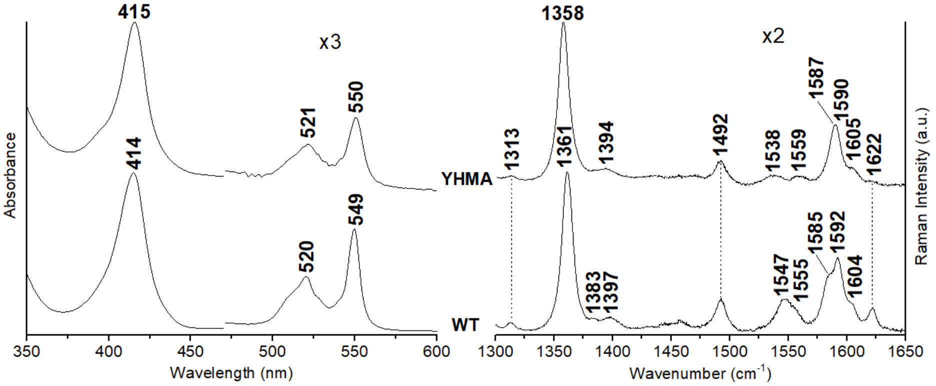

Figure 3.17: Electronic absorption and RR spectra of ferrous YHMA and WT HuCc at pH 7.0. Left: electronic absorption spectra, the 470-650 nm region is expanded 3-fold. Right: RR spectra in the high frequency region. Experimental conditions: excitation wavelength 413.1 nm; (WT): laser power at the sample 5 mW; average of 4 spectra with 20 min integration time; (YHMA): laser power at the sample 2 mW; average of 8 spectra with 40 min integration time. The 1450–1650 cm^{-1} region is expanded 2-fold.

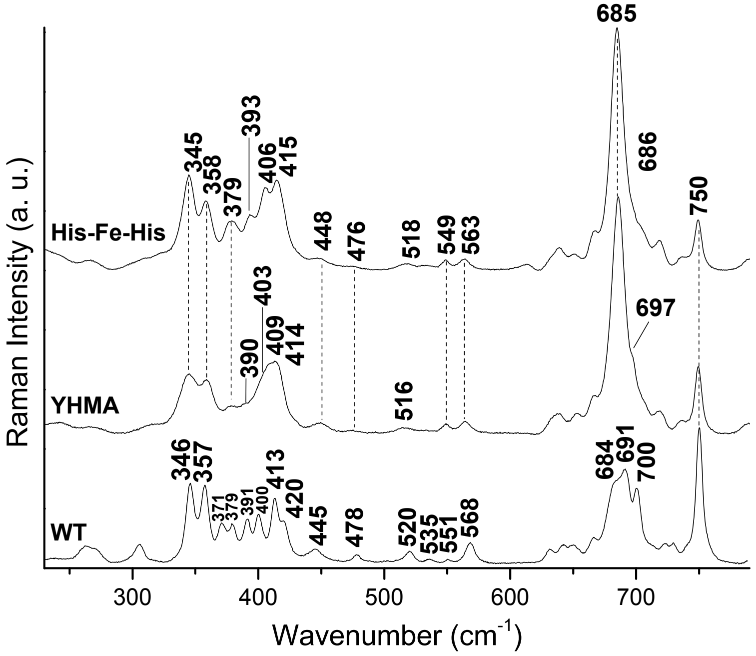

Figure 3.18: Comparison of the RR spectra in the low frequency region of ferrous WT and YHMA at pH 7.0 together with the bis-His Cc model. Experimental conditions: 413.1 nm excitation wavelength; WT, His-Fe-His: laser power at the sample 5 mW, average of 4 spectra with 20 min integration

time; YHMA: laser power at the sample 2 mW, average of 8 spectra with 40 min integration time.

Accordingly, the low frequency region spectrum (**Fig. 3.18**) shows pronounced changes in the relative intensities and frequencies of the bands compared to the WT (**Fig. 3.18**), similarly to what observed for the ferric form. This could suggest that even in the reduced form His67 replaces the Met80 ligand, giving rise to a His-Fe-His18 6cLS species. Since no literature data on bis-His coordinated ferrous forms were reported, I obtained the low frequency RR spectrum of the reduced His-Fe-His HHCc model, according to [Oellerich 2002] (**Fig. 3.18**). Many similarities are observed between the double mutant and the model spectrum, like the overall shape of the fingerprint region, the decrease in intensity of the out-of-plane bending modes γ_{22} (448 cm^{-1}), γ_{21} (563 cm^{-1}) and of the $\delta(C_\beta C_c C_d)$ and $\delta(C_\beta C_a S)$ bending modes at 379 and 390 cm^{-1} respectively, the shift of the ν_7 band, which overlaps with the ν(C-S) stretching mode at 685 cm^{-1} and the decrease of the ν_{15} at 750 cm^{-1}, thus confirming the assignment to a His-Fe-His coordination state.

The complete vibrational assignment of the RR spectra of the YHMA mutant in its ferric and ferrous forms is reported in **Table 3.2**.

Table 3.2. Vibrational mode assignment of ferric and ferrous WT human cyt c and its YHMA mutant at pH 7.0 and pH 5.0-6.0 [Choi 1982, Hu 1993, Othman 1994, Othman 1998].

Mode	***Symmetry***	**Fe^{3+}**			**Fe^{2+}**		
		WT	**Y67H/M80A**		**WT**	**Y67H/M80A**	
		pH 7.0	*pH 7.0*	*pH 5.0*	*pH 7.0*	*pH 7.0*	*pH 6.0*
ν_{34}	B_{2g}				178		
ν_{53}	E_u						
γ_{24}	E_g	230					
ν_9	A_{1g}	273	274	272	263,270	267	269
ν_{51}	E_u	303			306		
ν_8	A_{1g}	349	344		346	345	344
ν_{50}	E_u	361	360		357	359	357
$\delta(C_\beta C_c C_d)$		374,	373, 383		371,	379	380

		382			379		
$\delta(C_{\beta}C_{a}S)$		398	395		391, 400	390	
ν_{as}(Fe-Im$_2$)			403			403	
$\delta(C_{\beta}C_{a}C_{b})$		413,418	409,417		413,420	409,414	
γ_{22}	E_g	445	449		445	448	
ν_{33}		480	477	475	478	476	475
γ_{12}	B_{1u}	522			520	516	518
ν_{49}	E_u				535		
γ_{21}	E_g	555, 568	553, 566	553, 567	551, 568	549, 564	
ν(C-S)		690, 696	688, 693		684, 691	686	
ν_7	A_{1g}	703			700	697	
γ_{11}	B_{1u}				723		
γ_5	A_{2u}	730			729		
ν_{15}	B_{1g}				750	750	
ν_{21}	A_{2g}	1317	1318		1313	1313	1314
ν_4 (6cHS)	A_{1g}		1370				
ν_4 (6cLS)	A_{1g}	1373	1374		1361	1358	1360
ν_{20}	A_{2g}				1383		
ν_{29}	B_{2g}	1406	1410	1408	1397	1394	
ν_{28}	B_{2g}	1465	1469		1459		
ν_3 (6cHS)	A_{1g}		1483				
ν_3 (5cHS)	A_{1g}		1493				
ν_3 (6cLS)	A_{1g}	1503	1506		1492	1492	1493
ν_{11} (6cHS)	B_{1g}			1544			
ν_{11} (5cHS)	B_{1g}		1554				
ν_{38}	E_u	1547	1554		1555	1559	
ν_{11} (6cLS)	B_{1g}	1560	1564		1547	1538	1543
ν_2 (6cHS)	A_{1g}		1571				

ν_2 (5cHS)	A_{1g}		1580		
ν_{19} (6cLS)	A_{2g}			1585	
ν_2 (6cLS)	A_{1g}	1584	1587	1592	1590
ν_{37}	E_u	1596	1602	1604	1605
ν_{10} (6cHS)	B_{1g}		1620		
ν_{10} (6cLS)	B_{1g}	1636	1640	1622	1622

3.4 Bioconjugation of Cytochrome c on gold nanorods

The surface properties of the AuNRs have been modified by means of a layer-by-layer electrostatic functionalization procedure. CTAB-coated AuNRs with an aspect ratio of 4.2 ± 0.4 (diameter = 14.1 ± 1.6 nm; length = 58.5 ± 5.8 nm) have been synthesized by using the seed-mediated approach, resulting in NRs coated with a CTAB bilayer, which ensures a very good particle dispersion in water, thus minimizing the risk of aggregation phenomena. The UV-Vis spectrum of colloidal AuNRs is reported in **Fig. 3.19** (black) and shows the typical two plasmon bands located at 516 and 800 nm, corresponding to transverse and longitudinal plasmon modes, respectively. Moreover, the longitudinal plasmon band is quite narrow and intense compared with the transverse band, suggesting a high yield of nearly monodisperse AuNRs.

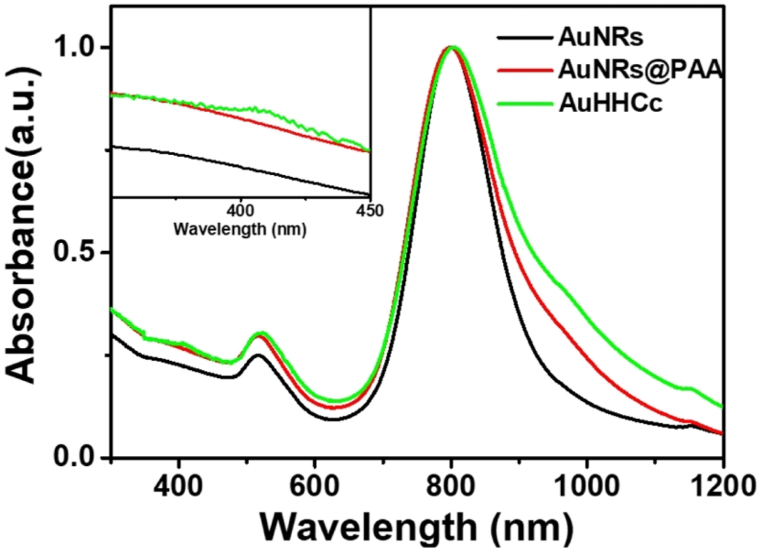

Figure 3.19: UV-vis absorption spectra of AuNRs (black), AuNRs coordinated by PAA (red), and HHCc-conjugated AuNRs (AuHHCc, green). The inset shows a zoom of the spectra within the 350-450 nm wavelength range. The calculated HHCc concentration of the AuHHCc solution is about 10^{-6} M.

The ammonium-terminated polar heads of the surfactants interact with water molecules in the surrounding environment, conferring a positive charge to the AuNRs, as demonstrated by the ζ-potential measurements (**Table 3.3**). The positively charged quaternary ammonium heads of the CTAB molecules coating the AuNRs promote the electrostatic binding of the positively charged HHCc by interaction with the negatively charged PAA (see the sketch in **Fig. 3.1**). Such a polyelectrolyte wrapping of the NRs is, in principle, able to limit the possible release of the CTAB molecules of the bilayer coating the NR surface, thus representing a safe "glue" compatible with the presence of biomolecules. Moreover, PAA, being a weak polyelectrolyte, allows interaction between HHCc and AuNRs to be modulated by the tuning of ionic strength and pH, thus obtaining the most-suited wrap for the AuNRs. The charge density of PAA is a function of the solution pH and, therefore, affects the arrangement of the chains and their conformation upon surface adsorption [Burke 2004]. In fact, for pH > pKa (PAA, pKa = 4.8), many of the PAA carboxylic groups are deprotonated, thus inducing stretching of the polymeric chains because of reciprocal electrostatic repulsion [Aulich 2010]. In this study, PAA has been incubated in solution with the AuNRs at pH 7.0, obtaining a complete surface coverage. This is demonstrated by the inversion of the ζ-potential value (**Table 3.3**) from the initial positive charge of the AuNRs (+36.4 mV) to the negative charge of AuNRs@PAA (-37.9 mV).

Table 3.3: particle size (*d*), size distribution and surface charge of AuNRs.

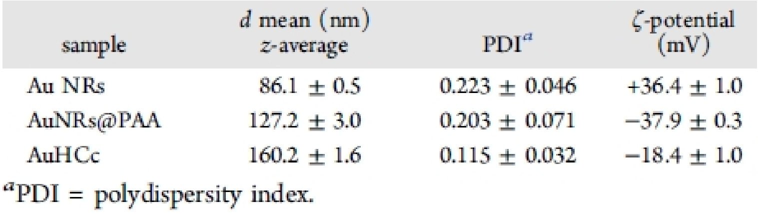

sample	*d* mean (nm) *z*-average	PDI^a	ζ-potential (mV)
Au NRs	86.1 ± 0.5	0.223 ± 0.046	+36.4 ± 1.0
AuNRs@PAA	127.2 ± 3.0	0.203 ± 0.071	−37.9 ± 0.3
AuHCc	160.2 ± 1.6	0.115 ± 0.032	−18.4 ± 1.0

^{a}PDI = polydispersity index.

As can be seen in the absorption spectrum of the AuNRs@PAA sample, after the purification procedure, the coverage with the PAA layer does not induce any significant change in the position of the longitudinal plasmon band (**Fig. 3.19**, red). At this stage, the AuNRs@PAA solution has been incubated with an excess of positively charged HHCc for 1 h to promote electrostatic anchoring of the protein on the AuNRs (AuHHCc sample). The unbound HHCc has been removed by centrifugation cycles, to precipitate and isolate only functionalized AuNRs. The experimental conditions are decisive not only to control the amount of protein anchored on the AuNRs surface by simply varying the incubation time of the protein in the AuNRs@PAA solution, but also to modulate the strength of the interaction, that may affect the extent of protein denaturation at the NRs surface [Aubin-Tam 2005, Verma 2005]. It has been reported that a higher protein coverage could result in an overcrowded arrangement and thus enhance the protein-protein and protein-NRs interactions, consequently affecting protein folding [Vertegel 2004, Aubin-Tam 2008]. Therefore, to maintain constant the number of free carboxylates of PAA coating the AuNRs, the AuNRs@PAA solution has been washed and redispersed in phosphate buffer solution at physiological pH (7.0). The presence of HHCc in the AuNRs solution is clearly shown by the absorption spectrum of the AuHHCc sample. The appearance of the Soret band of native HHCc (Fe^{3+}) at 409 nm, concomitant with the slight red shift of the longitudinal plasmon band due to the modification of the chemical environment, is clearly evident (**Fig. 3.19**, green). Remarkably, because of its low molecular weight, the free HHCc in solution does not precipitate along with the bioconjugated AuNRs upon numerous washing cycles of the sample by centrifugation. In fact, no precipitate is observed when pure HHCc solution was centrifuged in the same experimental conditions as the bioconjugated sample. The shoulder on the longitudinal plasmon band observed at higher wavelengths can be ascribed to minor aggregation phenomena arising from the purification/centrifugation cycles. The ζ-potential value after incubation with HHCc (**Table 3.3**) decreases because of the reduction in the number of free PAA carboxyl groups, which confirms that the protein is well-anchored and also indicates a good stability of the prepared NRs. Transmission electron microscopy (TEM) images of as-synthesized AuNRs (a), AuNRs coordinated by PAA (b), and AuHHCc are reported in **Fig. 3.20**. The TEM micrograph in (a) shows that the shape and size distribution of the AuNRs is quite uniform with an aspect ratio of 4.2 ± 0.4 (g). The TEM analysis of the aspect ratios of the particles for AuNRs@PAA and AuHHCc (h,i), performed on the TEM images (b,c), shows that they are 4.2 ± 0.5 and 4.1 ± 0.5, respectively. This confirms that the AuNRs preserve their size and shape after the polyelectrolyte wrapping and HHCc binding steps. Therefore, the slight modification of the longitudinal plasmon band position observed in **Fig. 3.19** can be safely ascribed to the modification of the chemical environment of AuNRs.

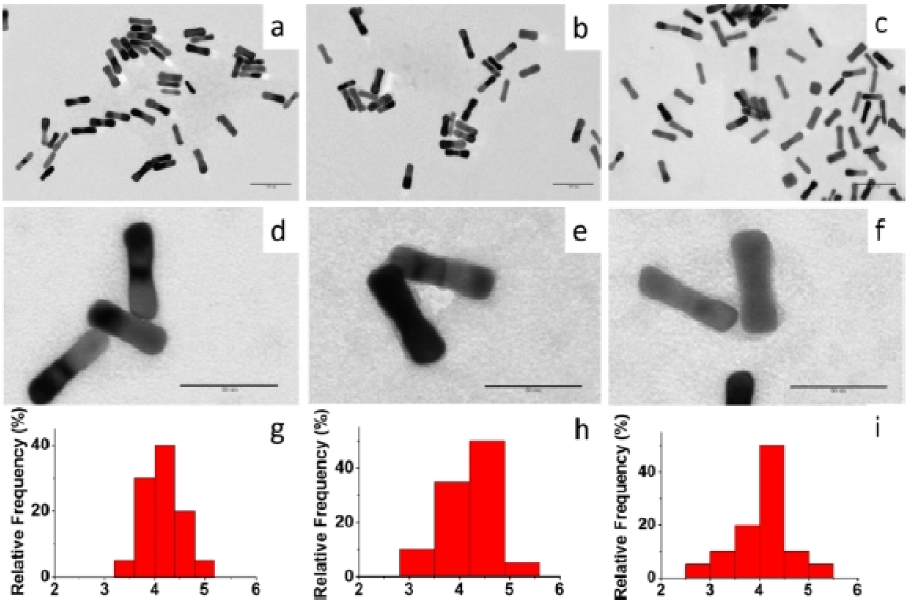

Figure 3.20: TEM images of AuNRs (a), AuNRs coordinated by PAA (b) and AuHHCc (c) (100 nm scale bar). The TEM images of the same samples captured in negative staining mode are shown in (d-f). (50 nm scale bar). The corresponding aspect ratio statistical analyses of the particles are presented in (g-i).

Interestingly, TEM images of the negatively stained samples (d-f) highlight the modification of the AuNRs organic coating, that passes from a uniform and thin layer for AuNRs to an inhomogeneous coating of about 2.5 nm for AuNRs@PAA, consistent with the less compact structure of a polyelectrolyte layer. Such features are even more evident when the HHCc is anchored to the AuNRs. Furthermore, the diameter analysis by dynamic light scattering (DLS) (**Table 3.3**) shows that the AuNRs are characterized by an equivalent spherical shape and rather homogeneous in size: 86.1 ± 0.5 nm for AuNRs, 127.2 ± 3.0 nm for AuNRs@PAA, and 160.2 ± 1.6 nm for AuHHCc, whereas their diameters are higher than those observed by TEM. This discrepancy can be explained by taking into account that DLS probes the hydrodynamic diameter, which includes the hydration shell due to the PAA coating. In addition, the DLS analysis of anisotropic particles, such as AuNRs, has to be interpreted cautiously because of the possible occurrence of multiple diffusion modes and must be considered only qualitatively.

The bioconjugation process has also been monitored by FTIR investigation (**Fig. 3.21**). The intense signal at 1702 cm^{-1} and the broad band with medium intensity at 1248 cm^{-1} are typically associated with ν(C=O) and ν(C-O) stretching modes of carboxylic group dimers. The weak bending δ(O-H) mode at 814 cm^{-1} further confirms the presence of carboxylic group dimers in PAA. In addition, the asymmetric stretching ν(C-O) mode, associated with -COO$^-$ at 1558 cm^{-1}, is coupled with the weaker symmetric ν(C-O) mode at 1408 cm^{-1}, indicating the presence of carboxylate ions [Hu 2002]. Therefore, this suggests that at the pH 7.0, the carboxylic groups of the PAA stock solution are not completely deprotonated and thus both dimers and carboxylate ions coexist. Remarkably, when PAA interacts with CTAB to wrap the AuNRs, the intense band at 1702 cm^{-1} significantly decreases, leaving the intense band at 1558 cm^{-1} of the carboxylate ions, which interacts with the ammonium heads of CTAB (**Fig. 3.21**, B). The binding of HHCc to the PAA layer results in the appearance of the typical band at 1652 cm^{-1} (**Fig. 3.21**, D), assigned to the ν(C=O) stretching mode of amide I of the protein (**Fig. 3.21**, C) that is a very sensitive probe of protein linkages [Jiang 2005]. In fact, the intensity of this signal slightly decreases when HHCc electrostatically interacts with PAA. Therefore, the overlap of the HHCc and PAA bands in the 1500-1700 cm^{-1} region does not permit any further considerations on the bioconjugation event. However, any denaturation of the protein can be ruled out, as indicated by the lack of a band at 1635 cm^{-1} in the FTIR spectrum of AuHHCc, typically ascribed to denatured HHCc (**Fig. 3.21**, D) [Speare 2003].

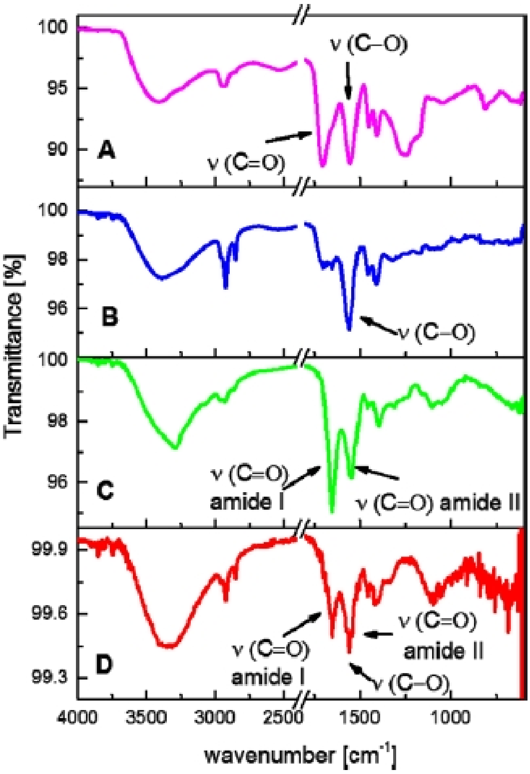

Figure 3.21: ATR-FTIR spectra of PAA (A), AuNRs@PAA (B), HHCc (C), and AuHHCc (D).

3.4.1 Raman measurements

To verify the native heme pocket structure retention of HHCc on the NPs surface, Raman measurements were performed on the bioconjugate. The AuHHCc RR spectra (**Fig. 3.22**, red) show, for both 406.7 (b) and 514.5 (a) nm excitation, the coexistence of the oxidized and reduced HHCc forms. For 406.7 nm excitation, in resonance with the HHCc Soret bands of both the ferric (409 nm) and ferrous (417 nm) forms, the spectra are dominated by the totally symmetric modes of native HHCc. In fact, for the Fe^{2+} form, ν_4, ν_3, ν_2, and ν_{10} bands are observed at 1363, 1492, 1592, and 1622 cm^{-1}, and for the Fe^{3+} form, ν_4, ν_3, ν_2, and ν_{10} bands are observed at 1372, 1502, 1585, and 1637 cm^{-1}, respectively. The full assignment is reported in **Table 3.4**.

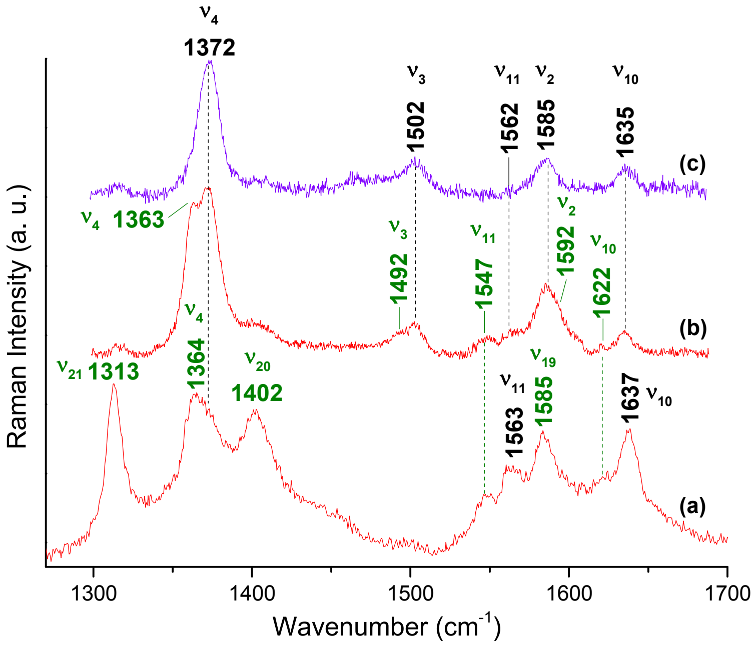

Figure 3.22: RR spectra of AuHHCc (red) and AuHHCc after addition of $K_3[Fe(CN)_6]$ (violet) obtained with the 514.5 (a) and 406.7 (b,c) nm excitation wavelengths. The bands assigned to (Fe^{2+}) and (Fe^{3+}) HHCc are indicated in green and black, respectively. Experimental conditions: laser power at the sample 40 (a) and 10 mW (b,c); average of 15 spectra with 2 h 30 min integration time (a), 4 spectra with 40 min integration time (b), and 8 spectra with 80 min integration time (c).

Table 3.4: Resonance Raman frequencies and vibrational assignments of Cyt c and AuHHCc [Hu 1993]. The bands assigned to Fe^{2+} and Fe^{3+} HHCc are indicated in green and black, respectively.

Mode	***Symmetry***	***λ_{exc} = 406.7 nm***			***λ_{exc} = 514.5 nm***		
		Cyt c		**AuHHCc**	**Cyt c**		**AuHHCc**
		Fe^{2+}	***Fe^{3+}***		***Fe^{2+}***	***Fe^{3+}***	
ν_8	***A_{1g}***	346	348	348			
ν_{50}	***E_u***	357	360	359			
$\delta(C_\beta C_c C_d)$		372 380	374 382	374 382			
$\delta(C_\beta C_a S)$		391 400	398	398			
$\delta(C_\beta C_a C_b)$		413 420	413 418	413 418			
γ_{22}	***E_g***	445	446	446			

ν_{33}	B_{2g}	478	480	480			
γ_{12}	B_{1u}	520	522	522			
γ_{21}	E_{g}	551 568	554 568	554 568			
ν(C-S)		683 691	693	683 692			
ν_{7}	A_{1g}	700	702	702			
ν_{15}	B_{1g}	750		750			
ν_{22}	A_{2g}				1130	1125	1130
ν_{30}	B_{2g}				1173	1169	1173
ν_{13}	B_{1g}				1230	1234	1230
ν_{42}	E_{u}				1242	1247	1247
ν_{21}	A_{2g}				1313	1316	1313
ν_{4}	A_{1g}	1361	1375	1372	1363	1372	1364 1372
ν_{20}	A_{2g}				1400	1409	1402
ν_{3}	A_{1g}	1492	1504	1492 1502	1492	1502	
ν_{11}	B_{1g}	1546	1564	1566	1547	1561	1547 1562
ν_{19}	A_{2g}	1584		1585	1583	1583	1585
ν_{2}	A_{1g}	1592	1584				
ν_{37}	E_{u}	1604	1596	1604			
ν_{10}	B_{1g}	1622	1635	1622 1635	1621	1635	1622 1637

Complete HHCc oxidation has been achieved by adding a minimum amount of $K_3[Fe(CN)_6]$ solution to the AuHHCc solution (**Fig. 3.22**, violet), without any change in the position of the Au plasmon bands and the HHCc Soret band (data not shown). This suggests that the reduced species represents only a small amount of the total HHCc bound to the NRs, even though it is clearly visible in the Raman spectrum. This apparent discrepancy probably results from different resonance intensification factors and cross sections of the core-size marker bands of the reduced form compared with the oxidized species. Moreover, the treatment with $K_3[Fe(CN)_6]$ did not induce any detachment of the protein from the NRs, as verified by subsequent centrifugation and washing of the sample (**Fig. 3.23**). Nevertheless, after the washing, the reduced species appears again in the Raman spectrum.

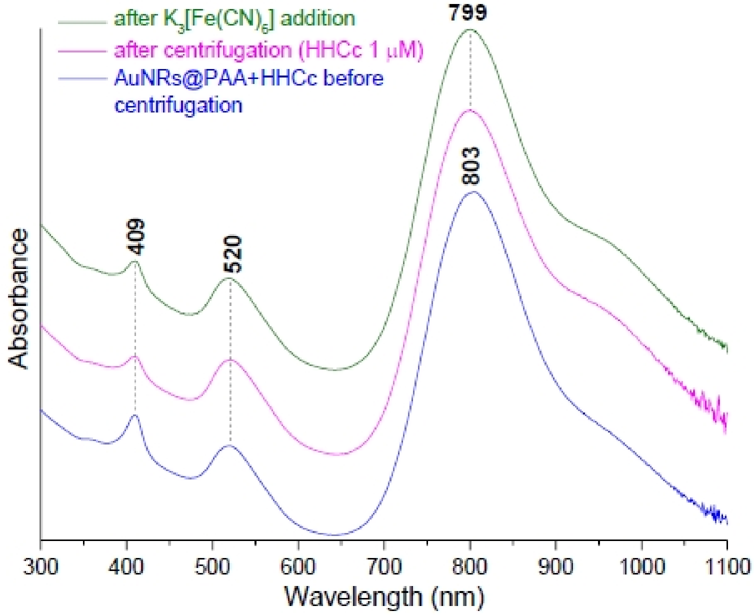

Figure 3.23: AuNRs@PAA + HHCc before washing (blue), after washing by centrifugation (pink) and after $K_3[Fe(CN)_6]$ addition (green).

Upon 514.5 nm excitation (**Fig. 3.22**, a), in resonance with the Q band transitions of HHCc (β-band at 530 and 520 nm for the ferric and ferrous forms, respectively), the spectrum is dominated, as expected, by B_{1g}, A_{2g}, and B_{2g} modes. The bands at 1313, 1402, and 1585 cm^{-1} are assigned to ν_{21}, ν_{20}, and ν_{19} of the ferrous form, respectively. However, the coexistence of the reduced and oxidized forms causes some changes in the relative intensity ratios of the bands compared with the spectra of the pure species (**Table 3.4**) [Hildebrandt 1986, Hu 1993]. The HHCc adsorbed on the NRs retains its native conformation (i.e., the heme iron is bound to the His18 and Met80 internal ligands), as demonstrated by the close correspondence of the difference spectra obtained by subtracting alternatively the native HHCc (Fe^{2+}) (**Fig. 3.24**, b-c) and the native HHCc (Fe^{3+}) (**Fig. 3.24**, b-a) from the spectrum of AuHHCc (**Fig. 3.24**, b). In fact, the core-size marker band frequencies are identical to those of the native protein in solution, indicating that no changes in the heme distortion, and hence ligation [Shelnutt 1998, Jentzen 1998], have been induced by bioconjugation.

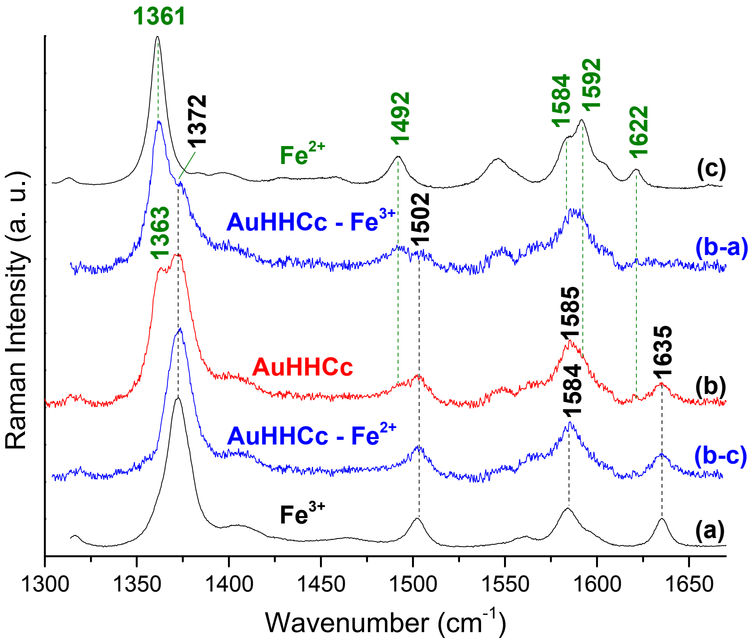

Figure 3.24: RR spectrum of AuHHCc (b) together with the difference spectra (b-c, b-a) after subtraction of the pure ferric HHCc (a) and ferrous HHCc (c) solution spectra. Experimental conditions: (a) 406.7 nm excitation wavelength, laser power at the sample 5 mW, average of 5 spectra with 25 min integration time; (b) 406.7 nm excitation wavelength, laser power at the sample 10 mW, average of 48 spectra with 4 h integration time; (c) 413.1 nm excitation wavelength, laser power at the sample 5 mW, average of 4 spectra with 20 min integration time.

This conclusion is confirmed by the “fingerprint” region between 300 and 450 cm^{-1} that shows the typical features of a Met-Fe-His species (**Fig. 3.25**), whereas none of the markers identified for the Cc misligated species (see paragraph 3.3) [Döpner 1998, Tognaccini 2016] are observed. Moreover, previous reports found that upon denaturation the disruption of the Met80-iron bond occurs concomitantly with the loss of the secondary structure and the increase in the molecular size under equilibrium unfolding conditions [Yeh 1998]. Because the band frequencies and the intensity pattern of AuHHCc (Figure 6b, red) are identical to those of the oxidized protein in solution (Figure 6a), with some minor changes due to the presence of a small percentage of the reduced species (Figure 6b), the HHCc structure and heme ligation are fully conserved on the AuNR surface.

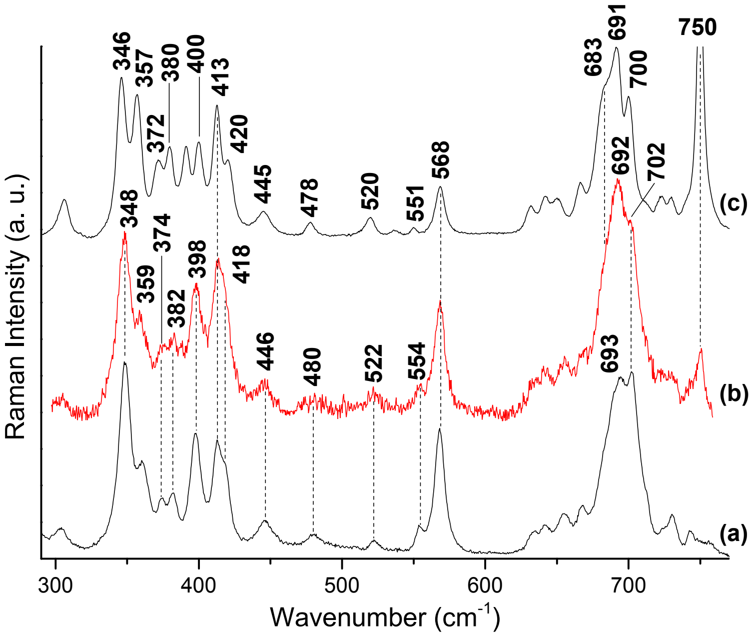

Figure 3.25: RR spectra of AuHHCc (b, red) compared with ferric (a) and ferrous (c) HHCc in the low-frequency region, obtained with the 406.7 nm excitation wavelength. Experimental conditions: laser power at the sample 5 mW (a,c) and 10 mW (b); average of 5 spectra with 25 min integration time (a), 18 spectra with 3 h integration time (b), and 4 spectra with 20 min integration time (c).

No SE(R)RS effect has been observed for both 406.7 and 514.5 nm excitation because the intensity of the HHCc signals is the same (or marginally lower) as that of a pure HHCc buffer solution at 10^{-6} M (**Fig. 3.26**), that is, the calculated HHCc concentration from the spectrum in Figure 1 (green line). Excitation with the 632.8, 647.1, 785, and 1064 nm laser lines has been also checked. However, no HHCc signals have been observed (data not shown).

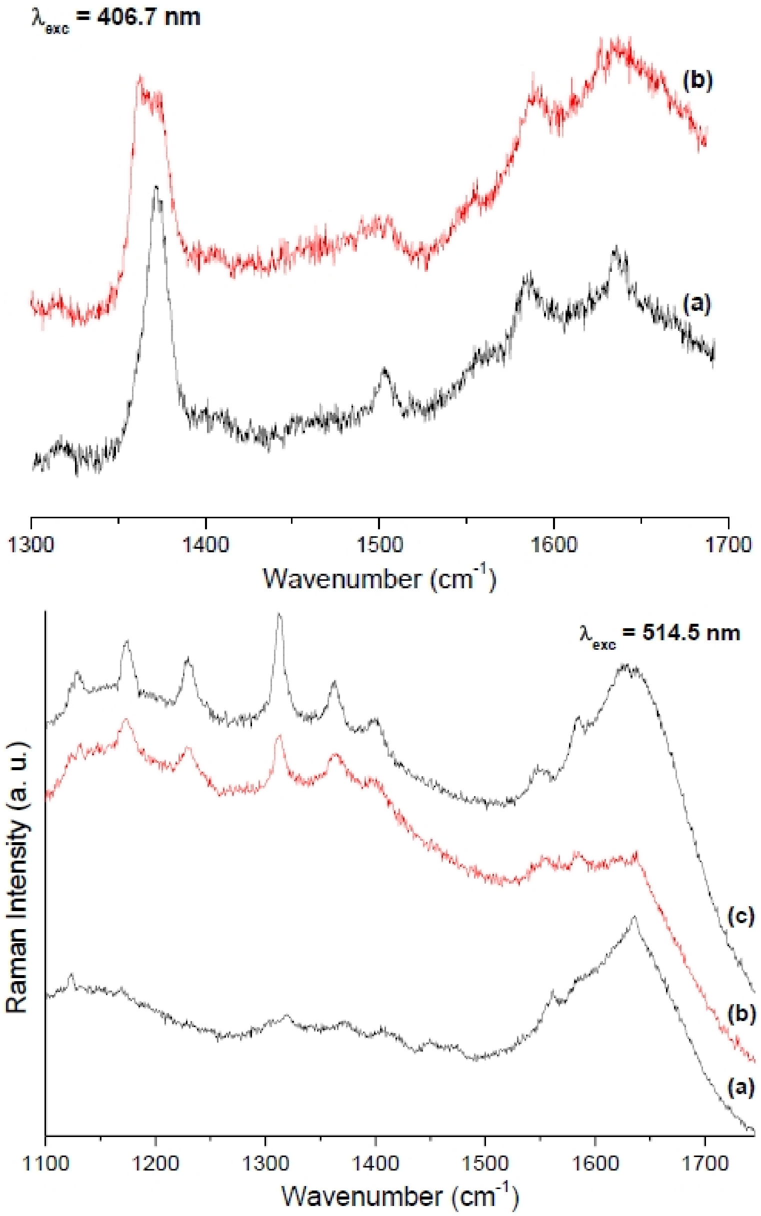

Figure 3.26: Top: RR spectra (406.7 nm) of AuHHCc (red) and HHCc (Fe^{3+}) solution (black). Experimental conditions: 406.7 nm excitation wavelength, laser power at the sample 10 mW, 5 min integration time. Bottom: RR spectra (514.5 nm) of AuHHCc (red) and HHCc Fe^{2+} (a) and Fe^{3+} (c) solutions (black). Experimental conditions: 514.5 nm excitation wavelength, laser power at the sample 40 mW, 10 min integration time. The HHCc solutions are at the same concentration calculated from the electronic absorption spectra of AuHHCc (1 μM, see **Fig. 3.19**, green).

3.4.2 Conclusions

In conclusion, the native state of the protein has been demonstrated for the first time, by means of Raman spectroscopy, to be retained upon conjugation with the anisotropic Au nanostructures, thus validating the proposed protocol as specifically suited to mostly preserve the plasmonic properties of the NRs and to retain the native heme Fe coordination of the protein.

The successful creation of such bioconjugates with the retention of the protein structure and function along with the preservation of the NPs properties represents a challenging but essential task, as it provides the only way to access functional hybrid systems with potential applications in biotechnology, medicine, and catalysis.

3.5 Cytochrome c - cardiolipin interaction on gold nanorods

Cc-cardiolipin (CL) interaction is a pivotal step in apoptosis initiation [Kagan 2005] and has been studied with many different techniques and in various experimental conditions [Kagan 2009, McMillin 2002, Bayir 2006, Kapralov 2007, Ow 2008, Muenzner 2014, Hannibal 2016]. Recently, the combination of UV-Vis, RR and EPR spectroscopies and site-directed mutagenesis allowed the long-standing debate about the nature of the structural changes induced by CL in the pre-apoptotic process to be resolved.[Capdevila 2015, Milazzo 2017] In fact, when interacting with CL, the 695 nm CT band decrease, indicating the rupture of the Fe-Met80 bond, while the Soret band blue-shifts at 407 nm and the RR core-size marker bands upshift; this demonstrates that a new misligated 6cLS species is formed, and the new distal ligand has been identified as a His, thanks to the comparison of the low frequency Cc-CL complex spectrum with that of the bis-His model compound [Milazzo 2017]. Hence, I tried to study Cc-CL interaction by bioconjugation of the Cc-CL complex on AuNRs@PAA.

1. The AuNRs@PAA were prepared as described above and then a solution of Cc-CL complex (molar ratio 1:30), prepared following a previously reported procedure [Kapetanaki 2009, Milazzo 2017], was added. The UV-Vis absorption spectrum after an hour of gentle stirring showed that the Cc Soret band blue-shifted from 409 to 408 nm, as

reported for the formation of the Cc-CL complex, indicating that at least a part of Cc bound CL and acquired bis-His coordination; anyway, the shift reverted completely after centrifugation and washing, implying that the newly formed Cc-CL complex was not adsorbed on the NRs surface and was washed away.

2. I tried to form the Cc-CL complex directly on the NRs surface by Cc titration with a CL solution: the AuHHCc bioconjugate was prepared following the usual procedure, then an aliquot of CL solution was added and the Soret band shifted to 408 nm (**Fig 3.27**, red). After centrifugation, the supernatant UV-Vis absorption spectrum (blue) shows that the newly formed Cc-CL complex detached from the NRs surface, whereas the uncomplexed Cc stayed on the NPs (pink).

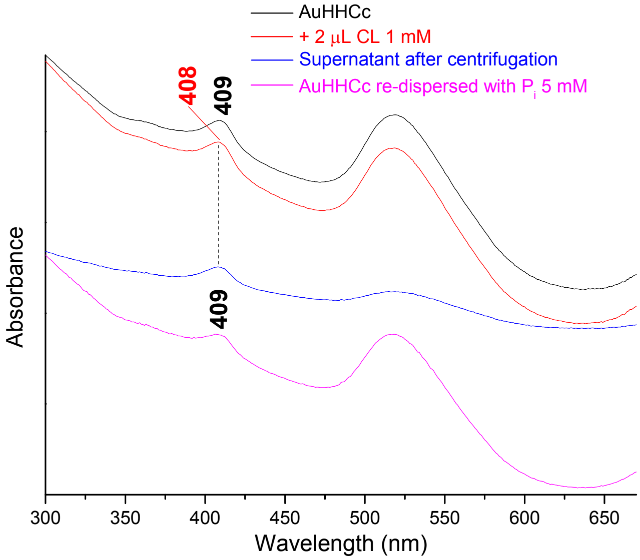

Figure 3.27: UV-Vis absorption spectra of AuHHCc (black), AuHHCc after CL addition (red), supernatant collected after centrifugation (blue), precipitate re-dispersed with 5 mM phosphate buffer (pink).

I repeated the procedure three more times, until the Soret absorbance in the centrifuged sample decreased to zero (**Fig 3.28**, left). Moreover, the spectra obtained from the supernatant after each centrifugation (**Fig 3.28**, right) demonstrate that, after every addition of CL, a consistent fraction of bioconjugated Cc is detached from the AuNRs@PAA and bind CL to form the Cc-CL complex. Therefore, the bioconjugation of the Cc-CL complex on AuNRs cannot be achieved because

AuNRs@PAA and CL compete for the same sites on Cc, most likely the positively charged Lys residues. In fact, CL bears negatively charged phosphate groups, thus displacing the protein from the NRs surface.

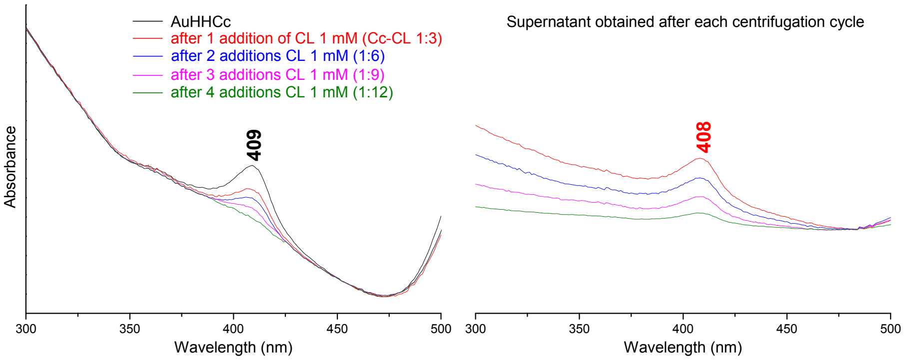

Figure 3.28: Left: UV-Vis absorption spectra of AuHHCc as prepared (black) and after each CL addition, centrifugation and re-dispersion with phosphate buffer (red, blue, pink, green). Right: UV-Vis absorption spectra of the corresponding supernatant solutions taken after every centrifugation.

References

- Alkilany A.M., Thompson L.B., Boulos S.P., Sisco P. N., Murphy C. J., Adv. Drug Delivery Rev. 2012, 64, 190-199.
- Aubin-Tam M.-E., Hamad-Schifferli K., Langmuir 2005, 21, 12080−12084.
- Aubin-Tam M.-E., Zhou H., Hamad-Schifferli K., Soft Matter 2008, 4, 554−559.
- Aubin-Tam M.-E., Hamad-Schifferli K., Biomed. Mater. 2008, 3, 034001.
- Aubin-Tam M.-E., Hwang W., Hamad-Schifferli K., Proc. Natl. Acad. Sci. U.S.A. 2009, 106, 4095−4100.
- Aulich D., Hoy O., Luzinov I., Brücher M., Hergenröder R., Bittrich E., Eichhorn K.-J., Uhlmann P., Stamm M., Esser N., Hinrichs K., Langmuir 2010, 26, 12926−12932.
- Austin L.A., Mackey M.A., Dreaden E.C., El-Sayed M.A., Arch. Toxicol. 2014, 88, 1391−1417.
- Battistuzzi G., Bortolotti C.A., Bellei M., Di Rocco G., Salewski J., Hildebrandt P., Sola M., Biochemistry 2012, 51, 5967.
- Bayir H., Fadeel B., Palladino M.J., Witasp E., Kurnikov I.V., Tyurina Y.Y., Tyurin V.A., Amoscato A.A., Jiang J., Kochanek P.M., Dekosky S.T., Greenberger J.S., Shvedova A.A., Kagan V.E., Biochim. Biophys. Acta 2006, 1757, 648.
- Bren K.L., Gray H.B., J. Am. Chem. Soc. 1993, 115, 10382–10383.
- Brown K.R., Fox A.P., Natan M.J., J. Am. Chem. Soc. 1996, 118, 1154−1157.
- Burda C., Chen X., Narayanan R., El-Sayed M. A., Chem. Rev. 2005, 105, 1025−1102.
- Burke S.E., Barrett C.J., Pure Appl. Chem. 2004, 76, 1387−1398.
- Capdevila D.A., Oviedo Rouco S., Tomasina F., Tortora V., Demicheli V., Radi R., Murgida D.H., Biochemistry 2015, 54, 7491.
- Caroppi P., Sinibaldi F., Fiorucci L., Santucci R., Curr. Med. Chem. 2009, 16, 4058–4065.
- Casalini S., Battistuzzi G., Borsari M., Bortolotti C.A., Di Rocco G., Ranieri A., Sola M., J. Phys. Chem. B 2010, 114, 1698–1706.

- Choi S., Spiro T.G., Langry K.C., Smith K.M., J. Am. Chem. Soc. 1982, 104, 4337–4344.
- Daniel M.-C., Astruc D., Chem. Rev. 2004, 104, 293−346.
- Döpner S., Hildebrandt P., Rosell F.I., Mauk A.G., J. Am. Chem. Soc. 1998, 120, 11246.
- Hainfeld J.F., Powell R.D., J. Histochem. Cytochem. 2000, 48, 471−480.
- Hamad-Schifferli K., Schwartz J.J., Santos A.T., Zhang S., Jacobson, J.M., Nature 2002, 415, 152−155.
- Hannibal L., Tomasina F., Capdevila D.A., Demicheli V., Tortora V., Alvarez‐Paggi D., Jemmerson R., Murgida D.H., Radi R., Biochemistry 2016, 55, 407.
- Hildebrandt P., Stockburger M., J. Phys. Chem. 1986, 90, 6017−6024.
- Hildebrandt P., Biochim. Biophys. Acta 1990, 1040, 175.
- Hobara D., Niki K., Zhou C., Chumanov G., Cotton T.M., Colloids Surf. A 1994, 93, 241−250.
- Hu S., Morris I.K., Singh J.P., Smith K.M., Spiro T.G., J. Am. Chem. Soc. 1993, 115, 12446−12458.
- Hu Y., Jiang X., Ding Y., Ge H., Yuan Y., Yang C., Biomaterials 2002, 23, 3193−3201.
- Huang X., Neretina S., El-Sayed M.A., Adv. Mater. 2009, 21, 4880−4910.
- Indiani C., De Sanctis G., Neri F., Santos H., Smulevich G., Coletta M., Biochemistry 2000, 39, 8234.
- Jain P.K., Huang X., El-Sayed I.H., El-Sayed M.A., Acc. Chem. Res. 2008, 41, 1578−1586.
- Jentzen W., Ma J.-G., Shelnutt J.A., Biophys. J. 1998, 74, 753−763.
- Jiang X., Jiang J., Jin Y., Wang E., Dong S., Biomacromolecules 2005, 6, 46−53.
- Jordan T., Eads J.C., Spiro T.G., Protein Sci. 1995, 4, 716.
- Kagan V.E., Tyurin V.A., Jiang J., Tyurina Y.Y., Ritov V.B., Amoscato A.A., Osipov A.N., Belikova N.A., Kapralov A.A., Kini V., Vlasova I., Zhao Q., Zou M., Di P., Svistunenko D.A., Kurnikov I.V., Borisenko G.G., Nat. Chem. Biol. 2005, 1, 223.

- Kagan V.E., Bayir H.A., Belikova N.A., Kapralov O., Tyurina Y.Y., Tyurin V.A., Jiang J., Stoyanovsky D.A., Wipf P., Kochanek P.M., Greenberger J.S., Pitt B., Shvedova A.A., Borisenko G., Free Radical Biol. Med. 2009, 46, 1439.
- Kapetanaki S.M., Silkstone G., Husu I., Liebl U., Wilson M.T., Vos M.H., Biochemistry 2009, 48, 1613−1619.
- Kapralov A.A., Kurnikov I.V., Vlasova I.I., Belikova N.A., Tyurin V.A., Basova L.V., Zhao Q., Tyurina Y.Y., Jiang J., Bayir H., Biochemistry 2007, 46, 14232.
- Katz E., Willner I., Angew. Chem., Int. Ed. 2004, 43, 6042−6108.
- Keating C.D., Kovaleski K.M., Natan M.J., J. Phys. Chem. B 1998, 102, 9404−9413.
- Khanal B.P., Zubarev E.R., Angew. Chem., Int. Ed. 2007, 46, 2195−2198.
- Kitagawa T., The heme protein structure and the iron histidine stretching mode. In Biological applications of Raman spectroscopy: Resonance Raman spectra of hemes and metalloproteins (Spiro, T. G., Ed.) 1988, vol. 3, pp 97−131, John Wiley and Sons Inc., New York.
- Królikowska A., Bukowska J., J. Raman Spectrosc. 2007, 38, 943−949.
- Kuo W.-S., Chang C.-N., Chang Y.-T., Yang M.-H., Chien Y.-H., Chen S.-J., Yeh C.-S., Angew. Chem., Int. Ed. 2010, 49, 2711−2715.
- Lee K.-S., El-Sayed M. A., J. Phys. Chem. B 2006, 110, 19220−19225.
- Link S., Mohamed M.B., El-Sayed M.A., J. Phys. Chem. B 1999, 103, 3073−3077.
- Lofas S., Pure Appl. Chem. 1995, 67, 829−834.
- Malikova N., Pastoriza-Santos I., Schierhorn M., Kotov N.A., Liz-Marzán L.M., Langmuir 2002, 18, 3694−3697.
- Margoliash E., Frohwirt N., Biochem. J. 1959, 71, 570–572.
- Mason J.N., Farmer H., Tomlinson I.D., Schwartz J.W., Savchenko V., DeFelice L.J., Rosenthal S.J., Blakely R.D., J. Neurosci. Methods 2005, 143, 3−25.

- McMillin J.B., Dowhan W., Biochim. Biophys. Acta - Molecular and Cell Biology of Lipids 2002, 1585, 97.
- Milazzo L., Tognaccini L., Howes B.D., Sinibaldi F., Piro M.C., Fittipaldi M., Baratto M.C., Pogni R., Santucci R., Smulevich G., Biochemistry 2017, 56, 1887.
- Muenzner J., Pletneva E.V., Chem. Phys. Lipids 2014, 179, 57.
- Murphy C.J., Thompson L.B., Alkilany A.M., Sisco P.N., Boulos S.P., Sivapalan S.T., Yang J.A., Chernak D.J., Huang J., J. Phys. Chem. Lett. 2010, 1, 2867−2875.
- Njoki P. N., Lim I.-I.S., Mott D., Park H.-Y., Khan B., Mishra S., Sujakumar R., Luo J., Zhong C.-J., J. Phys. Chem. C 2007, 111, 14664−14669.
- Oellerich S., Wackerbarth H., Hildebrandt P., J. Phys. Chem. B 2002, 106, 6566.
- Orrenius S., Gogvadze V., Zhivotovsky B., Annu. Rev. Pharmacol. Toxicol. 2007, 47, 143.
- Othman S., Le Lirzin A., Desbois A., Biochemistry 1994, 33, 15437–15448.
- Othman S., Desbois A., Eur. Biophys. *J.* 1998, 28, 12–25.
- Ow Y.P., Green D.R., Hao Z., Mak T.W., Nat. Rev. Mol. Cell Biol. 2008, 9, 532.
- Park J., Yoon D.-Y., Kim Y., Korean J. Chem. Eng. 2009, 26, 258−260.
- Patriarca A., Polticelli F., Piro M.C., Sinibaldi F., Mei G., Bari M., Santucci R., Fiorucci L., Arch. Biochem. Biophys. 2012, 522, 62–69.
- Pérez-Juste J., Pastoriza-Santos I., Liz-Marzán L.M., Mulvaney P., Coord. Chem. Rev. 2005, 249, 1870−1901.
- Placido T., Fanizza E., Cosma P., Striccoli M., Curri M.L., Comparelli R., Agostiano A., Langmuir 2014, 30, 2608−2618.
- Ros I., Placido T., Amendola V., Marinzi C., Manfredi N., Comparelli R., Striccoli M., Agostiano A., Abbotto A., Pedron D., Pilot R., Bozio R., Plasmonics 2014, 9, 581−593.
- Sau T.K., Rogach A.L., Jäckel F., Klar T.A., Feldmann, J., Adv. Mater. 2010, 22, 1805−1825.

- Santoni E., Scatragli S., Sinibaldi F., Fiorucci L., Santucci R., Smulevich G., J. Inorg. Biochem. 2004, 98, 1067.
- Santucci R., Sinibaldi F., Patriarca A., Santucci D., Fiorucci L., Expert Rev. Proteomics 2010, 7, 507–517.
- Scott R.A., Mauk A.G., Cytochrome C: A Multidisciplinary Approach, Univ. Science Books, Sausalito, 1996.
- Shelnutt J.A., Song X.-Z., Ma J.G., Jia S.L., Jentzen W., Medforth C.-J., Chem. Soc. Rev.1998, 27, 31.
- Sinibaldi F., Piro M.C., Howes B.D., Smulevich G., Ascoli F., Santucci R., Biochemistry 2003, 42, 7604.
- Speare J.O., Rush T.S., Biopolymers 2003, 72, 193−204.
- Stellwagen E., Cass R., Biochem. Biophys. Res. Commun. 1974, 60, 371.
- Tognaccini L., Ciaccio C., D'oria V., Cervelli M., Howes B.D., Coletta M., Mariottini P., Smulevich G., Fiorucci L., J. Inorg. Biochem. 2016, 155, 56–66.
- Verma A., Rotello V.M., Chem. Commun. 2005, 303−312.
- Vertegel A.A., Siegel R.W., Dordick J.S., Langmuir 2004, 20, 6800−6807.
- Yang M., Chung F.L., Thompson M., Anal. Chem. 1993, 65, 3713−3716.
- Yeh S.-R., Rousseau D.L., Nat. Struct. Biol. 1998, 5, 222−228.
- Ying T., Wang Z.-H., Lin Y.-W., Xie J., Tan X., Huang Z.-X., Chem. Commun. 2009, 30, 4512–4514.
- Yu X., Lei D.Y., Amin F., Hartmann R., Acuna G.P., Guerrero-Martínez A., Maier S.A., Tinnefeld P., Carregal-Romero S., Parak W.J., Nano Today 2013, 8, 480−493.
- Weidinger I.M., Murgida D.H., Dong W.-F., Möhwald H., Hildebrandt P., J. Phys. Chem. B 2006, 110, 522−529.

Chapter 4

Silver nanowires as infrared-active materials for surface-enhanced Raman scattering

- Becucci M., Bracciali M., Ghini G., Lofrumento C., Pietraperzia G., Ricci M., Tognaccini L., Trigari S., Gellini C., Feis A., Silver nanowires as infrared-active materials for surface-enhanced Raman scattering, Nanoscale 2018, 10, 9329-9337.

4.1 Introduction

The great development of nanotechnology and novel nanofabrication methods [Betz 2014, Lane 2015, Fabris 2016, Mosier-Boss 2017, Amendola 2017, Zhang 2017] opened the doors to a broad range of applications for surface-enhanced Raman scattering (SERS) spectroscopy. SERS is commonly performed in the visible range, whereas infrared excitation is by far less usual in spite of its great potential in biological applications. Infrared radiation, in fact, can penetrate biological tissues to a much larger extent than visible light, especially between 700 and 900 nm (near-infrared I region), and between 1000 and 1400 nm (near-infrared II region) [Bashkatov 2005, Troy 2001, Altınoğlu 2010]. Therefore, developing new SERS-active materials in the NIR region is fundamental to explore new opportunities of SERS application. Presently, the choice is limited to aggregated metal nanospheres [Leopold 2003] or specially designed nanostructures [Greeneltch 2013, Kearns 2015], which can display a localized surface plasmon resonance (LSPR) band in the near infrared.

Silver nanowires (AgNWs) appear to be a natural choice because of their extremely broad LSPR extinction band, which covers the UV, visible, and infrared regions. They offer the additional advantage of a relatively high enhancement factor (EF), due to the optical properties of silver [Rycenga 2011]. Nevertheless, SERS spectroscopy with AgNWs has only been performed with excitation wavelengths shorter than 800 nm [Tao 2003, Hunyadi 2006, Goh 2012, Santos 2016, Chen 2017, Singh 2012].

In this work, the SERS activity of commercially available and water-dispersible AgNWs with 1064 nm excitation has been tested and then compared with the relative enhancement obtained by shorter-wavelength excitation.

4.2 Materials

Ethylene glycol, polyvinylpyrrolidone (PVP), and benzenethiol were purchased from Sigma-Aldrich, and glycerol and pyridine were purchased from Merck. All reagents were used without further purification. Isopropanol (from Merck) was distilled before use. High-purity $AgNO_3$ was produced by Cabro (Arezzo, Italy). Water solutions were prepared with deionized (Milli-Q) water.

4.2.1 Silver nanowires synthesis

AgNWs were obtained by Cabro according to a polyol synthesis method using PVP as a capping agent and NaCl as a catalyst [Sun 2010, Tao 2008, Wiley 2007]. 25 mL of 0.01 M NaCl and 35 g PVP were added to 500 mL of ethylene glycol at 60 °C under stirring to obtain a clear solution. 10 g $AgNO_3$ were diluted in 300 mL ethylene glycol in the dark with the help of an ultrasonic bath until a homogeneous pale yellow solution was obtained. This solution was poured into PVP at a $[NaCl]/[AgNO_3]$ ratio close to 0.07. The resulting solution became reddish. The temperature was kept at 80 °C for 20 min and then increased to 100 °C until the NO_x red gases completely evaporated and the solution became grey. AgNWs were precipitated with acetone and dried, then re-dispersed with isopropanol.

4.2.2 Silver nanowires purification

The as-synthesized material had to be further treated in order to remove residual PVP and to reduce the fraction of small-sized AgNPs. To this aim, AgNWs samples were purified by continuous density gradient centrifugation [Steinigeweg 2011]. Five glycerol/water solutions (30/70, 35/65, 40/60, 45/55 and 50/50 v/v) were prepared and 2 mL of each solution were stratified carefully in a 15 mL Falcon tube, starting with the 30/70 solution at the bottom. The tube was kept horizontally for about 15 minutes, and then centrifuged at 3000 rpm for 5 minutes. Right after, 200 μL of the AgNWs isopropanol dispersion were added on the top of the glycerol solution and centrifuged at 3000 rpm until a precipitate was formed at the very bottom of the tube. Most of the samples stayed as a brown layer at the top of the tube. The top and the bottom fractions were separated using a Pasteur pipette, and centrifuged for 10 minutes at 8000 rpm. The precipitates were re-suspended in water and this procedure was repeated twice for each fraction. The samples for SERS and LIOAS measurements were prepared by diluting the top fraction in deionized water. The concentration range was 0.02–0.8% (metal mass/volume).

4.2.3 Samples preparation

SERS spectra has been obtained at 406.7 and 514.5 nm excitations with a dispersive spectrometer and at 1064 nm excitation with a Bruker MultiRAM FT-Raman (see Chapter 2).

Samples for wavelength-dependent SERS measurements were prepared by adding a 10^{-2}, 10^{-3} or 10^{-4} M benzenethiol aqueous solution to AgNWs to reach a final 10^{-4}, 10^{-5} or 10^{-6} M benzenethiol concentration. Pure isopropanol was added to a final 5% (v/v) concentration as an internal intensity standard to evaluate the SERS intensity when the excitation wavelength is changed. The presence of an internal standard is required, as the absorption of the incident and scattered light by the sample strongly depends on the wavelength.

Concentration-dependent measurements at 514.5 nm excitation wavelength yielded an estimate for the limit of detection (LOD) of benzenethiol (10^{-6} M < LOD < 10^{-5} M) and pyridine (10^{-4} M < LOD < 5×10^{-4} M).

4.3 Silver nanowires characterization

SEM was used to study nanometer-scale features such as the morphology, length and diameter of the NWs. **Fig. 4.1** displays randomly piled up AgNWs, with lengths between 1 and 4 μm and an average thickness of 90 ± 10 nm. The cross section of the nanowires appears rather prismatic than circular. A minority fraction of smaller nanoparticles with very different shapes and sizes was also observed.

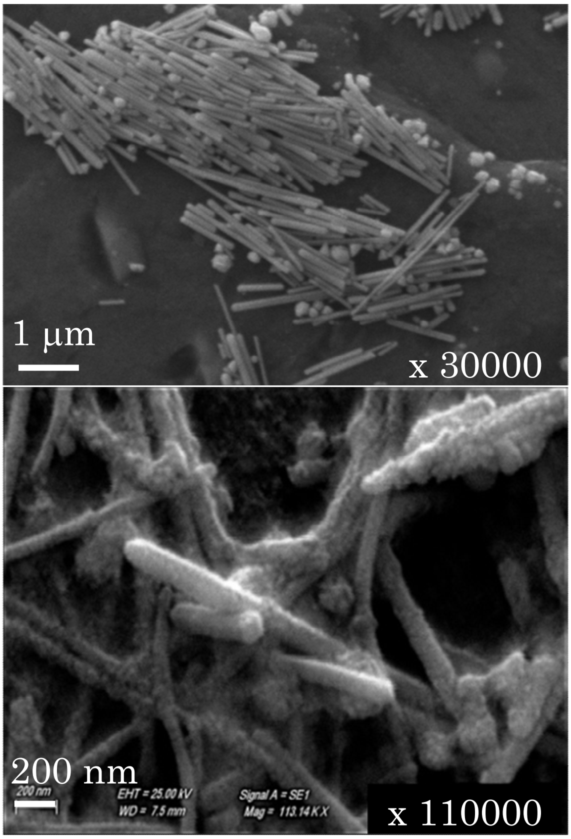

Figure 4.1: Representative SEM images of AgNWs at 30000× and 110000× magnification.

The extinction spectra of AgNWs are characterized by an extremely broad LSPR band, extending from the near UV to the infrared range [Johns 2017]. The as-synthesized material displayed a shoulder at 352 nm and a maximum at 386 nm, together with a shoulder at 411 nm (**Fig. 4.2**, A). After purification, the main component gave rise to a spectrum with a maximum at 387 nm without the 411 nm shoulder (**Fig. 4.2**, B), whereas the residual fraction yielded a spectrum with a prominent shoulder at 432 nm (**Fig. 4.2**, C). The latter fraction likely corresponds to the smaller nanoparticle population observed by SEM. These results were in line with those obtained by a previously described purification procedure [Gao 2005].

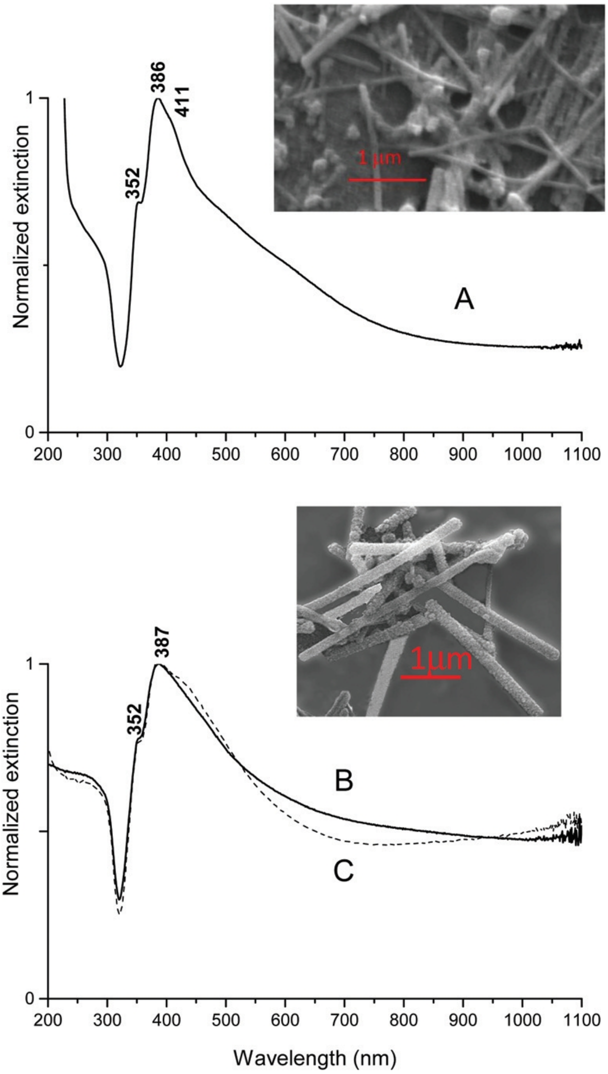

Figure 4.2: Extinction spectra of the AgNW aqueous dispersion before purification (A) and of the top (B, solid line) and bottom (C, dashed line) fractions (see Experimental methods). The three spectra have been normalized to unity. Representative SEM images of fractions A and B are shown.

In particular, the extinction spectrum of purified AgNWs was very similar to the previous one, which was interpreted as originating from AgNWs with a pentagonal cross section on the basis of electronic microscopy images and previous theoretical work [Kottmann 2001].

The shoulder at 352 nm can therefore be assigned to the transverse quadrupole resonance, the band at 387 nm to the transverse dipole resonance, and the broad, featureless band at longer wavelengths to the longitudinal resonance. The presence of an intense quadrupole band confirms that the cross section of our AgNWs is prismatic [Shuford 2005, Pietrobon 2009].

4.4 SERS measurements

The exceptionally large width of the LSPR band suggests that SERS spectra can be obtained from AgNWs with excitation wavelength (λ_{exc}) in a very broad range. To test this opportunity, I performed SERS with excitation at 407 nm, i.e., close to the extinction maximum, at 514.5 nm, on the red edge of the LSPR band, and at 1064 nm, where the extinction reaches a plateau. The experimental conditions were specifically adjusted to obtain a reliable comparison of the SERS intensities at different wavelengths. Benzenethiol was chosen as a SERS probe because it does not display electronic resonances in this wavelength range. AgNWs were used as aqueous dispersions where isopropanol was added as an internal intensity standard. Isopropanol was chosen because it does not interact with the metal surface, thus only its Raman bands are observed in the spectra.

At 514.5 nm and 1064 nm I tested three different benzenethiol concentrations, 10^{-4} M, 10^{-5} M, and 10^{-6} M (**Fig. 4.3**).

Then, the intensity ratio between the Raman bands of 10^{-4} M benzenethiol and those of isopropanol at different λ_{exc} was evaluated. This ratio yielded the wavelength dependence of the enhancement factor (EF), even if I did not perform a determination of the absolute EF, which had been previously shown to be 5.8×10^3 (at 514.5 nm) for similar AgNWs [Goh 2012].

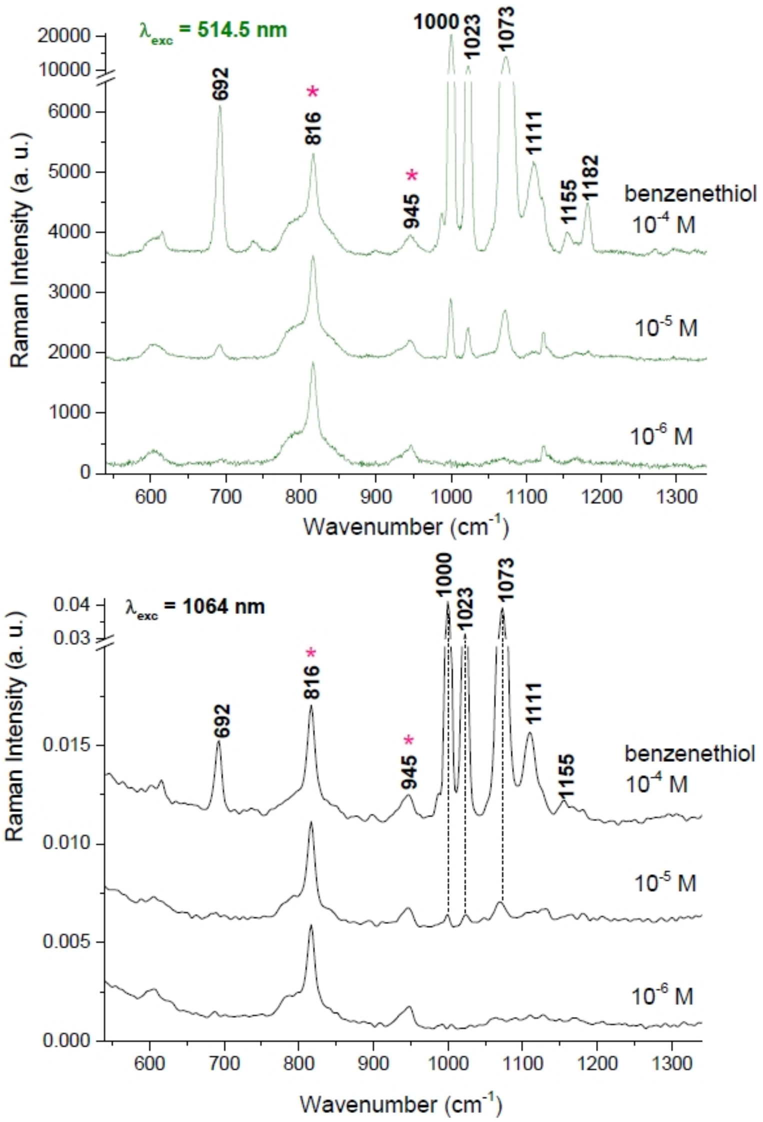

Figure 4.3: SERS spectra of benzenethiol on AgNWs as a function of concentration at $\lambda_{ex.}$= 514.5 and 1064 nm. The asterisks mark the bands of the internal standard isopropanol (5% v/v). Experimental conditions: (514.5 nm) 5 mW power at the sample, 10 minutes integration time; (1064 nm) 200 mW power at the sample, 400 scans averaged.

Fig. 4.4 shows the extinction spectrum of AgNWs after the addition of 10^{-4} M benzenethiol. The only effect of the analyte addition was a slight red shift of the LSPR band maximum.

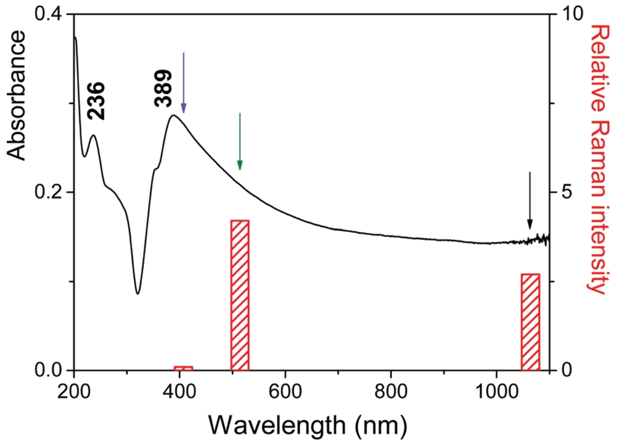

Figure 4.4: Extinction spectrum of the AgNWs aqueous dispersion after the addition of 10^{-4} M benzenethiol. The arrows indicate the three λ_{ex} for SERS spectra, and the red bars represent the intensity ratio between the benzenethiol SERS band at 1000 cm^{-1} and the isopropanol Raman band at 817 cm^{-1}.

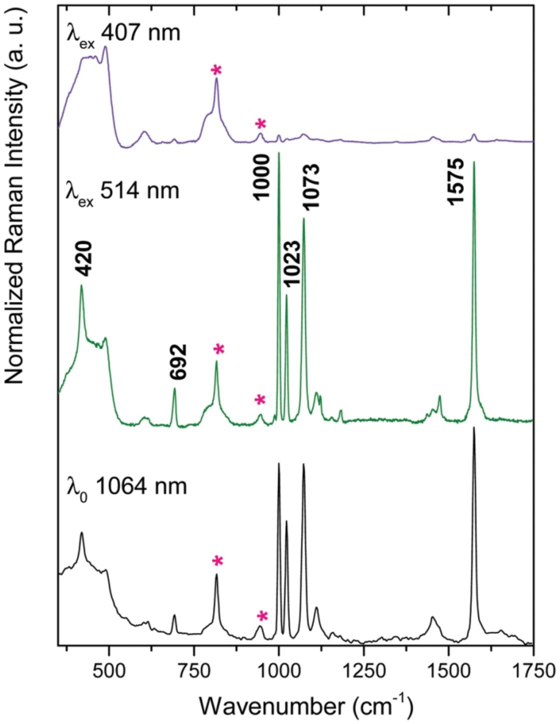

Figure 4.5: SERS spectra the AgNWs aqueous dispersion after the addition of 10^{-4} M benzenethiol at the three λ_{ex}. The asterisks label the bands of the internal standard isopropanol. Experimental conditions: (406.7 and 514.5 nm)

5 mW power at the sample, 10 minutes integration time; (1064 nm) 200 mW power at the sample, 400 scans averaged.

The SERS spectra of benzenethiol adsorbed on AgNWs at the three selected λ_{ex} (**Fig. 4.5**) matched the published SERS spectra of benzenethiol on Ag surfaces [Carron 1991]. In particular, the intensity of the strong band at 1000 cm^{-1}, which can be assigned to the ring breathing mode, was similar to the intensity of the bands at 1073 cm^{-1} and 1575 cm^{-1}. This feature is typical of benzenethiol adsorbed onto Ag surfaces [Zhou 2008], and contrasts with the spectrum of pure liquid benzenethiol, where the band at 1000 cm^{-1} is by far the strongest one.
The spectra were most intense for 514.5 nm excitation. At 1064 nm excitation, the relative intensity of the bands of benzenethiol was weaker. For example, the band at 1000 cm^{-1} was weakened by a factor of 1.5. The bands of benzenethiol could be hardly detected at 407 nm excitation (**Table 4.1**). The relative intensities at the three λ_{ex} values are plotted in **Fig. 4.4**.

Table 4.1: Relative intensities of the most intense benzenethiol bands in the SERS spectra shown in **Fig. 4.3**. I* represents the normalized intensity of the isopropanol band at 817 cm^{-1}.

	I*	I_{1000}	I_{1023}	I_{1073}
λ_{ex} = 407 nm	1.0	0.1	0.05	0.1
λ_{ex} = 514.5 nm	1.0	4.2	2.0	3.05
λ_{ex} = 1064 nm	1.0	2.7	1.85	2.6

The data in **Fig. 4.4** and **4.5** are a clear example of the non-coincidence of extinction and EF. In particular, the unusually high EF observed in the NIR region could be due to:

i) the presence of small amounts of extended NPs aggregates, displaying especially high EFs at long wavelengths;
ii) some analytes, like heterocyclic aromatic molecules, can form charge-transfer complexes with the metal surface (chemical effect) [Lombardi 2009], leading to the appearance of new electronic transitions, often lying at wavelengths longer than the LSPR band;
iii) the presence of diverse LSPRs, which can contribute to extinction and SERS EF to a strongly different extent [Reguera 2017, Giannini 2007]. Anisotropic NPs like nanorods [Guiton 2011, Chu

2009] and nanosphere dimers [Kleinman 2013, Le Ru 2006] are characterized by a relatively weak resonance at shorter wavelengths and a stronger one at longer wavelengths. The wavelength dependence of the electric field intensity at the metal surface that gives rise to SERS follows the shape of the extinction spectrum, but the EF is increased by several orders of magnitude for the longer wavelength resonance, whereas extinction changes to a much lesser extent. Therefore, SERS on anisotropic nanoparticles is most effective for λ_{ex} in the red/NIR region [Le Ru 2009].

Contribution of reasons (i) and (ii) to the SERS wavelength dependence cannot be excluded, but most likely the AgNWs marked anisotropy is determinant, i.e. the SERS enhancement at longer wavelengths originates from resonance with a longitudinal mode. Finite element method (FEM) simulations, performed by others, confirmed this possible explanation.

Moreover, laser induced optoacoustic spectroscopy (LIOAS) measurements (performed by others) showed that contributions to extinction are mostly due to scattering, especially in the NIR, where absorption is negligible (**Fig. 4.6**). This has important consequences in the field of AgNWs applications because it has been recently reported that highly absorbing SERS substrates display a rapid decrease of the SERS signal under laser irradiation, because of high temperatures around the nanoparticle surface. In contrast, AgNWs can indeed act as SERS substrates without heating and therefore may be advantageous when compared to other plasmonic systems.

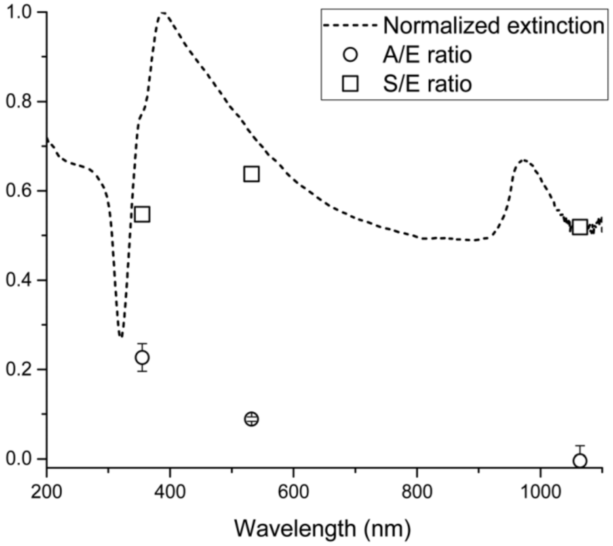

Figure 4.6: Absorbance/Extinction (A/E) and Scattering/Extinction (S/E) ratios obtained by LIOAS measurements. In this figure the water absorption band at ~980 nm has not been subtracted from the spectrum.

4.5 Conclusions

In conclusion, AgNWs demonstrated to be a very useful SERS substrate for NIR excitation, because not only in this region they are still fairly SERS-active, but also absorption does not significantly contribute to extinction, thus preventing the AgNWs from heating. The effect is outstanding at 1064 nm, nevertheless, low heating and high SERS efficiency are maintained at shorter wavelengths (514.5 nm), adding further versatility to AgNWs as SERS substrates.

References

- Altınoğlu E.İ., J.H. Adair, WIREs Nanomed. Nanobiotechnol. 2010, 2, 461.
- Amendola V., Pilot R., Frasconi M., Maragò O.M., Iatì M.A., J. Phys.: Condens. Matter 2017, 29, 203002.
- Bashkatov A.N., Genina E.A., Kochubey V.I., Tuchin V.V., J. Phys. D: Appl. Phys. 2005, 38, 2543.
- Betz J.F., Yu W.W., Cheng Y., White I.M., Rubloff G.W., Phys. Chem. Chem. Phys. 2014, 16, 2224.
- Carron K.T., Hurley L.G., J. Phys. Chem. 1991, 95, 9979.
- Chen Y.C., Hsu J.H., Lin Y.G., Hsu Y.K., Sens. Actuators B 2017, 245, 189.
- Chu M.-W., Myroshnychenko V., Hsuan Chen C., Deng J.-P., Mou C.-Y., García de Abajo F.J., Nano Lett. 2009, 9, 399.
- D’Andrea C., Irrera A., Fazio B., Foti A., Messina E., Maragò O.M., Kessentini S., Artoni P., David C., Gucciardi P.G., J. Opt. 2015, 17, 114016.
- Fabris L., Chem. Nano Mat. 2016, 2, 249.
- Gao Y., Jiang P., Song L., Liu L., Yan X., Zhou Z., Liu D., Wang J., Yuan H., Zhang Z., Zhao X., Dou X., Zhou W., Wang G., Xie S., J. Phys. D: Appl. Phys. 2005, 38, 1061.
- Giannini V., Sánchez-Gil J.A., J. Opt. Soc. Am. A 2007, 24, 2822–2830.
- Goh M.S., Lee Y.H., Pedireddy S., Phang I.Y., Tjiu W.W., Tan J.M.R., Ling X.Y., Langmuir 2012, 28, 14441.
- Greeneltch N.G., Blaber M.G., Schatz G.C., Van Duyne R.P., J. Phys. Chem. C 2013, 117, 2554.
- Guiton B.S., Iberi V., Li S., Leonard D.N., Parish C.M., Kotula P.G., Varela M.,. Schatz G.C, Pennycook S.J., Camden J.P., Nano Lett. 2011, 11, 3482.
- Hunyadi S.E., Murphy C.J., J. Mater. Chem. 2006, 16, 3929.
- Johns P., Beane G., Yu K., Hartland G.V., J. Phys. Chem. C 2017, 121, 5445.

- Kearns H., Shand N.C., Smith W.E., Faulds K., Graham D., Phys. Chem. Chem. Phys. 2015, 17, 1980.
- Kleinman S.L., Sharma B., Blaber M.G., Henry A.-I., Valley N., Freeman R.G., Natan M.J., Schatz G.C., Van Duyne R.P., J. Am. Chem. Soc. 2013, 135, 301.
- Kottmann J.P., Martin O.J.F., Smith D.R., Schultz S., Phys. Rev. B: Condens. Matter Mater. Phys. 2001, 64, 235402.
- Lane L.A., Qian X., Nie S., Chem. Rev. 2015, 115, 10489.
- Leopold N., Lendl B., J. Phys. Chem. B 2003, 107, 5723.
- Le Ru E.C., Galloway C., Etchegoin P.G., Phys. Chem. Chem. Phys., 2006, 8, 3083.
- Le Ru E., Etchegoin P., Principles of Surface-Enhanced Raman Spectroscopy and related plasmonic effects, Elsevier, Amsterdam, The Netherlands, Oxford, UK, 2009.
- Lombardi J.R., Birke R.L., Acc. Chem. Res., 2009, 42, 734.
- Mosier-Boss P.A., Nanomaterials 2017, 7, 142.
- Pietrobon B., McEachran M., Kitaev V., ACS Nano 2009, 3, 21.
- Reguera J., Langer J., Jiménez de Aberasturi D., Liz-Marzán L.M., Chem. Soc. Rev. 2017, 46, 3866.
- Rycenga M., Cobley C.M., Zeng J., Li W., Moran C.H., Zhang Q., Qin D., Xia Y., Chem. Rev., 2011, 111, 3669.
- Santos J.J., Ivanov E., dos Santos D.P., Toma H.E., Corio P., Chem. Phys. Chem. 2016, 17, 463.
- Shuford K.L, Ratner M.A., Schatz G.C., J. Chem. Phys. 2005, 123, 114713.
- Singh J.P., Lanier T.E., Zhu H.,. Dennis W.M, Tripp R.A., Zhao Y., J. Phys. Chem. C 2012, 116, 20550.
- Steinigeweg D., Schütz M., Salehi M., Schlücker S., Small 2011, 7, 2443.
- Sun Y., Nanoscale 2010, 2, 1626.
- Tao A., Kim F., Hess C., Goldberger J., He R., Sun Y., Xia Y., Yang P., Nano Lett. 2003, 3, 1229.
- Tao A.R., Habas S., Yang P., Small, 2008, 4, 310.
- Troy T.L., Thennadil S.N., J. Biomed. Opt. 2001, 6, 167.
- Wiley B., Sun Y., Xia Y., Acc. Chem. Res., 2007, 40, 1067.

- Zhang X., Dai Z., Si S., Zhang X., Wu W., Deng H., Wang F., Xiao X., Jiang C., Small 2017, 13, 1603347.
- Zhou J., An J., Tang B., Xu S., Cao Y., Zhao B., Xu W., Chang J., Lombardi J.R., Langmuir 2008, 24, 10407.

Chapter 5

SERS spectroscopy for in-field detection of pesticides and pollutants in agrifood products

- Tognaccini L., Ricci M., Gellini C., Feis A., Smulevich G., Becucci M., SERS for detection of dimethoate residues in water and olive leaves, Molecules 24, 2019, 292.
- Tognaccini L., Ricci M., Gellini C., Feis A., Becucci M., Smulevich G., Surface-enhanced Raman spectra of glyphosate: a correlation with ordinary Raman spectra based on isotopic substitution, to be submitted to J. Raman Spectrosc.

5.1 Introduction

In modern agriculture, chemical pesticides are widely used and play an essential role in food production [Matson 1997, Khöler 2013]. Most chemical pesticides are designed to be toxic to living organisms, so they might represent a risk for the human health and the environment. There is increasing evidence showing an association between pesticide exposures and human diseases, such as cancer and nervous system disorders [Alavanja 2004, Saeedi Saravi 2001]. Therefore, the balance between large-scale, cost-effective, production in agriculture and the public demand of healthy, possibly organic, food is actively pursued and a continuous effort is made for a sustainable use of pesticides. Their possible field of application, dose and allowed residual limit is defined by public regulatory authorities and periodically revised. Analytical methods with very high sensitivity and general applicability for pesticides exist, mostly based on extraction and chromatographic method. Efficient routines (QuEChERS) have been devised allowing sample cleanup and multiresidue analysis of pesticides, fully responding to the present norms. However these methods require many steps (sampling, transport to the laboratory, storage of the sample, analysis), a long time and an advanced sample manipulation (including the use of different solvents and reagents). Simple analytical methods, possibly suitable for in-field application can be of great interest, especially if adapted for targeted analysis of specific pesticides that are known to be used to control the presence of specific pests in the interest area.

Thanks to its high sensitivity, SERS spectroscopy could be a very suitable candidate for this kind of application. One of the potential advantages of SERS, when compared to chromatographic methods, is the selectivity in the identification of single components in multicomponent mixtures, since the vibrational spectrum can be considered as a fingerprint of the analyte. This can avoid pretreatment and/or functionalization of the analytes making the analysis quicker and cheaper. In recent years, SERS spectroscopy has been widely used in the detection of pesticide residues in water solution and even on food surfaces [Guerrini 2011, Fang H. 2015, Fang W. 2015, Liu 2012, Yang 2014, Zhai 2015, Zhang 2014, Albuquerque 2015, Furini 2015, Furini 2016, Wang 2018, Chen 2018]. Moreover, since many small portable instruments already exist, in-field application could also become feasible [Lee 2007, Halvorson 2010, Yan 2007, Pilot 2017].

The aim of my work was to develop a simple, quick, in-field detection method, based on SERS spectroscopy to be applied on widely used chemicals. The results obtained for the common pesticides, namely dimethoate and glyphosate, will be discussed in this chapter.

On the contrary, only preliminary results obatined on food pollutants, the so-called FCMs (food contact materials) will be reported in the last part of this chapter

5.2 Materials

Dimethoate (DMT), glyphosate (GLP) glyphosate-2-^{13}C, aminomethylphosphonic acid (AMPA), KNO_3, $AgNO_3$ and sodium citrate were purchased from Sigma and used without further purification. Diisodecyl phthalate (DIDP) as a pure compound, bisphenol A and 4-octylphenol (4-OP) as 10^{-4} M methanol solutions were provided by our collaborators in Istituto Zooprofilattico Sperimentale del Lazio e della Toscana (IZSLT). Isopropanol (from Merck) was distilled before use. Water used for preparation of the different solutions was lquid chromatography - mass spectrometry grade, obtained from Sigma.

5.2.1 Samples preparation

Silver nanoparticles were prepared as colloidal dispersions according to the standard Lee Meisel method [Lee 1982]. The synthesis was repeated several times with similar results and we always obtained, as usual, a rather large size distribution of spherical particles. The colloid properties were checked measuring their UV-Vis extinction spectrum, that corresponds to the ones reported in the literature [Ca˜namares 2005].

The analyte solutions were prepared by adding to 160 μL of the colloidal dispersion 20 μL of a 0.3 M solution of KNO_3 (as aggregant) and 20 μL of a standard analyte solution in water to obtain final concentrations ranging from 10^{-3} to 10^{-6} M. DIDP, being water-insoluble, was previously dissolved in isopropanol.

SERS spectra of DMT solutions dried on olive leaves were measured on samples prepared by deposition of a 1 μL of 10^{-2} - 10^{-6} M DMT water solution followed, after 1 hour, by deposition on the same spot of another 2 μL drop of colloidal dispersion aggregated by KNO_3 (as described above).

5.3 Dimethoate

DMT is an organophosphorus insecticide and acaricide commonly used since the ‘50s in particular to protect olive trees from the olive fly (*Bactrocera oleae*), that is probably the most important pest affecting olives in some regions (typically the Mediterranean basin and South Africa and, more recently, also California). Its presence is most relevant in areas and periods characterized by higher humidity and relatively lower temperatures. DMT on the leaf surfaces is oxidized to its active oxygenated analogous omethoate (OMT), while the absorbed DMT is decomposed following different enzymatic reaction pathways [Dauterman 1960]. This is the reason for the regulatory limits defined as the sum of DMT and OMT content. The DMT and OMT structures are sketched in **Fig. 5.1**.

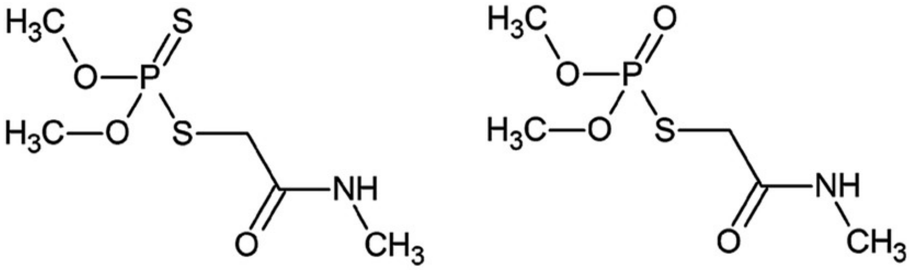

Figure 5.1: Schematic structure of DMT (left) and OMT (right).

DMT is suggested for treatments on olive plants as a water solution at 10^{-2}-10^{-3} M concentration range, according to the technical datasheet from the producer Cheminova AS for the different treatment strategies (80-625 ml of the industrial formulation containing 40% DMT in weight per 100 L of the final solution to be spread). It has a deadline deficiency (interval between treatment and use of product) of 28 days. Its persistence (either as DMT or OMT) on the olive fruit surface is up to 10% on the four weeks timescale [FAO Report 2003]. The presence of DMT on olives is allowed to the maximum limit 2 mg/Kg [Commission Directive 2008/17/EC of 19 February 2008] while on olive oil the limit is 0.05 mg/kg [Codex Alimentarius Commission, Codex alimentarius pesticide residues in food-maximum residues limits, 2nd ed., Vol. 2B, FAO/WHO Press, 1996]. Even if DMT is noxious for human health, neurotoxic by ingestion, inhalation and skin contact, it is considered quite safe to use for olive oil production, because, being highly water-soluble, it flows away in the residual water during the oil extraction process. This is very convenient but poses severe issues on the treatment of the residues from olive oil production (the limit in drinking water is 6 μg/L (i.e. 2.6×10^{-8} M) [FAO/WHO 1997, WHO 2003] and on the certification of organic cultures, where DMT use is not permitted. Furthermore, DMT use is allowed in many productions, including citrus, lettuce, tomatoes, onions and others. Therefore, the availability of simple and effective methods for its in-field identification is of extreme interest for public health and for certification of organically grown food.

5.3.1 SERS detection in solution

The SERS spectra of DMT solutions at different concentrations using the portable BWTek system with the 785 nm have been obtained (**Fig. 5.3**). The spectra are in agreement with the work published by Guerrini et al. [Guerrini 2011].

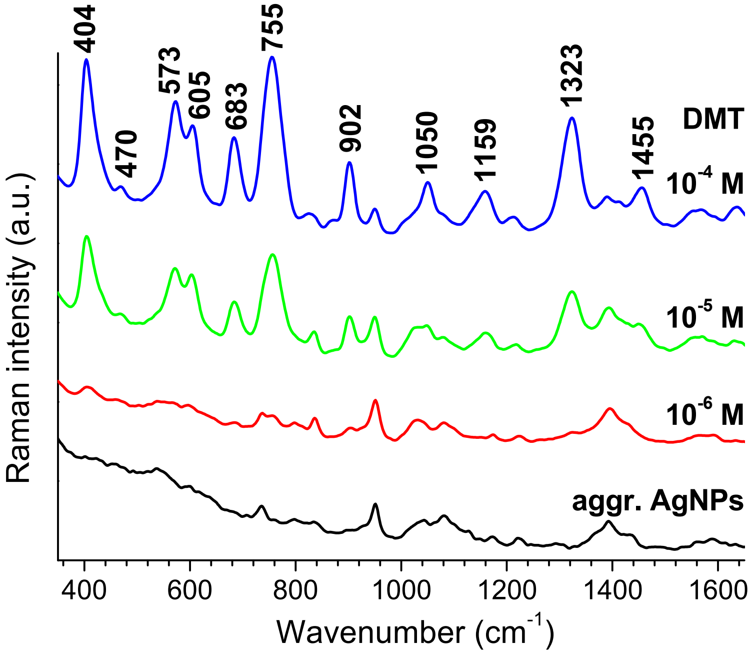

Figure 5.3: SERS spectra (λ_{exc} = 785 nm) of DMT from 10^{-4} to 10^{-6} M concentration (red, blue, pink) compared with the aggregated AgNPs background (black). Experimental conditions: 20 mW at the sample, average of 5 spectra with 8'20'' integration time.

As previously reported [Guerrini 2011], it appears that AgNPs promote DMT hydrolysis to omethoate (OMT). Therefore, the spectrum can show possible contribution to the different molecules present in the actual solution, a contribution whose ratio is changed by the reaction advancement. Nevertheless, the isolated single δ(NCC) band at 404 cm^{-1} [Guerrini 2011] in the SERS spectrum could be a good reference for the possible quantification of DMT in the sample (**Fig. 5.4**).

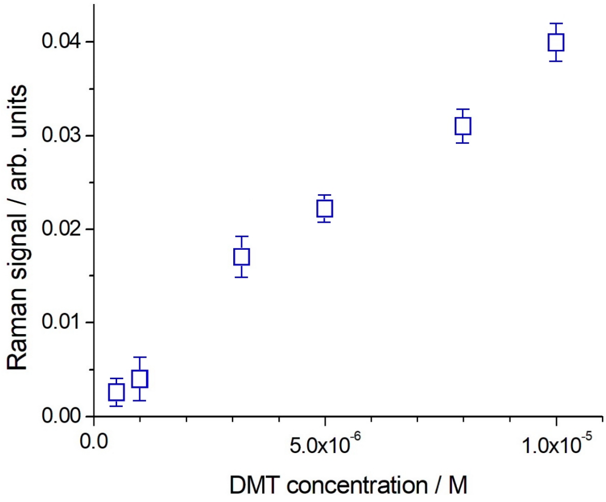

Figure 5.4 DMT SERS signal (785 nm excitation) on the peak at 404 cm^{-1} as a function of DMT nominal concentration.

Analogous SERS spectra have also been obtained with other excitation wavelengths at 458, 532, 633 and 1064 nm. With the shorter wavelengths (458 and 532 nm) a negligible intensity SERS signal was observed with respect to 633, 785 and 1064 nm excitations. This is expected, because in the 600-1100 nm region, extinction is mostly due to aggregated NPs (see **Fig. 5.5**) and it is well known that a partial NPs aggregation induced by presence of specific ions in solution (like nitrate) can strongly improve the SERS signal for longer wavelength excitation, thanks to the formation of strongly SERS-active aggregates of nanoparticles, the so-called ‘hot-spots’ [Ca˜namares 2005].

In details, the aggregation has been followed spectroscopically, by checking the change of the UV-Vis extinction spectrum with the concentration of nitrate. Upon addition of KNO_3, a decrease of the extinction peak at 417 nm and an increase of the longer wavelength wing of the signal has been observed, as already reported [Ca˜namares 2005]. A 100 mM KNO_3 concentration in solution completely destabilize the Ag colloidal dispersion, while at 30 mM KNO_3 concentration the colloidal dispersion is still stable during the measurements (see **Fig. 5.5**), a strong aggregation is spectroscopically observed and the SERS efficiency strongly increases using the wavelength excitation of 785 nm and above. Moreover, since no changes in the spectrum overall shape due to the laser wavelength was observed, I worked with excitation in the long wavelength region.

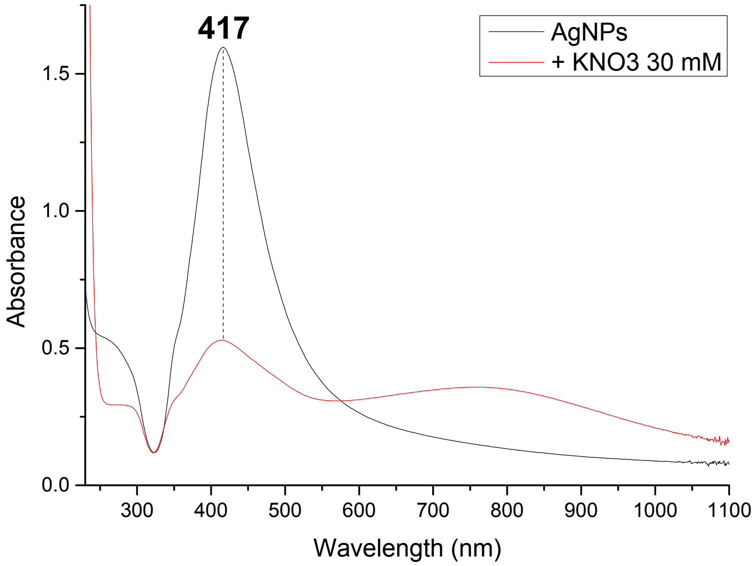

Figure 5.5: UV-Vis absorption spectra of as-synthesized AgNPs (black) and AgNPs after addition of the KNO_3 solution (red).

Furthermore, I have measured the relative SERS signal enhancement for DMT with 785 and 1064 nm excitation in the presence of 10% (v/v) ethanol, which is not adsorbed on AgNPs and does not destabilize the colloidal dispersion. Therefore, the Raman peaks of ethanol can be used as internal standard for intensity calibration of the DMT SERS signals. As shown in **Fig. 5.6**, we observed a signal enhancement approximately two times higher in the DMT spectrum taken with the 785 nm excitation as compared to the 1064 nm excitation, indicating that 785 nm is a favorable excitation wavelength for this SERS substrate. Even if an increase of the SERS enhancement factor does not intrinsically lead to an improvement of the S/N ratio, which is rather related to various experimental conditions (e.g.: detector efficiency, gratings reflectivity, etc.), the 785 nm excitation wavelength was chosen to perform all the next experiments due to the availability of instruments, even portable, that allowed me to measure DMT signal both in solution and on solid substrates, including direct measure on olive leaves.

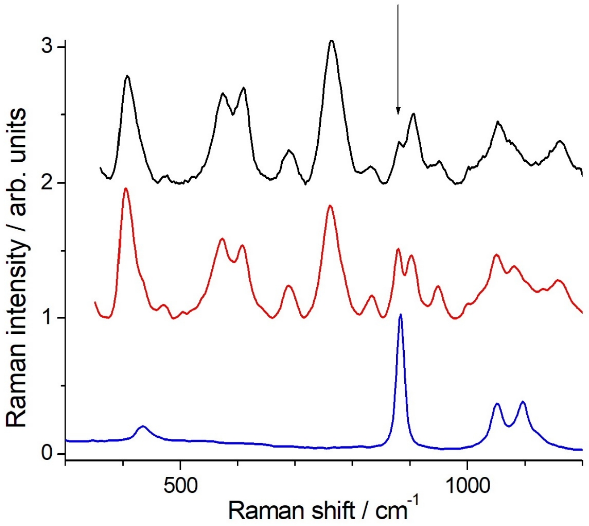

Figure 5.6: Raman spectrum of ethanol taken with the 785 nm excitation (blue), and SERS spectra of 10^{-4}M DMT taken with the 1064 (red) and 785 nm (black) excitation, in presence of 10% ethanol. The arrow points to the ethanol band at 893 cm^{-1}, used to evaluate the relative SERS enhancement factors. Experimental conditions: (blue) 2 mW at the sample, 5 minutes integration time; (red) 100 mW at the sample, 400 scans average; (black) 20 mW at the sample, average of 5 spectra with 8’20’’ integration time.

5.3.2 SERS detection on olive leaves

1. In order to test the possibility to detect the presence of DMT on olive leaves via SERS experiment in-situ, I have measured the Raman/SERS signal of olive leaves obtained with the 785 nm excitation using a Raman microscope. I dropped 2 μL of aggregated AgNPs colloidal dispersion on a bare olive leaf (picked from an ornamental non-contaminated olive tree), let it dry and collected a spectrum using a micro-Raman equipped with a 785 nm laser source. No relevant Raman signal is observed and the fluorescence background (**Fig. 5.6**, red) is efficiently quenched by the AgNPs (**Fig. 5.6**, green). The spectra taken on the front and back of the leaf are very similar, but the signal is slightly larger on the front surface. Therefore, I proceed to setup a test on samples spiked with DMT.

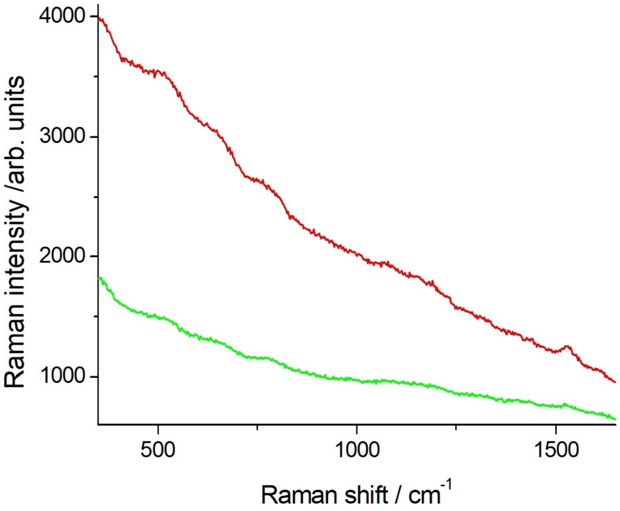

Figure 5.7: Raman spectrum with 785 nm excitation of a clean olive leaf (red) and in presence of AgNPs (green). Experimental conditions: 2 mW at the sample, 5 minutes integration time.

2. The first test was executed on a glass slide, where I sprayed a DMT 10^{-2} M solution (recommended concentration for in-field treatments) with aggregated AgNPs, similar to those used for the tests in solution described above (**Fig. 5.3**). The sprayer produced a good aerosol that covered uniformly the surface with 20-100 μm diameter droplets. Then I used the 785 nm excitation wavelength of a Raman microscope and obtained a SERS spectrum with very good S/N ratio (**Fig. 5.8**, blue). Furthermore, similar DMT solutions in the 10^{-2} - 10^{-4} M range were sprayed on olive leafs and let dry in air. The SERS spectra have been taken from many different points with a Raman microscope. In some cases, it was possible to recognize the position of the drop on the dried sample by visual inspection. The SERS signal of DMT was detected with a reasonably good S/N ratio (**Fig. 5.8**, red).Unlike the DMT SERS spectrum in solution (**Fig 5.3**), in this case the observed spectrum shows some features of OMT and a strong peak around 500 cm^{-1}, characteristic of solid DMT [Guerrini 2011]. Nevertheless, the intense δ(NCC) peak at 404 cm^{-1} is still clearly observable.

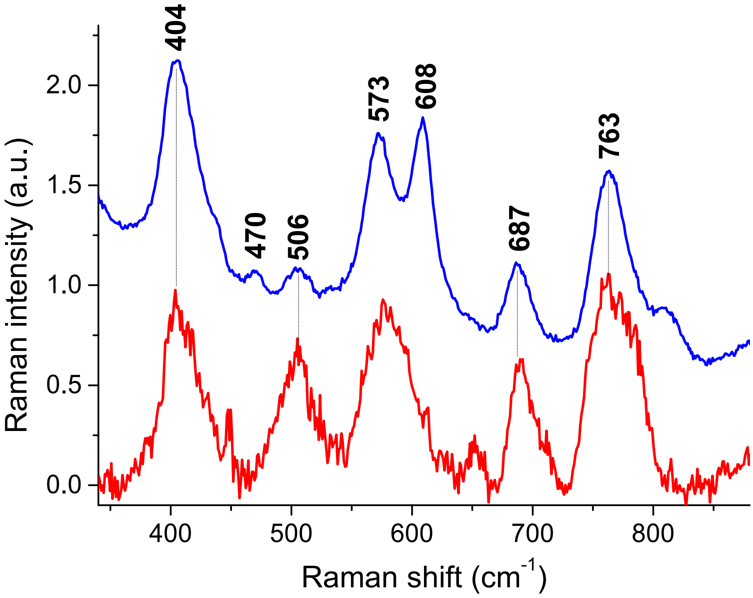

Figure 5.8 SERS spectra of DMT 10^{-2} M solution taken on the glass slide (blue) and of DMT 10^{-4} M solution taken on the olive leaf (red) with 2 mW laser power at 785 nm, 10 s acquisition time, 1 average (blue), 20 averages (red).

3. Detailed information on the DMT distribution on the leaves could be obtained by Raman line-scanning experiments. I dropped 1 µL of DMT 10^{-3} M solution on a clean leaf, let it dry and then added 2 µL of aggregated AgNPs dispersion on the same spot and other 2 µL on a clean near spot (see photo inset in **Fig. 5.7**). Then, I performed Raman line-scanning experiments by placing the sample on a computer controlled motorized micrometric table, acquiring the spectrum on the two spots and plotting the intensity of the δ(NCC) band at 404 cm^{-1} as a function of the sampling point position. Only a small section of the spectrum was selected for numerical elaboration, around the 404 cm^{-1} band, namely 350-450 cm^{-1}, such that it was possible to fit the spectrum by using only a linear baseline and one single band with a Lorentzian profile for a total of five free parameters (with appropriate constrains for the band center position and bandwidth). **Fig. 5.9** shows the intensity signal of the 404 cm^{-1} band for line-scans made across a leaf area, either clean or contaminated with 1 µL of 10^{-3}M DMT solution, covered by 2 µL of AgNPs colloidal dispersion and air dried. The experiment gives

zero signal on the clean leaf surface or in that covered with AgNPs only, while the leaf region treated with DMT/AgNPs (visually measured as 3 mm large) is clearly identified. The irregular distribution of the signal is only due to the irregular distribution of AgNPs between the leaf stomata.

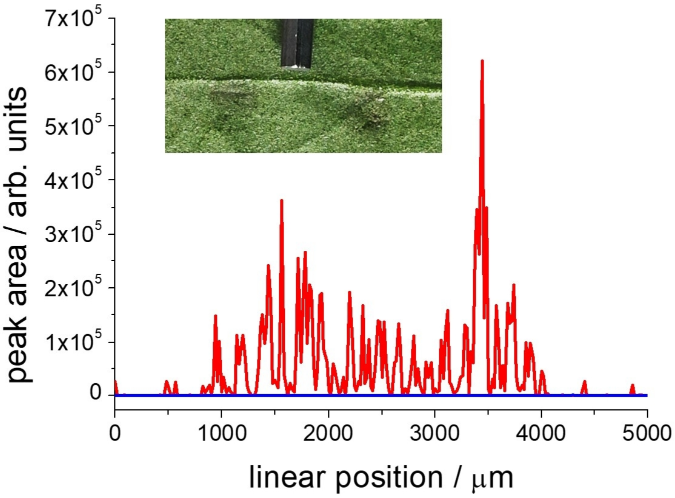

Figure 5.9: Plot of the DMT 404 cm^{-1} peak intensity in a 5 mm line-scan (20 μm step) passing across a 3 mm diameter area treated with the AgNPs solution and spiked with DMT (red) or not (blue). The inset shows a picture of the leaf and the two measured areas (DMT treated and not), identified as grey circles due to the presence of AgNPS. The tip of a 2 mm hex key has been put in between the two spots to set the scale of the image.

4. Finally, to simulate a real in-field situation, I sprayed an olive leaf with a 10^{-2} M DMT solution. Then, 2 μL droplets of AgNPs were deposited in various points of the leaf. SERS spectra with very good S/N ratio has been obtained after subtraction of the clean leaf background (**Fig 5.10**). Unlike the spectrum of the solution of DMT with aggregated AgNPs (**Fig. 5.3**), in this case the observed spectrum shows some typical features of OMT [Guerrini 2011]: the absence of the band at 470 cm^{-1}, the decrease of the band at 605 cm^{-1}, the growth of the bands at 776 and 863 cm^{-1}, the downshift of the band at 1323 to 1303 cm^{-1}; moreover, the peak at 507 cm^{-1}, characteristic of solid DMT [Guerrini 2011], is quite intense (**Fig. 5.10**). With this method, the

intense δ(NCC) band at 404 cm^{-1} allows detection of the presence of DMT even when less concentrated solutions are sprayed on the leaf, in particular, until a 10^{-5} M concentration. This is a very promising result, since with a simple drop deposition of AgNPs solution and a portable Raman instrument, DMT can be detected at concentrations far lower than that of the commercially available solutions. This simple protocol could easily become a quick screening method for organic cultures certification, avoiding the need of expensive and time-consuming analysis when traces of DMT are not detected by SERS on a statistically significant number of leaves.

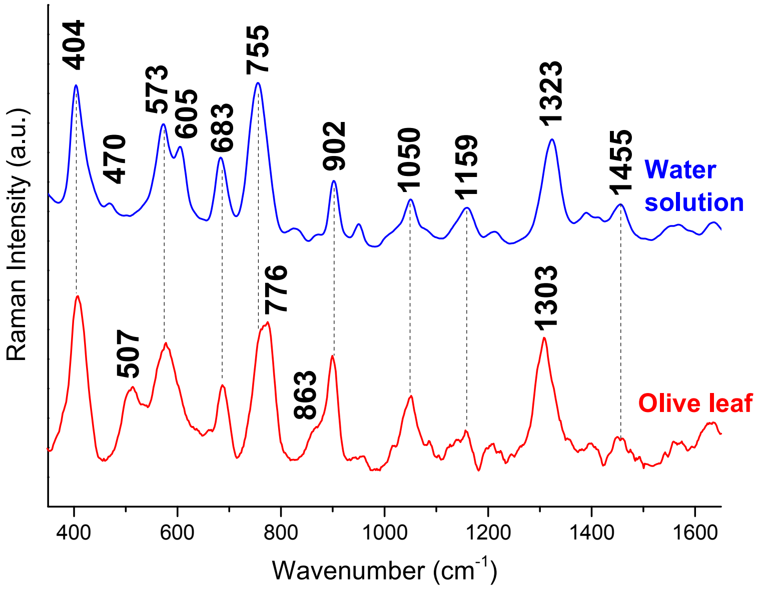

Figure 5.10: SERS spectra (λ_{exc} = 785 nm) of DMT 10^{-4} M in water solution (blue) and DMT 10^{-2} M sprayed and dried on an olive leaf (red). Experimental conditions. 20 mW at the sample, average of 5 spectra with 8'20'' integration time (blue), 5 mW at the sample, average of 10 spectra with 1'40'' integration time.

5.4 Glyphosate

GLP is a common non-selective herbicide used to kill weeds and especially grasses that compete with crops [Borggard 2008, Fenner 2013]. Being moderately soluble, GLP tends to accumulate in water and hence in the soil. In fact, GLP interacts strongly with soil components by forming stable complexes with metal ions [Khoury 2010], and it is thus considered an immobile compound, which remains adsorbed in the ground [Laitinen 2009, Rampazzo 2013]. In fact, both GLP and one of its principal metabolites, aminomethylphosphonic acid (AMPA, **Fig. 5.11**) [Rampazzo 2009, Ndjeri 2013], have frequently been detected in surface waters and even groundwaters. While GLP has been approved by regulatory bodies worldwide, concerns about its effects persist, and have grown as the global usage of GLP increases . In March 2015 the World Health Organization's International Agency for Research on Cancer classified GLP as "probably carcinogenic in humans" based on epidemiological, animal and in vitro studies [Guyton 2015]. Although an official limit in drinking water has not been set, some countries established a maximum contaminant level goal (MCLG) at 0.7 mg/L, i.e. 4.1×10^{-6} M to prevent potential health problems [Safe Drinking Water Act (SDWA) amendment of 1986, Speth 1993]. Hence, it is very likely that a quick practical method to reveal GLP in water and soil will be needed, so I tried to apply the same method that I developed for DMT to the GLP detection.

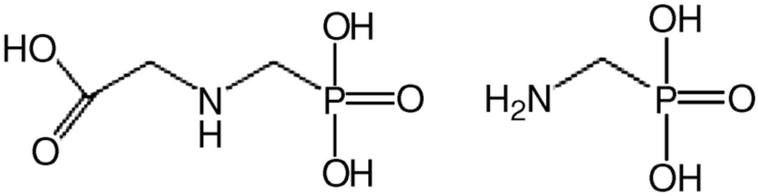

Figure 5.11: Schematic structure of GLP (left) and AMPA (right).

5.4.1 Glyphosate SERS detection

In order to develop a SERS method for GLP detection in water and soil, the first step is obtaining a reproducible SERS spectrum of the molecule. Despite the relevance of GLP for human health and environment, the number of literature SERS studies is limited. A SERS spectrum at 3.3×10^{-7} M concentration was obtained on Ag nanocubes [Costa 2012], showing few relationships with the Raman spectrum of solid GLP. The authors assigned the SERS spectrum to the anionic form of GLP, and performed DFT (density functional theory) calculations for the anion in vacuo and on a Ag atom to support their interpretation. It is noted that the calculated Raman spectrum of GLP anion shares only some features with the SERS spectrum on nanocubes.

Unfortunately, I was unable to obtain an experimental Raman spectrum of GLP in water solution due to the limited solubility in water (5x10^{-2} M), at all pH values (3-12). Therefore, I collected the solid-state FT-Raman spectra of GLP and of the 2-^{13}C isotopically substituted molecule (**Fig. 5.12**) and the solid-state FT-IR spectrum (**Fig. 5.13**). A tentative assignment, on the basis of literature data [Costa 2012, Ascolani Yael 2014, Sheals 2001], is reported in **Table 5.1**. The isotopic substitution is expected to downshift those bands deriving from the modes involving the 2-^{13}C atom. Accordingly, 17 isotope-sensitive bands are observed, which are marked above the spectrum of 2-^{13}C GLP (**Fig. 5.12**, red). As expected, large (~10 cm^{-1}) isotopic shifts (**Table 5.1**) were observed for two of the ν(CH) bands in the 2900-3100 cm^{-1} region. Large shifts were also observed for the 1081/1069 cm^{-1} band, assigned to a ν(CN) + ν(COH) mode, and for the 864/857 cm^{-1} band, assigned to a ρ(CH$_2$) + δ(NH) + ν(CC) mode. Smaller shifts (2-4 cm^{-1}) were displayed by bands assigned to modes mainly involving other functional groups. Moreover, the isotopic substitution effect on the 1036 cm^{-1} band showed that this band is formed by two components.

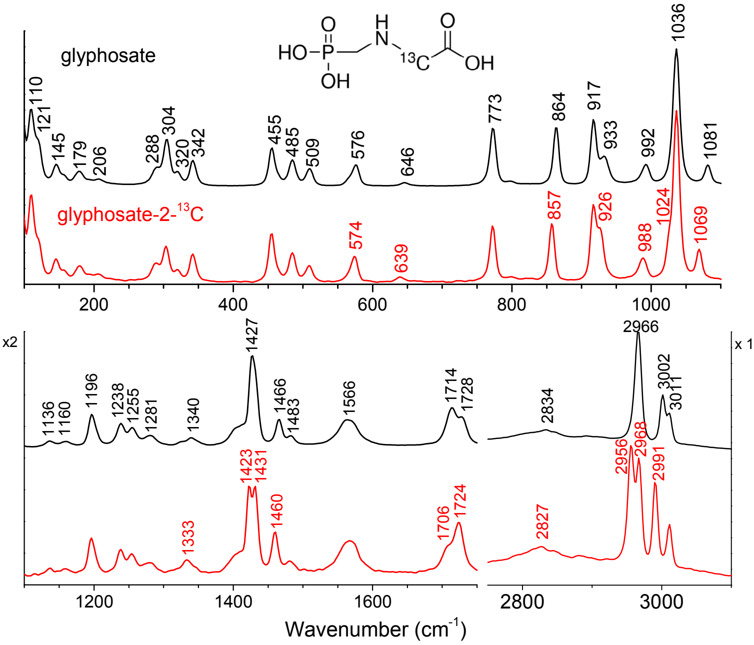

Figure 5.12: Raman spectra of solid GLP (black) and its 2-^{13}C isotope (red). Experimental conditions: laser excitation wavelength 1064 nm, 100 mW laser power at the sample, 100 scans average.

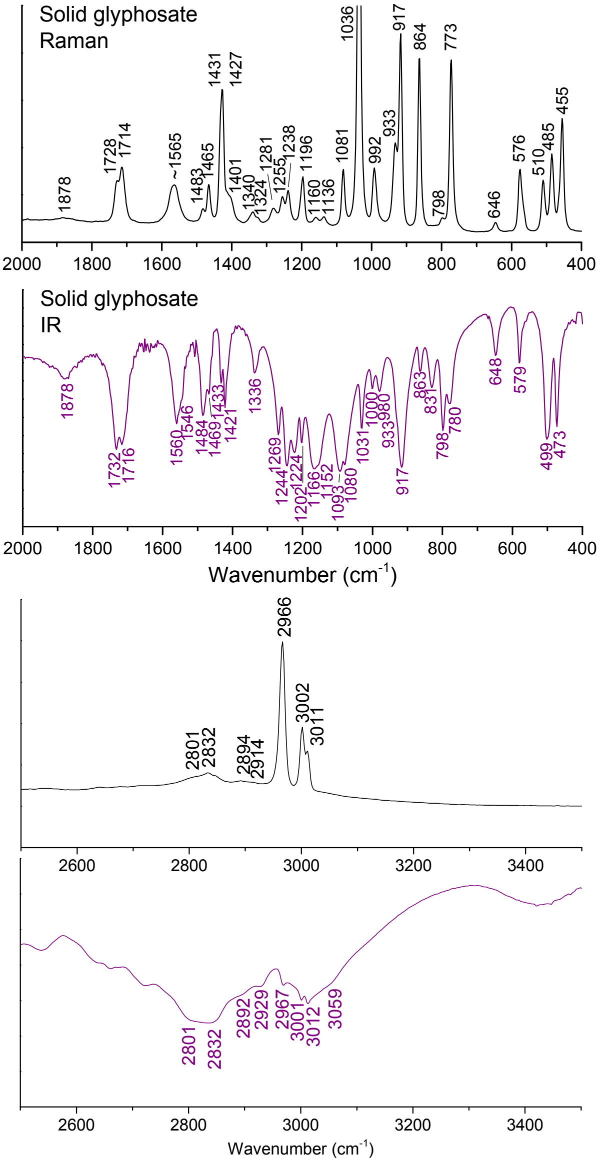

Figure 5.13: Raman (black) and IR (violet) spectra of solid GLP.

Table 5.1. Tentative assignment of the bands (cm^{-1}) observed in the Raman and SERS spectra of GLP and its 2-^{13}C isotope, based on [Costa 2012, Ascolani Yael 2014, Sheals 2001].

Raman		SERS		Tentative assignment
2-^{12}C GLP	2-^{13}C GLP	2-^{12}C GLP	2-^{13}C GLP	
455				$\rho(CH_2) + \delta(OH)$
485				$\delta(OH) + \rho(CH_2) + (PO_2)$
509				$\delta(OH) + \delta(CH)$
576	574			$\delta(OH) + \delta(OH\text{-}C{=}O)$
646	639			
773		770		$\delta(NH) + \rho(CH_2) + \nu(P\text{–}OH)$
		800		
		819		
864	857			$\rho(CH_2) + \delta(NH) + \nu(C\text{–}C)$
917		889	885	$\rho(CH_2)$
933	926	936	927	
992	988	974	968	$\rho(CH_2) + \delta(OH)$
1036	1036	1027	1027	$\nu_{sym}(PO) + \delta(OH)$
	1024		1021	
1081	1069			$\nu(C\text{–}N) +$
1160				$\nu_{as}(PO)$
1196		1189		$\tau(CH_2) + \delta(OH) + \nu_{as}(PO)$
1238				$\tau(CH_2)$
1255				$\omega(CH_2)$
1281				
		1313	1311	
1340	1333			$\omega(CH_2)) + \nu(C\text{–}C)$
1427	1423	1435 (broad)	1425	$\delta(2\text{-}CH_2)$ + carbon backbone^a
1431 (shoulder)	1431			$\delta(4\text{-}CH_2)$ + carbon backbone^a
1466	1460			
1483				
1566				$\delta(NH_2)$
1714	1706			$\nu(C{=}O)$ H-bonded
1728	1724			$\nu(C{=}O)$ free
2834	2827			
2966	2955	2950	2947	$\nu_{sym}(CH_2)$
	2968			$\nu_{as}(CH_2)$
3002	2991			$\nu_{sym}(CH_2)$
3011		2996		$\nu_{as}(CH_2)$

[a] Mode involving motions of the carbon backbone coupled with C-O and P-O stretching motions

Following the Raman experiments, I obtained the SERS spectrum of GLP on Lee-Meisel AgNPs dispersion (**Fig. 5.14**), that is quite different from the one previously obtained on silver nanocube surfaces [Costa 2012]. The wavenumbers of the SERS bands are reported in **Table 5.1**. Most bands are shifted and the enhancement pattern is variable, as it often occurs in SERS [Lombardi 2009, Le Ru 2009]. Two main features, though, exceed the differences which are commonly observed, i.e., the very strong SERS band at 720 cm^{-1}, which lacks a possible Raman counterpart, and the strongest Raman band at 1036 cm^{-1}, which becomes very weak in the SERS spectrum.

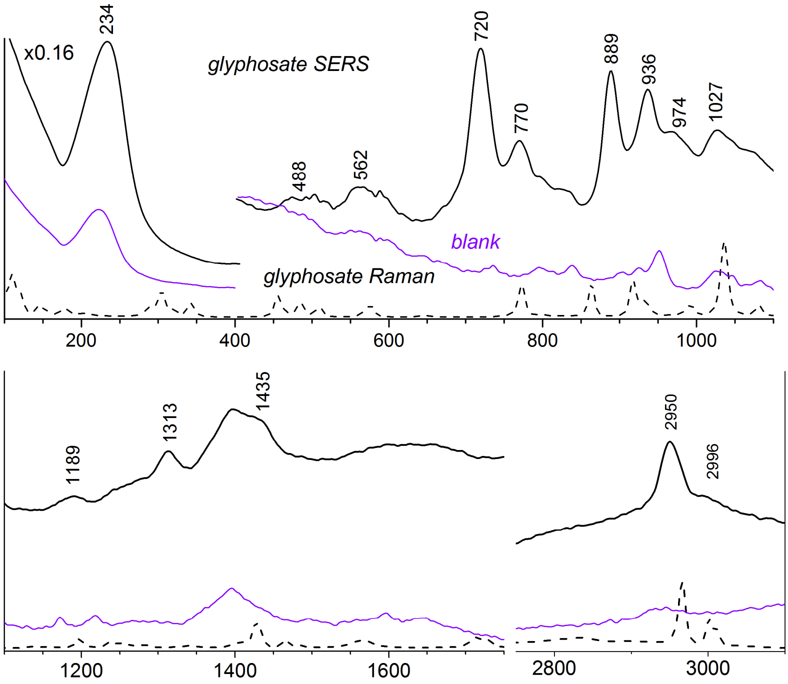

Figure 5.14: SERS (continuous line) and Raman (dashed line) spectra of GLP. The SERS spectrum of the Ag colloid (blank) is also reported. Experimental conditions: 1064 nm laser excitation wavelength. SERS: 200 mW laser power at the sample, 400 scans average; Raman: 100 mW, 100 scans average; blank: 200 mW, 1000 scans.

Due to the limited frequency correspondence between the Raman and SERS bands, and the very high analyte concentration (0.1 mM, at least) necessary to detect SERS spectra, I needed to prove that the SERS spectrum really arose from adsorbed GLP. Therefore, I obtained the SERS spectrum of 2-^{13}C GLP (**Fig. 5.15**), that is very similar to those obtained for the non-substituted molecule: seven SERS bands displaying small wavenumber shifts are well correlated to the isotopic shifts observed for the corresponding bands in the solid state (**Table 5.1**), thus supporting that the SERS spectrum I obtained arises from GLP. Remarkably, two SERS bands (770 and 1189 cm^{-1}) are unshifted, similarly to the corresponding Raman bands at 773 and 1196 cm^{-1}.

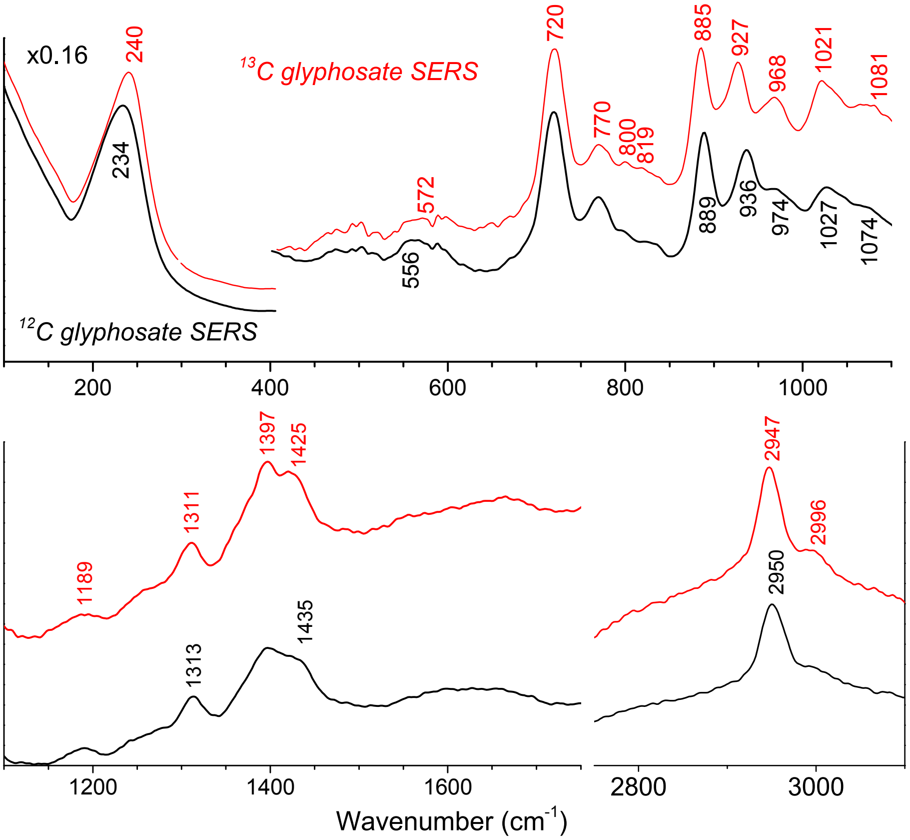

Figure 5.15: Comparison of the SERS spectra of GLP and its 2-^{13}C isotope. Experimental conditions: 1064 nm excitation wavelength, 200 mW laser power at the sample, 400 scans average.

The very strong SERS band at 720 cm^{-1} cannot be related to any Raman band of solid GLP. Following a suggestion from previous work [Ascolani Yael 2014], indicating that GLP on an Ag surface decomposes to AMPA, I measured Raman and SERS spectra of this compound (**Fig. 5.16**).

The affinity of AMPA for the Ag surface was even lower than that of GLP, as only few bands could be observed together with the background citrate bands, notwithstanding the high (5 mM) AMPA concentration. The strongest band at 730 cm^{-1} might be related to the GLP SERS band at 720 cm^{-1}, but a 10 cm^{-1} difference is hard to justify. More likely, the spectrum of GLP derives from a slightly different fragmentation product, like methylphosphonic acid, hydroxymethylphosphonic acid or others.

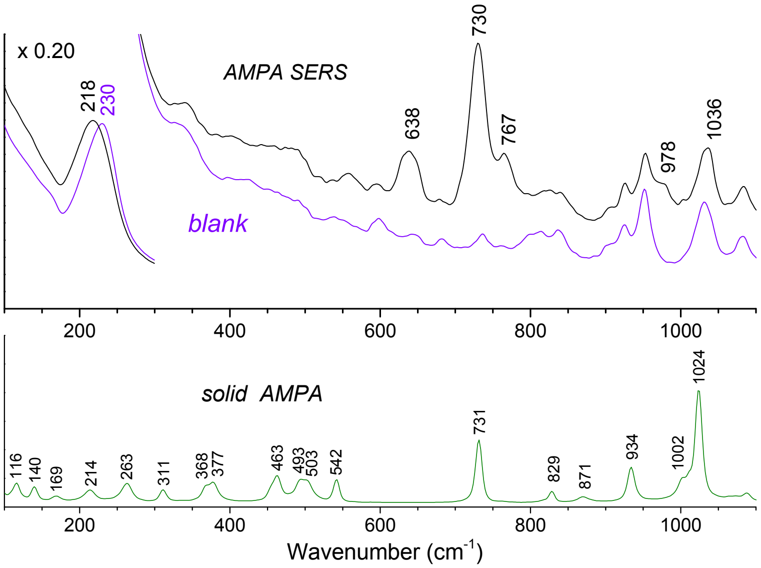

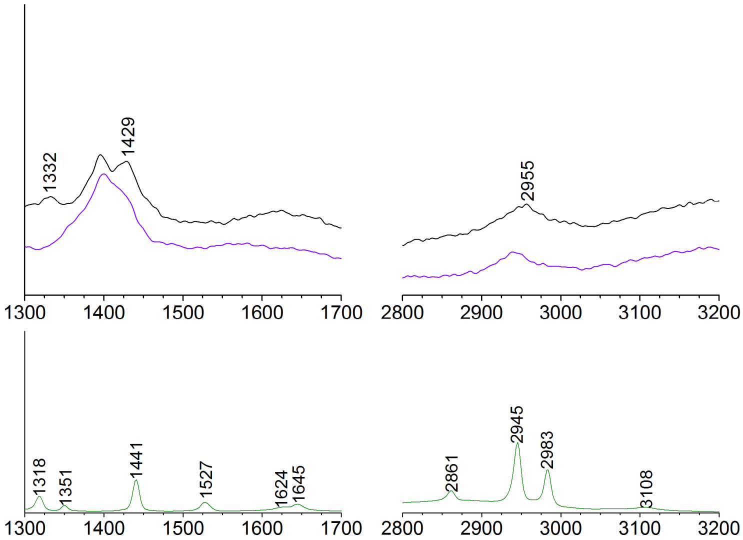

Figure 5.16: Raman (green) and SERS (Black) spectra of AMPA. The aggregated AgNPs spectrum is also reported (blank). Experimental conditions: 1064 nm laser excitation wavelength; Raman: 100 mW laser power at the sample, 100 scans average; SERS: 200 mW, 400 scans average; blank: 200 mW, 1000 scans average.

In order to try to increase the sensitivity of the SERS detection, I repeated the measurements using AgNPs synthesized by reduction with $NaBH_4$ or hydroxylamine, or even AuNPs and I tried a different aggregation agent, NaCl. However, AuNPs and hydroxylamine AgNPs did not allow to detect any signal and $NaBH_4$ AgNPs performed poorly, leading to spectra with high background and weak bands.

In conclusion, these are some useful preliminary results that allowed to define and tentatively assign the GLP SERS spectrum on AgNPs surface, but in order to develop an efficient in-field method, the sensitivity must be improved with alternative SERS substrates. Moroever, SERS spectra of other possible GLP degradation products must be studied.

5.5 Food contact materials

FCMs are a class of molecules used as plasticizer additives in food packaging to improve the flexibility, plasticity or viscosity of a polymer, thus allowing to obtain the desirable mechanic properties. They include phthalate esthers, bisphenols, alkylphenols and other hydrophobic molecules, that are liable to be released from plastic to the food content in condition of unstable temperature, long-term usage and critical pH. Due to the large plastic-packaged food consumption, FCMs accumulation in the consumers' body is a real possibility and it poses high risk to human health due to their endocrine disruptor properties [Diamanti-Kandarakis 2009, Mathieu-Denoncourt 2015]. Chronic exposure can increase the risk of developing reproductive cancers, cause lowered fertility, birth malformations, and sexual development problems [Harrison 1999]. In May 2011, a major phthalate-contaminated foodstuffs incident happened in Taiwan: di(2-ethylhexyl) phthalate (DEHP) and diisononyl phthalate were illegally added to foods and beverages as substitute emulsifiers [Yang 2013, Wu 2012]. Hence, a robust and reliable assessment is necessary to identify FCMs in air, water and food [Fang 2013, Yen 2011]. The difficulties in detecting endocrine disruptor compounds lie in the variety and the low concentrations. The traditionally used detection methods are high performance liquid chromatography [Tranfo 2012], high performance liquid chromatography-tandem mass spectrometry [Wu 2012, Koch 2012], gas chromatography-mass spectrometry [Sanchez-Avila 2012, Fierens 2012] and gas chromatography-electron capture detector. These methods are highly robust, however, some features, such as requiring complex sample pre-treatment, being time-consuming and having high cost, limit their applications [Cheung 2010].

5.5.1 Preliminary results

Three samples from different plasticizer classes were analyzed by Raman and SERS spectroscopy on Lee-Meisel AgNPs:

- DIDP (diisodecyl phthalate) as a pure compound,
- bisphenol A in a 10^{-4} methanol solution,
- 4-OP (4-octylphenol) in a 10^{-4} methanol solution.

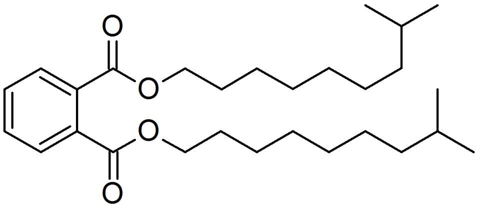

DIDP

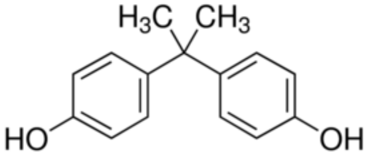

Bisphenol A

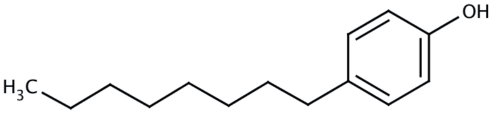

4-Octylphenol

SERS spectra of many phthalate esthers have been obtained on silica or anodic aluminium oxide nanostructured arrays decorated with various kind of AgNPs or AuNPs [Chou 2014, Chen 2015, Tang 2015, Zuo 2015, Wu 2018]; to the best of my knowledge, no data are reported for DIDP, but many works about DEHP have been recently published [Cao 2014, Chou 2014, Wu 2018], that is another long alkyl chain-substituted phthalate esther.

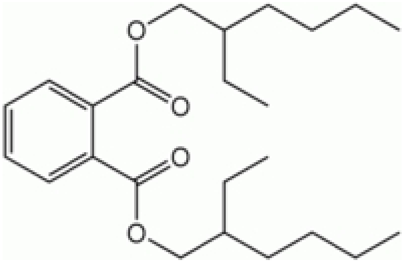

DEHP

SERS on bisphenol A has been reported on Lee-Meisel AgNPs by functionalization with diazonium ions [Han 2011] or on surface-imprinted core-shell AuNPs [Xue 2013]. No Raman or SERS data are reported for 4-OP.

The spectra were collected using the 532.3 nm and 1064 nm excitations, with similar results. Therefore, only the 1064 nm spectra will be shown. DIDP Raman spectrum is shown in Fig. **5.17** and is closely related to the Raman spectrum observed for DEHP [Wu 2018]. The Raman spectrum of the other analytes were identical to that of pure methanol due to the low concentration of the samples.

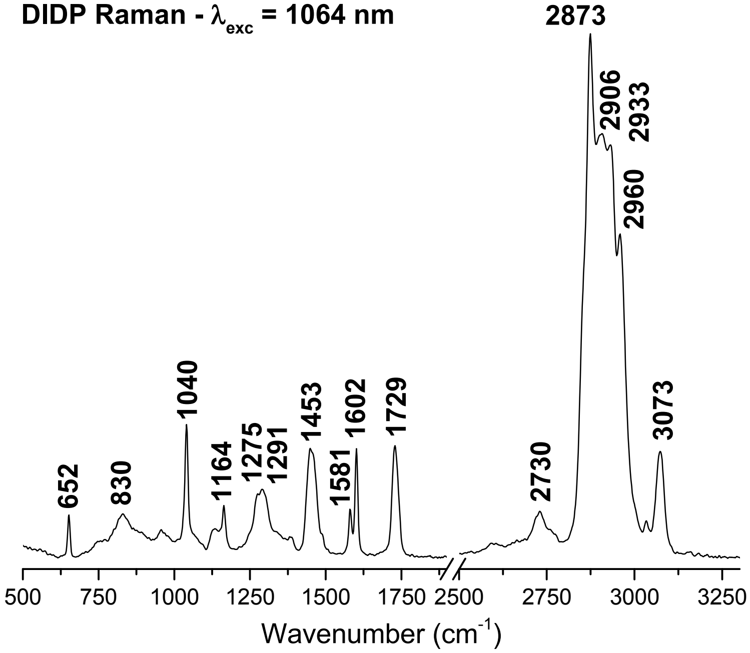

Figure 5.17: Pure DIDP Raman spectrum. Experimental conditions: 1064 nm excitation wavelength, 100 mW power at the sample, 100 scans average.

SERS analysis on aggregated AgNPs gave no results for all the examined samples under analysis, except that for bisphenol A. Its spectrum showed three weak bands decreasing with the concentration as compared to the citrate intense background (**Fig. 5.18**). The band at 1175 cm^{-1} is reminiscent of the 1178 cm^{-1} band observed on surface-imprinted core-shell AuNPs [Xue 2013, Wang 2011], but the other two bands are not characteristic of bisphenol A. Moreover, the other typical bands at 638 cm^{-1}, 820 cm^{-1}, 1102 cm^{-1}of bisphenol A SERS spectra are not observed.

I tried to improve the sensitivity and eliminate interference from the citrate capping agent by repeating the measurements with BH_4 and hydroxylamine reduced AgNPs, but, again, I obtained the same results for all the samples.

This is not surprising, since low affinity for Ag and Au surfaces has already been reported for bisphenols [Lezna 1991, Barnett 1994, Rodriguez-Lorenzo 2010, Han 2011] and for the other molecules the issue is very likely the same.

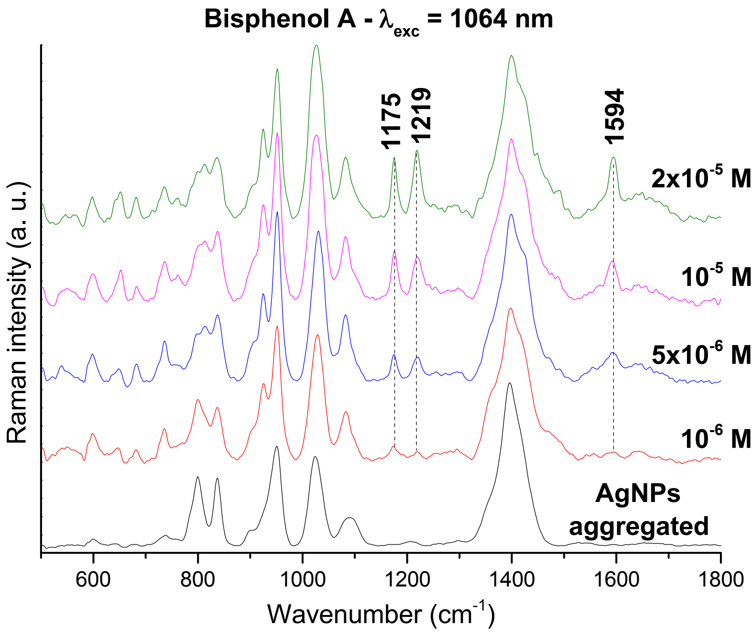

Figure 5.18: Bisphenol A SERS spectra from $2x10^{-5}$ to 10^{-6} M. The spectrum of aggregated AgNPs (black) is reported for comparison. Experimental conditions: 1064 nm excitation wavelength, 200 mW power at the sample, 500 scans average.

Since development of an efficient SERS detection method requires reproducible and fairly intense SERS spectra, two fundamental steps are needed: (i) acquisition of the pure compounds Raman spectra of all the samples; (ii) development of an effective AgNPs functionalization strategy to increase the analytes adsorption on the metal surface [Xue 2013, Droghetti 2013].

5.6 Conclusions

In conclusion, Lee-Meisel AgNPs proved to be a valid nanosubstrate for quick detection of DMT directly on the olive leaves. In fact, the presence of DMT can be detected by simply depositing a drop of AgNPs colloidal solution on a leaf and acquiring a few seconds spectrum with commercially available portable instruments. The intense isolated band at 404 cm^{-1} guarantees reproducibility and sensitivity until concentration three orders of magnitude inferior to the commonly used DMT solutions. This kind of test could be easily adopted for certification of organic oil production as a quick and low-cost screening technique before proceeding to more expensive and time-consuming quantitative analysis.

The same NPs also provided reproducible SERS spectra of GLP, which allowed for the first time a tentative assignment. Nevertheless, GLP, and also FCMs compounds, proved insufficient affinity for citrate-capped AgNPs surface, thus indicating the necessity of specific surface engineering to obtain an appropriate sensitivity.

References

- Alavanja M.C.R., Hoppin J.A., Kamel F., Annu. Rev. Public Health 2004, 25, 155−197.
- Albuquerque C.D., Poppi R.J., Anal. Chim. Acta 2015, 879, 24–33.
- Ascolani Yael J., Fuhr J.D., Bocan G.A., Daza Millone A., Tognalli N., dos Santos Afonso M., Martiarena M.L., Journal of agricultural and food chemistry 2014, 62, 40, 9651-9656.
- Barnett S.M., Vlckova B., Butler I.S., Kanigan T.S., Anal. Chem. 1994, 66, 1762-1765.
- Borggaard V., Gimsing A.L., Pest Manage. Sci. 2008, 64, 441−456.
- Ca˜namares M.V., Garcia-Ramos J.V., Gómez-Varga J.D., Domingo C., Sanchez-Cortes S., Langmuir **2005**, 21, 8546.
- Cao Q., Che R., ACS Appl. Mater. Interfaces 2014, 6, 7020-7027.
- Chen J., Qin G., Shen W., Li Y., Das B., J. Mater. Chem. C 2015, 3, 1309.
- Cheung W., Shadi I.T., Xu Y., Goodacre R., J. Phys. Chem. C 2010, 114, 7285–7290.
- Chou A., Radi B., Jaatinen E., Juodkazis S., Fredericks P.M., Analyst 2014, 139, 1960-1966.
- Costa J.C., Ando R.A., Sant'Ana A.C., Corio P., Physical Chemistry Chemical Physics 2012, 14, 45, 15645-15651.
- Dauterman W.C., Viado, G.B., Casida J.E., O'Brien R.D., Journal of Agricultural and Food Chemistry 1960, 8, 2, 115-9.
- Diamanti-Kandarakis E., Bourguignon J.-P., Giudice L.C., Hauser R., Prins G.S., Soto A.M., Zoeller R.T., Gore A.C., Endocr. Rev. 2009, 30, 293.
- Droghetti E., Nicoletti F.P., Guandalini L., Bartolucci G., Smulevich G., J. Raman Spectrosc. 2013, 44, 10, 1428-1434.
- Fang C., Bandaru N.M., Ellis A.V., Voelcker N.H., Biosens. Bioelectron. 2013, 42, 632–639.
- Fang H., Zhang X., Zhang S.J., Liu L., Zhao Y.M., Xu H.J., Sens. Actuators B 2015, 213, 452–456.
- Fang W., Zhang X., Chen Y., Wan L., Huang W., Shen A., Hu J., Anal. Chem. 2015, 87, 9217−9224.

- Fenner K., Canonica S., Wackett L.P., Elsner M., Science 2013, 341, 752.
- Fierens T., Van Holderbeke M., Willems H., De Henauw S., Sioen, I., Food Chem. Toxicol. 2012, 50, 2945–2953.
- Furini L.N., Sanchez-Cortes S., López-Tocón I., Otero J.C., Aroca R.F., Costantino C.J.L., J. Raman Spectrosc. 2015, 46, 1095-1101.
- Furini L.N., Costantino C.J.L., Sanchez-Cortes S., Otero J.C., López-Tocón I., J. Colloid Interface Sci. 2016, 465, 183-189.
- Guerrini L., Sanchez-Cortes S., Cruz V.L., Martinez S., Ristori S., Feis A., J. Raman Spectrosc. 2011, 42, 980–985.
- Guyton K.Z., Loomis D., Grosse Y., El Ghissassi F., Benbrahim-Tallaa L., Guha N., Scoccianti C., Mattock H., Straif K., The Lancet Oncology 16 (2015) 490.
- Halvorson R.A., Vikesland P.J., Environ. Sci. Technol. 2010, 44, 7749.
- Han X.X., Pienpinijtham P., Zhao B., Ozaki Y., Analytical chemistry 2011, 83, 22, 8582-8588.
- Harrison R.M., Hester R.E., Endocrine Disrupting Chemicals, Royal Society of Chemistry, Cambridge, UK, 1999.
- Khoury G.A., Gehris T.C., Tribe L., Torres Sánchez R.M., dos Santos Afonso M., Appl. Clay Sci. 2010, 50, 167−175.
- Koch H.M., Haller A., Weiss T., Kafferlein H.U., Stork J., Bruning T., Toxicol. Lett. 2012, 213, 100–106.
- Köhler H.-R., Triebskorn R. Science 2013, 341, 759−765.
- Laitinen P., Rämö S., Nikunen U., Jauhiainen L., Siimes K., Turtola E., Plant Soil 2009, 323, 267−283.
- Lee P.C., Meisel D., J. Phys. Chem. 1982, 86, 3391–3395.
- Lee S., Choi J., Chen L., Park B., Kyong J.B., Seong G.H., Choo J., Lee Y., Shin K.H., Lee E.K., Joo S.W., Lee K.H., Anal. Chim. Acta 2007, 590, 139.
- Le Ru E., Etchegoin P., Principles of Surface-Enhanced Raman Spectroscopy and related plasmonic effects, Elsevier: Amsterdam, The Netherlands, Oxford, U.K., 2009.
- Lezna R.O., Detacconi N.R., Centeno S.A., Arvia A.J., Langmuir 1991, 7, 1241–1246.

- Liu B., Han G., Zhang Z., Liu R., Jiang C., Wang S., Han M.Y., Anal. Chem. 2012, 84, 255.
- Lombardi J.R, Birke R., Acc. Chem. Res. 2009, 42, 6, 734-742.
- Mathieu-Denoncourt J., Wallace S.J., de Solla S.R., Langlois V.S., Gen. Comp. Endocrinol. 2015, 219, 74.
- Matson P.A., Parton W.J., Power A.G., Swif, M.J. Science 1997, 277, 504−509.
- Ndjeri M., Pensel A., Peulon S., Haldys V., Desmazieres B., Chausse A., Colloids Surf. A 2013, 435, 154−169.
- Pilot R., J. Raman Spectrosc. 2018, 49, 954-981.
- Rampazzo N., Rampazzo Todorovic G., Mentler A., Blum W.E.H., Int. Agrophys. 2013, 27, 203−209.
- Rodriguez-Lorenzo L., Alvarez-Puebla R.A., de Abajo F.J.G., Liz-Marzan, L.M., J. Phys. Chem. C 2010, 114, 7336-7340.
- Saeedi Saravi S.S., Dehpour A.R. Life Sci. 2016, 145, 255−264.
- Sanchez-Avila J., Tauler R., Lacorte S., Environ. Int. 2012, 46, 50–62.
- Sheals J., Persson P., Hedman B., Inorg. Chem. 2001, 40, 4302.
- Speth T., Env. Eng. 1993,119, 6, 1139
- Tang H., Meng G., Li Z., Zhu C., Huang Z., Wang Z., Li F., Nano Res. 2015, 8, 2261-2270.
- Tranfo G., Caporossi L., Paci E., Aragona C., Romanzi D., De Carolis C., De Rosa M., Capanna S., Papaleo B., Pera A., Toxicol. Lett. 2012, 213, 15–20.
- Wang K., Huang M., Chen J., Lin L., Kong L., Liu X., Wang H., Lin M., J. Raman Spectrosc. 2018, 49, 3, 493-498.
- Wang S., Lu H., Ma N., Bao Y., Wang H., Liu Z., Yao W., Spectrosc. Spectral Anal. 2011, 31, 1006–1009.
- Wu M.T., Wu C.F., Wu J.R., Chen B.H., Chen E.K., Chao M.C., Liu C.K., Ho C.K., Environ. Int. 2012, 44, 75–79.
- Wu M.-C., Lin M.-P., Lin T.-H., Su W.-F., Jpn. J. Appl. Phys. 2018, 57, 04FM07.
- Xue J.Q., Li D.W., Qu L.L., Long Y.T., Anal. Chim. Acta 2013, 777, 57-62.
- Yan F., Vo-Dinh T., Sens. Actuators B 2007, 121, 61.

- Yang J., Hauser R., Goldman R.H., Food Chem. Toxicol. 2013, 58, 362–368.
- Yang J.K., Kang H., Lee H., Jo A., Jeong S., Jeon S.J., Kim H.I., Lee H.Y., Jeong D.H., Kim J.H., ACS Appl. Mater. Interfaces 2014, 6, 12541.
- Yen T.H., Lin-Tan D.T., Lin J.L., Formosan J., Med. Assoc. 2011, 110, 671–684.
- Zhai C., Li Y.Y., Peng Y.K., Xu T.F., Int. J. Agric. Biol. Eng. 2015, 113–120.
- Zhang Y., Wang Z., Wu L., Pei Y., Chen P., Cui Y., Analyst 2014, 139, 5148.
- Zuo Z., Zhu K., Ning L., Cui G., Qu J., Cheng Y., Wang J., Shi Y., Xu D., Xin,Y., Appl. Surf. Sci. 2015, 325, 45-51.
- FAO/WHO (1997) Pesticide residues in food – 1996 evaluations. Part II – Toxicological. Geneva, World Health Organization, Joint FAO/WHO Meeting on Pesticide Residues (WHO/PCS/97.1)
- WHO (2003) Dimethoate in drinking-water. Background document for preparation of WHO Guidelines for drinking-water quality. Geneva, 1World Health Organization (WHO/SDE/WSH/03.04/90)
- Safe Drinking Water Act (SDWA) amendment of 1986